UNIVERSITY OF CALIFORNIA
RIVERSIDE

Study of Tectonic Tremor in Depth: Triggering Stress Observation and Model of the Triggering Mechanism

A Dissertation submitted in partial satisfaction
of the requirements for the degree of

Doctor of Philosophy

in

Geological Sciences

by

Tien-Huei Wang

December 2014

Dissertation Committee:
Dr. David D. Oglesby, Chairperson
Dr. Elizabeth S. Cochran
Dr. Abhijit Ghosh

The Dissertation of Tien-Huei Wang is approved:

_____

_____

_____

Committee Chairperson

University of California, Riverside

Acknowledgements

This work has been a tremendously challenging journey but it has fulfilled my graduate school life with interesting stories. I thank my family of origin, and my new family of procreation just established. I owe them everything for their support and generous forgiveness for me while I try to accomplish the dream in science. I thank my parents who always encourage me to hang on to the goal. Especially my mother who always encourages me mentally during the time I struggled with new parenthood obligations along with the plateau phase of my study. I thank my loving husband and beautiful little daughter to put up with my limited time that I can spend with them. My husband has been generously supporting our new family, most of the time when I devoted to research in the last two years.

I also thank my advisors David Oglesby and Elizabeth Cochran, for their great patience and effort spent being my mentors. And thank them for being best role models for me to look up to both in academia and in life. I thank Dr. Ghosh for his kindness to teach me about beamforming and providing the data from UCR Array that makes it possible for Chapter 4. I thank Dr. Richards-Dinger, who patiently guided me through the derivations of rate-and-state friction. His effort helps improve my understanding of the constitutive law in a much deeper sense. Lastly, I thank Jim Dieterich for his warm offer on time, his leadership and bright ideas in numerous discussions with me, which is the solid foundation for my modeling chapter.

I thank Dr. Agnew for his collaboration and guidance in using the strain data. I truly enjoy and benefit from his straightforward style of communication and discussions.

This work has been supported by SCEC 2009 Grant (Number 09054) and NSF Grant (Number 0943892). My graduation study in the US has been supported by the 2006 Taiwanese scholarship funded by Ministry of Education in Taiwan.

To my beloved Abbie little girl,

Hope that one day you can pursue your dreams with flying colors,

ABSTRACT OF THE DISSERTATION

Study of Tectonic Tremor in Depth: Triggering Stress Observation and Model of the Triggering Mechanism

by

Tien-Huei Wang

Doctor of Philosophy, Graduate Program in Geological Sciences
University of California, Riverside, December 2014
Dr. David D. Oglesby, Chairperson

Non-volcanic tremor (NVT) has been discovered in recent years due to advances in seismic instruments and increased density of seismic networks. The NVT is a seismic signal typically generated on the fault below the main seismogenic portion of the fault that may provide insight into the physical conditions and the failure mechanism of the source. The detection methods used and the sensitivity of them relies on the density, distance and instrumentation of the station network available. How accurately the tremor is identified in different regions varies greatly among different studies. Therefore, there has not been a study that rigorously documents tectonic tremors in different regions using consistent methods and data. Many cases of NVTs are observed during or after small but significant strain changes induced by teleseismic, regional, or local earthquakes. The understanding of the triggering mechanisms critical for tremor remains unclear. In addition, characteristics of the triggering of NVT in different regions are rarely compared because of the short time frame after the discovery of the triggered NVTs. We first explore tectonic tremor based on observations to learn about its triggering, frequency of

occurrence, location and spectral characteristics. Then, we numerically model the triggering of instability on the estimated tremor-source, under assumptions fine-tuned according to previous studies (Thomas et al., 2009; Miyazawa et al., 2005; Hill, 2008; Ito, 2009; Rubinstein et al., 2007; Peng and Chao, 2008). The onset of the slip reveals that how and when the external loading triggers tremor. It also provides information on the background stress conditions under which tremor source starts with.

We observe and detect tremor in two regions: Anza and Cholame, along San Jacinto Fault (SJF) and San Andreas Fault (SAF) respectively. These two sections of the faults, relative to fault zone on which earthquakes (slip rate ~above 1^{-1} m/s; Lapusta and Rosakis, 2007) occur, are considered transition zones where slip of slow rates occurs (Johanson, 2006; Hong and Menke, 2006). Slip events including NVT occur on these sections have slower slip rates than that of the earthquakes (Rubin, 2008; Ide, 2008). In Azna region, we use envelope and waveform cross-correlation to detect tremor. We investigate the stress required to trigger tremor and tremor spectrum using continuous broadband seismograms from 11 stations located near Anza, California. We examine 44 $M_w \geq 7.4$ teleseismic events between 2001 and 2011, in addition to one regional earthquake of smaller-magnitude, the 2009 M_w 6.5 Gulf of California earthquake, because it induced extremely high strain at Anza. The result suggests that not only the amplitude of the induced strain, but also the period of the incoming surface wave, may control triggering of tremor near Anza. In addition, we find that the transient-shear stress (17–35 kPa) required to trigger tremor along the SJF at Anza is distinctly higher than what has been reported for the well-studied SAF (Gulihem et al. 2010).

We also use a newly deployed mini-array to detected tremor along the SAF. We use a beam-backprojection method (Ghosh et al., 2009, 2012) that enhanced imaging power to detect tremor more accurately than most conventional methods. This method finds the coherent tremor signal by stacking waveform data in slowness domain with a delay-and-sum approach. We detect tremor along the Cholame section of the SAF using the beam-backprojection method along with visual inspection to confirm the accuracy. We found the tremor rates increase at least 2 times or more after 6 out of 11 teleseismic and regional events. The detected tremor rate is also higher in comparison with the rate reported by previous studies (Nadeau and Guilhem, 2009). With the enhanced imaging power of beam-backprojection, we observed the triggering potential of 11 earthquakes which induced significant shear stress (0.07-4.5 kPa) in this region. The 11 earthquakes consist of 7 teleseismic (M_w >=7.0) and 4 regional (M_L >= 4.0) earthquakes. We observe the tremor rate before, during and after the 11 earthquakes. We find, in 7 out of 11 earthquakes, the tremor rate after the P-wave arrival of the major events is at least 2 times greater than the rate before. The results may also suggest that, for external loading of peak shear stress more than 0.25 kPa, triggering of tremor occurs 4 times out of 5. However, for peak shear stress less than 0.25 kPa, no apparent trend can be indicated.

We model slip initiation using the analytical solution of rate-and-state friction. We verify the correctness of this method by comparing the results with that from the dynamic model, implemented using the Multi-Dimensional Spectral Boundary Integral Code (MDSBI) written by Eric M. Dunham from Sanford University. We find that the analytical result is consistent with that of the dynamic model. We set up a patch model

with which the source stress and frictional conditions best resemble the current estimates of the tremor source. The frictional regime of this patch is rate-weakening. The initial normal and shear stress, and friction parameters are suggested by previous observations of tectonic tremor both in this and other studies (Brown et al., 2005; Shelly et al., 2006; Miyazawa, 2008; Ben-Zion, 2012). Our dynamic loading first consists of simple harmonic stress change with fixed periods, simplifying the transient stress history to resemble teleseismic earthquakes. We tested the period and amplitude of such periodic loading. We find that the period of the transient shear stress is less important relative to the amplitude. The triggering depends mainly on the ratio between amplitude of the shear stress loading and the background normal stress. We define a ratio of rates before and after the major events, which is indicative of the occurrence of the triggering of NVT. We later test the triggering of the instability using the shear stress history from 44 large teleseismic earthquakes (data equivalent to those used in Chapter 1). With the constraints of these observations, we find that the background normal stress should be in the range of ~400-700 kPa. The background normal stress suggested agrees with the common hypothesis that the tremor source is under low normal stress. In addition, our results provide a first estimation of the background normal stress with numerical method. We also demonstrate how our model finds constraints on the background physical stress or frictional conditions, with several incidences of real transient shear stressing which triggers or not-triggers tremor..

Contents

List of Figures

List of Tables

Chapter 1 Introduction

1.1 Background and Motivation

Non-volcanic tremor (used interchangeably in short as 'tremor', or NVT) is a newly observed seismic signal that has been an area receiving increasing attention (since Obara, 2002). NVT has been widely observed around the world in both subduction zones and crustal regions close to well-developed strike-slip faults (e.g. Obara, 2002; Obara et al., 2004; Rogers et al., 2003; Nadeau and Dolenc, 2005; Shelly et al., 2006; Schwartz and Rokosky, 2007). NVT is discriminated from typical earthquakes by its less-impulsive waveforms, lack of P-wave onset, occurrence in swarms, and low amplitude. Due to the low amplitude, the NVT is mostly only discernible at stations local to its source, with fair signal-to-noise ratio. NVT has long durations, lasting from minutes to hours, or to weeks, relative to earthquakes. NVT tends to have dominant frequency content from 0.5-15 Hz. Compared to earthquakes, the high frequency content (above 10 Hz) of its seismic signal usually decays rapidly.

NVT has been observed to occur spontaneously (e.g., Obara, 2002; Obara et al., 2004; Rogers et al., 2003; Nadeau and Dolenc, 2005; Shelly and Hardebeck, 2010), but their occurrence can also be modulated by tidal forces (e.g., Rubinstein et al., 2008; Thomas et al., 2009) and teleseismic surface wave arrivals (e.g., Miyazawa and Mori, 2005; Miyazawa and Mori, 2006; Rubinstein et al., 2007; Gomberg et al., 2008; Miyazawa and Brodsky, 2008; Peng and Chao, 2008; Peng et al., 2008; Rubinstein et al., 2009). In seismology, this new discovery is revealing a new view of frictional behaviors on the fault. The frictional behaviors cover a wide spectrum of events, including

earthquakes, slow-slip events (SSE), low-frequency earthquakes (LFE), episodic tremor and slip (ETS), and fault creep. The physical conditions involved in the source of the SSE, LFE and ETS events, which may have been critically different from each other, include the friction regime, pore-pressure, slip rate, and background stresses. NVT is observed at the down-dip location on a fault plane primarily between the shallow (above ~20-30 km depth) source of mega-earthquakes and the deeper region of creep. They are found not only along subduction zones, but also along well-developed crustal faults. The source location of tremor is contiguous with the region where hazardous earthquakes occur. The importance of NVT lies in its release of the stress on the fault with its frequent and large numbers of occurrences. The total energy release, in terms of the seismic moment from the NVT, is eminent to relation to that of earthquakes at regions where NVT is active. The seismic moment of tremor estimated at Cascadia can well exceed one Mw6.0 earthquake for 70 hours of duration (Aguiar et al., 2009). Thus, the NVT also plays an important role to the stress release on faults where it is observed. By understanding the phenomena of tremor and the physics behind its source, scientists gain crucial knowledge of the frictional behavior on faults.

Among the several interesting questions that have emerged from observations of NVT, one of the key questions is to understand the source mechanism of such tremor. Scientists strive to know the physics of the friction and pressure regime operating during tremor, as well as the material properties of the tremor source. The differences between tremor sources and earthquakes are still not fully understood. By understanding the source physics of the NVT, we could gain precious insights into the occurrence and

modulation of earthquakes if we understood more of the source physics of tremor. In light of the accumulating observations of NVTs, researchers (Shelly et al., 2006; Wech et al., 2012; Peacock et al., 2011; Ide, 2008) have explored and proposed several mechanisms for NVT. Detailed physical properties of the source region of NVT can be tested numerically. In the mean time, most of the numerical studies adopts the agreement made from observational studies that the location of tremor is highly related to SSE. Therefore, most of the physical parameters of the source of NVT are obliged to the characteristics of SSE (Ide, 2008; Ader et al., 2012) in numerical models. The physical properties can also be estimated by seismic observations (e.g. Ito et al., 2009; Shelly et al., 2006). Overall, there is general agreement that tremor responds to minute changes of stress, and its spatial and temporal frequency is highly sensitive to the physical conditions of the hypocentral region (Gomberg, 2010; Nadeau et al., 2008). NVT is a seismic signal released from slip on the fault that has slower slip rate than earthquakes. It also has a lower stress drop than earthquakes of the same magnitude (Zhang et al., 2011), and thus, it presents low signal-to-noise ratio on seismic waveforms. The tremor source is thought to be of small dimension and it seems to operate in a different friction regime relative to earthquakes (close to neutral rate-weakening and rate-strengthening). If this is true, the occurrence of tremor implies the presence of certain physical properties at the source region, which can then be indicators of the characteristics of particular source regions, once NVT is detected and located. In any case, sufficient details on the mechanism can only be estimated and validated by tremor observations. Consequently, a worldwide search for tremor is an important cooperative effort. Ample tremor observations at

different locations, under different conditions, will help to complete our understanding of the tremor source.

Another interesting question is the physical status and process under which tremor is triggered. The triggering and ambient stress of triggered NVTs provides information about the values of stress and frictional parameters, and the form of the additional stress loading critical to tremor initiation at particular location, under specific background stress and frictional history. These conditions are essential for the occurrence of both tremor and earthquakes. Moreover, tremor is known to be triggered by sudden or oscillatory stress changes (triggered tremor), or can spontaneously occur due to background tectonic loading (ambient tremor) (Nadeau and Dolenc, 2005; Gomberg, 2010). The temporal frequency of ambient tremor depends upon the loading history of stress and the in-situ stress and friction regime. The NVT can also be accelerated or hindered by local stress change caused by tides, local earthquakes, or transient stress from remote sources (Nadeau and Guilhem, 2009; Chao et al., 2011; Chao and Peng, 2012; Peng et al., 2013). These processes may be comparable to those known to trigger small earthquakes. Due to the nature of the tremor source, remote triggering of tremor in specific regions on the fault is more abundant in numbers compared to the triggering of earthquakes along the faults. Therefore, it is statistically convenient to study multiple incidences of the triggering process of tremor. Such remote triggering can also help us understand frictional failure in the specific regions on the fault, where the physical principles may be extended beyond tremor.

Immediate technical issues arise in the search for tremor. In particular, the methods to precisely determine tremor events using specialized array records, or limited data from surface broadband stations, are crucially important. The need for tremor searches worldwide gives rise to the applications of designed-array methods (Ghosh et al., 2009, 2012), improvements in signal detection, and enhancement of signal resolution (e.g. High-Resolution Seismic Network borehole stations) to successfully identify and locate tremors. Station arrays and back-projection (Ghosh et al., 2009, 2012), cross-correlation and stacks (Obara, 2002, Brown et al., 2005), and template matching (Shelly et al., 2006) can enhance the accuracy of the detection threshold and hence the precision of locating the tremor source. In addition, developments on these techniques accommodate the rapid analysis of large quantities of high-resolution data. Thus, more observations can be reported and serve as constraints to the proposed mechanisms of the tremor source, which can then be tested in numerical modeling.

Studying the triggering of tremor can be viewed as a natural experiment to probe the in-situ conditions on the fault, such as the background stresses and friction coefficient (Brodsky and Van der Elst, 2014). Tremor occurs in a frictional regime that is thought to be different from that of earthquakes. The tremor source is inferred to be spatially associated with creep or slow-slip earthquakes (Rogers and Dragert, 2003; Peng and Gomberg, 2010). In addition, the frictional regime of the creep or slow-slip events is thought to be rate-strengthening, while the tremor source is very close to rate-neutral (Ader et al., 2010). The differences in the stress conditions under which tremor is triggered is one piece of crucial information to further confine the source mechanism of

tremor. With the worldwide observation of tremor, ample evidence becomes available. The temporal and spatial occurrence of NVT reflect the state of stress and the frictional regime, as well as the remote stress resolved in regions close to the hypocenter. Both ambient and triggered NVTs have been observed in subduction zone and along well-developed strike-slip faults.

1.2 Contributions and Dissertation Organization

My work focuses on the triggering of tectonic tremor. In particular, I study the triggering process of tremor induced by earthquakes. The studies included in this dissertation look at triggering of tremor through different approaches. The approaches lie in three areas of interests as described above: observation, modeling, and detection methodology. The three studies cross-reference each other in some parts, while acting in cooperation to provide a more complete and realistic view of the triggering process of NVT.

The first part of my work is a thorough search for triggered tremors during the time of teleseismic earthquakes, using the conventional methods: visual inspection and cross-correlation of seismograms. This observational work was conducted in the Anza area along the SJF, and was inspired by the massive triggering of tectonic tremor in California by the 2002 Denali Fault earthquake (Gomberg, 2007). My observational study reports preliminary detections of triggered tectonic tremor at Anza. In this part of work, I not only report the characteristics of the tremor in Anza, but also suggest empirically that the tremor occurs less frequently in this region relative to other regions. In other regions (e.g. Cholame of SAF, Peng et al., 2009 ; north Washington of Cascadia,

Houston et al., 2010, 2011; Guerrero of Mexico, Zigone et al., 2012), the triggering of tremor occurs more frequently, in addition to the ambient tremor activity. This study serves as one piece of evidence in the overall pool of tremor observations worldwide (e.g. New Zealand, Fry et al., 2011; Taiwan, Chao et al., 2012; Canada, Rubinstein et al., 2009; Japan, Ide et al., 2007). For the first time, we constrain the minimum triggering stress for tremor in this area. The minimum stress required to trigger tremor is then used to refine the range of stresses to be tested in the numerical models of tremor triggering.

Remote triggering of tectonic tremor has been observed worldwide. Careful visual inspection of the waveform is still irreplaceable verification when we report tremor to the science community. The conventional template method is time-consuming because building up a visual-inspected template requires experienced eyes and long training. I carried out my observational studies of tremor using multiple methods with robust visual verification when possible.

The second part of my work focuses on implementing a methodology of tremor detection. We adopted a newly developed beam-backprojection method (Ghosh et al., 2009, 2012), which is known to enhance the signal-to-noise ratio in detecting tremor. Rates of detected tremor using the beam-backprojection method increases by twice or more compared to those detected by visual inspection (e.g. Obara, 2002; Nadeau and Guillem, 2009). With the enhanced detection of NVT, more detailed studies of tremor rate, rate modulation, and new explorations of the triggering of NVTs are now possible. A key advantage using this method is the improved signal-to-noise ratio through a delay-and-sum approach. We test this method using a mini-array ~100 km to the southwest of

the Cholame section of SAF. This work validates the improved detection with the beam-backprojection method and its advantages in improving the signal-to-noise ratio. The method is implemented to analyze tectonic tremor along SAF with the designed UCR-array. We first validate the effectiveness of this method by carefully inspecting the tremor detected. We take a conservative measurement: first, we define detections of these tremors that are clearly visible on the waveforms. Secondly, we detect tremor before and after the passage of teleseismic surface waves (M_w>=7.0) and local earthquakes (M_w>=4.0). These events cause local stress change ranges from .2 to 8 kPa. We compare our detection number with that reported by TremorScope catalogue of the UC Berkeley Seismolab that uses visual inspection (Nadeau and Guilhem, 2009). The number of detections using the beam-backprojection method is significantly higher: The rate of tremors detected after a major stress change (~0.25 kPa) induced by teleseismic or local events is increased by at least 50% in 10 out of 11 events. The result suggests that the threshold of the shear stress for triggering may be lower than the previous estimates (~1kPa; Gulihem et al., 2011) at this section of SAF.

Inspired by the first observational study, the second part of this dissertation is a numerical patch model of tremor nucleation using rate-and-state friction. This part of my work engages in the analysis of the triggering of slip instability on a tremor source. We incorporate as much as possible the characteristics and background physics of the tremor source, as estimated from preceding observations and theoretical/numerical studies. We design this model to represent a simplified tremor source and stress loading due to teleseismic waves, with the scale similar to those I used in my first study. Additionally,

several studies have reported triggered tremor and the triggering conditions (Miyazawa and Brodsky, 2008; Hill, 2012a, 2012b; Peng et al., 2010; Shelly et al., 2011). This model is the first one that closely models the remote stressing by teleseismic earthquakes on a tremor patch. This model simulates the frictional response of slip rate and seismic events over time, to a form of external stress loading. These frictional responses may lead eventually to a failure on the fault. The background frictional stability is determined according to the background seismic rate prior to external loading. The background seismic rate is subjected to change when shear stress changes. With this model, we are able to analyze individual factors involved in remote triggering of instability on a tremor-liked source. We test the effect of the amplitude and period of the stress change on the frictional stability. Such tests provide a theoretical background to the triggering potential of any long-period loading (teleseismic surface waves or tides). Based on the earlier observation analysis, we apply the stress histories induced by the teleseismic waves to the model. This study explains most of the factors that affect the triggering of tremor, or even small earthquakes. This study also tempts to provide some constraints and confirmations on the thresholds of the background stress and frictional condition for triggering of the NVT.

There are three chapters in this dissertation in which I describe my work. Each chapter corresponds to one of the three major interests mentioned previously. Chapter 2 discusses the triggered tremor observation located in the Anza region along the SJF. Chapter 3 presents the analytical model of triggering that incorporates stress loading by

teleseismic surface waves. Chapter 4 describes the implementation of the beam-backprojection method with a case study of tectonic tremor near the Cholame section of the SAF.

Chapter 2 Infrequent Triggering of Tremor along the San Jacinto Fault near Anza California

(This work is published in *Bulletin of the Seismological Society of America*, Vol. 103, No. 4, pp. 2482–2497 Infrequent Triggering of Tremor along the San Jacinto Fault near Anza, August 2013, doi:10.1785/0120120284, by Tien-Huei Wang, Elizabeth S. Cochran, Duncan Agnew, and David D. Oglesby)

2.1 Introduction

Tectonic tremor, also known as nonvolcanic tremor (NVT), has been widely observed around the world, in both subduction zones and crustal regions close to well-developed strike-slip faults (e.g., Obara, 2002; Rogers et al., 2003; Obara et al., 2004; Nadeau and Dolenc, 2005; Shelly et al., 2006; Schwartz and Rokosky, 2007). Tremor has been observed to occur spontaneously (e.g., Obara, 2002; Rogers et al., 2003; Obara et al., 2004; Nadeau and Dolenc, 2005; Shelly and Hardebeck, 2010), but their occurrence can also be modulated by tidal forces (e.g., Rubinstein et al., 2008; Thomas et al., 2009) and teleseismic surface wave arrivals (e.g., Miyazawa and Mori, 2005, 2006; Rubinstein et al., 2007; Gomberg et al., 2008; Miyazawa and Brodsky, 2008; Peng and Chao, 2008; Peng et al., 2008; Rubinstein et al., 2009; Gonzalez-Huizar et al., 2012). Tremor episodes triggered by the dynamic stress changes imposed by passing surface waves are well correlated with surface-wave peak amplitudes (e.g., Gomberg et al., 2008; Peng et al., 2008). Triggered tremor has been shown to be modulated by either teleseismic Love or Rayleigh wave arrivals, depending on the tectonic regime and fault plane orientation (Hill, 2012b). These observations of remote triggering hold clues to the failure-stress conditions on the deep fault (below typical seismogenic depths), and perhaps imply different material properties, such as high fluid pressures and/or lower effective friction

at or near the location of the triggered tremor. Specific failure conditions, including the amplitude and type of triggering stress, can illuminate the conditions necessary to generate tremor. Remote triggering of tremor is widely documented in various tectonic regions as the number of tremor observations has accumulated in recent years. However, the type of surface waves shown to trigger tremor appears to vary by region and/or faulting type. In subduction zones, studies in Japan report that tremor is modulated by the Rayleigh wave arrival (Miyazawa and Mori, 2005, 2006; Miyazawa and Brodsky, 2008), whereas in Cascadia (Rubinstein, 2009) and Taiwan (Peng and Chao, 2008) tremor is shown to start at the Love wave arrival. Miyazawa and Mori (2005, 2006) and Miyazawa and Brodsky (2008) suggest that volumetric strain changes due to the Rayleigh-wave arrival play a strong role in triggering tremor observed in Japan. The volumetric strain may cause dilatation on the fault, reducing friction, which acts to trigger tremor (Rubinstein, 2007). Miyazawa and Brodsky (2008) propose that the presence of fluid-induced volumetric strain modulates the normal stress, causing strong triggering. According to Hill (2012b), Rayleigh waves encourage failure on normal faults above ~13 km depth and encourage failure on thrust faults at deeper depths, where incoming waves are normal to fault strike. In contrast, Love waves induce large differential stresses across the fault surface with peak strains occurring when incident surface waves are parallel to fault strike (Hill, 2012b). Rubinstein et al. (2007) showed that shear-stress changes induced by passing Love waves due to the 2002 M 7.8 Denali earthquake triggered tremor in Cascadia. They noted that incident Love waves were parallel to the trench and, thus, encouraged tremor occurrence. Peng and Chao (2008) also concluded that tremor on

a detachment fault underneath the Central Range in Taiwan was likely triggered by the Love-wave arrival. They suggested that triggering was coincident with the Love and not the Rayleigh wave due to the higher amplitude of the Love wave, estimated to be roughly four times larger than the Rayleigh wave. Along strike-slip faults in California, Gomberg et al. (2008) reported the 2002 Denali Mw 7.8 earthquake triggered tremor in multiple locations, including along the San Andreas fault (SAF) and on the San Jacinto fault (SJF) near Anza in southern California. Peng et al. (2008) suggest tremor observed along the SAF near Cholame was triggered by the Love-wave arrival. They showed that peaks in the envelope of the tremor signal correlated with the Love-wave peak amplitude, after applying source-station travel time corrections. Both Peng et al. (2008) and Hill (2012b) noted that Love waves preferentially trigger tremor on vertical strike-slip faults when the incident wave is approximately parallel or normal to fault strike. Several recent studies have shown that tremor is routinely triggered on the Parkfield–Cholame section of the SAF by both teleseismic and regional surface wave arrivals (Peng et al., 2008; Shelly et al., 2009). Along the SAF, tremor occurs at depths between 15–40 km depth, with the most abundant tremor occurring near the along-strike transition between the locked and creeping section under Cholame, California (Nadeau and Dolenc, 2005; Peng et al., 2009; Shelly, 2009). It is worth noting that physical conditions along crustal faults in California are likely to differ significantly from subduction-zone settings. In particular, tremor in subduction zones have been inferred to occur in regions of high pore-fluid pressures (Brown et al., 2005; Shelly et al., 2006), yet there is no obvious source of fluid along the southern SAF or the SJF at the depths where tremor has been observed. Thus, it is

important to examine the conditions needed to trigger tremor along crustal faults such as the SJF. Here, we report our observations of triggered tremor along the SJF near Anza, California. The Anza region of the SJF is an ideal location for such study as triggered tremor has previously been reported (Gomberg et al., 2008; Chao, Peng, Fabian, et al., 2012). A seismic network of surface and borehole stations provides a dense set of seismic observations necessary to identify tremor. Additionally, the long-base strainmeters at Piñon Flat Observatory (PFO) measure surface strains directly. Using the data from 44 teleseismic events, we examine whether the amplitude, frequency content, and/or orientation of the triggering surface wave controls triggering of tremor. We determine the shear stress induced by each event using the estimated strain primarily based on seismic-velocity records. The measured surface strain at PFO is then used to verify consistency and correctness of the estimated strain. In addition, we estimate the location of the triggered tremor and report its frequency and amplitude characteristics. The results are compared to triggered tremor observed previously in a variety of tectonic settings.

2.2 San Jacinto Fault Background

In southern California, the majority of the strain across the plate boundary is not solely accommodated on the SAF; instead, it is distributed across the SAF, SJF, and Elsinore faults. The surface expression of the SJF is composed of a series of widely spaced, en echelon strands with relatively complex geometry. In addition, the SJF appears to consist of several distinct fault segments according to interpretations of slip rate, historical earthquakes, background seismicity, and state of stress. From paleoseismic studies, the slip rate of SJF generally decreases from 20 mm/yr along the northwestern

segment (Kendrick et al., 2002), to 12-14 mm/yr along its central segment at Anza, (Rockwell, 1990), to 8-15 mm/yr along the southeastern segment (Sharp, 1967) (Figure 2.1).

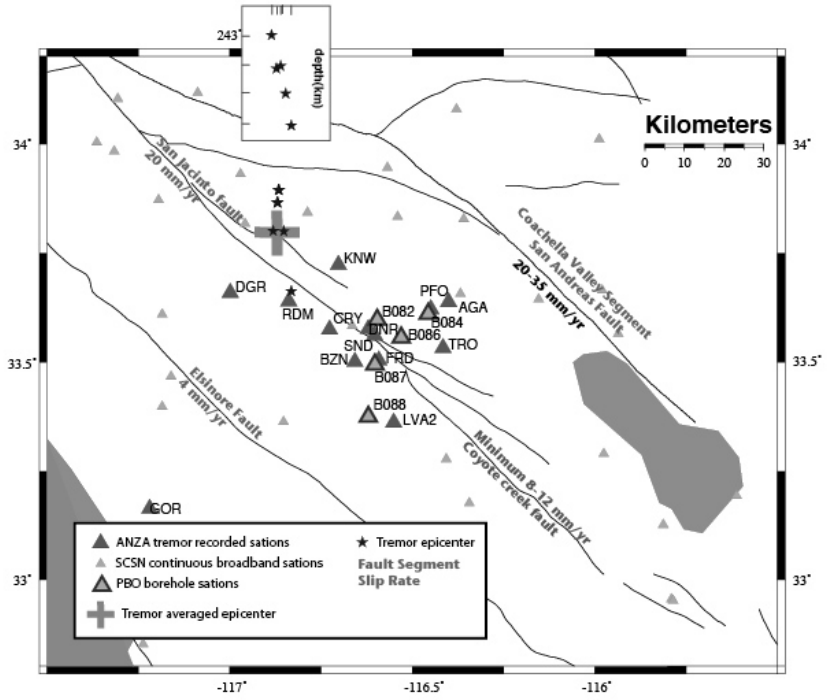

Figure 2.1 Map showing all SCSN continuous broadband stations, stations that observe tremor, and borehole seismic stations.
SCSN broadband stations are marked by small light grey triangles, stations that observe tremor are marked by dark grey triangles, and borehole seismic stations are marked by gray triangles with a black-border.Black star indicates the estimated location of each tremor LFE. The slip rates for each of the major faults are shown. Slip Rate References: Coachella Valley [Sanders, 1990], SJF [Sanders & Kanamori, 1984], southern SJF [Sanders, 1981], and Elsinore [Sieh, 1986].

Historically, the SJF has been the most seismically active fault in southern California, with a high rate of moderate to large earthquakes in the past 100-150 years (Sanders and Kanamori, 1984; Thatcher et al., 1975; Sanders, 1989). However, a 20-50 km segment near the central portion of the SJF, known as the Anza seismic gap (Sanders and Kanamori, 1984; WGCEP, 1988; see Figure 2.2), has not had a large surface-

rupturing earthquake (ML >=6.5) since 1899 (Thatcher et al., 1975; Rockwell and Loughman, 1990). The Anza Gap is bounded to the northwest by a segment that ruptured in the 1918 ML 6.8 earthquake and to the southeast by the Borrego Mountain segment that ruptured in the 1968 Mw 6.5 earthquake (Sanders and Kanamori, 1984; Thatcher, 1975; Heaton and Helmberger, 1977; Sanders, 1984; Steidl et al., 2000). Sanders and Kanamori (1984) suggested the Anza Gap segment was likely to rupture in a moderate to large earthquake because the segment had not ruptured in historic time (Thatcher et al., 1975; Sykes and Nishenko, 1984). With a strain accumulation of approximately 8–12 mm/yr, Rockwell and Loughman (1990) estimated at least 0.8 m has accumulated on the segment. The size of the future Anza seismic gap earthquake was estimated to be M 6.5 along a fault segment 20 km long and 15 km deep (Sanders and Kanamori, 1984; Rockwell and Loughman, 1990). It was suggested that the high rate of small earthquakes since 1970 at the edge of this gap indicated that the fault was critically stressed and likely to fail (Sanders and Kanamori, 1984). Although no evidence has since been found at the surface suggesting strain is being accommodated by aseismic creep (Louie et al., 1985; Vanbroskirk et al., 2011), Wdowinski (2009) inferred deep creep was occurring based on seismic and geodetic observations.

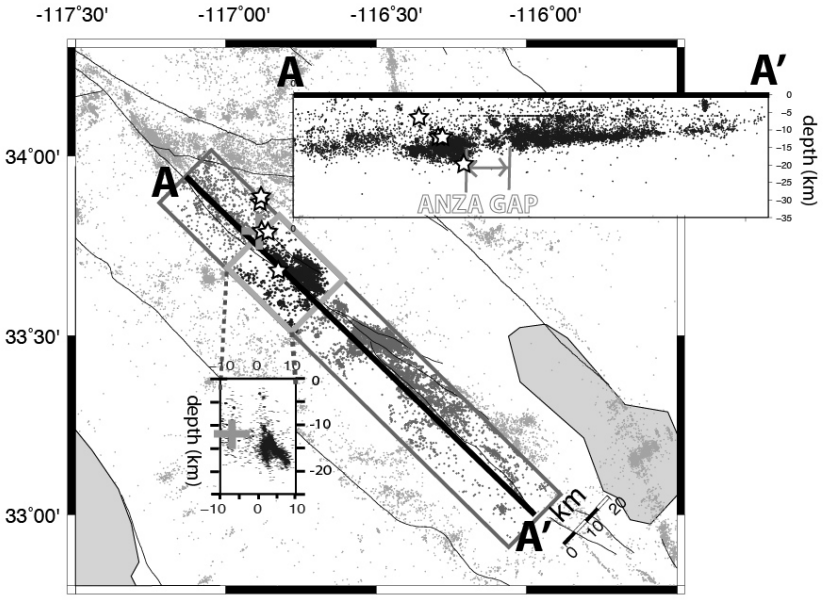

Figure 2.2 Seismicity map along the SJF.
Seismicity (small circles) from 1996-2005 is shown as reported in the SCEC catalog. Stars indicate the estimated locations of the LFE templates. Light gray cross indicates the averaged location of tremor. The upper right cross-section is a vertical profile of seismicity along A-A', a simplified surface fault trace for the SJF fault plane (N43W, vertical dip). This profile includes seismicity within 10 km of each side of A-A' (dark gray rectangular box). The depth profile at the lower-left shows seismicity particularly near the northwestern edge of the Anza Gap as indicated by the light grey box. The vertical and horizontal scales on both profiles are in km. Note that the white stars are hypocenters of tremor templates and the grey cross is the average location of tremors, which correspond to the locations in Figure 2.1.

The pattern of earthquakes along the SJF suggests distinct changes occur along fault strike, both from the seismicity rate and in the depth extent of the seismogenic zone. In Figure 2.2, we plot seismicity above M_L 2.0 from 1996-2005 (Figure 2.2). The depth of the seismogenic zone varies from about 11-12 km depth to the north to as deep as 20 km near the central section of the fault. Sanders and Magistrale (1994) reported an abrupt change in the maximum hypocentral depth of earthquakes about mid-way along the SJF. This abrupt change in hypocentral depth coincides with a change in the pattern of

seismicity from very well aligned, deep earthquakes to the south to diffuse, shallower seismicity to the north.

Several studies also suggest that the state of stress along the SJF may be quite heterogeneous. Hartse et al. (1994) analyzed focal mechanisms and found notable stress anomalies within the Anza seismic gap. They reported a significant change in orientation of focal mechanisms (maximum compressive stress $74^{o} \pm 13^{o}$ relative to fault strike, compared to $62^{o} \pm 11^{o}$ northwest and $49^{o} \pm 7^{o}$ southeast) and suggested that this may result from stronger material within the gap. More recently, Bailey et al. (2010) suggested that stress heterogeneity may be controlled by the complex fault structures. They observed two clusters of earthquakes with primarily thrust mechanisms to the northwest and strike-slip mechanisms to the southeast of the Anza gap (Bailey et al., 2010).

2.3 Data and Methods

2.3.1 Data

We examine continuous seismograms recorded along the SJF near Anza, California for triggered tremor; data from 11 surface stations, 8 of them are from Anza network and 3 from Southern California Seismic Network (SCSN). We also included 5 Plate Boundary Observatory (PBO) borehole stations (Figure 2.1). Borehole station installations were completed in 2006 and are used when available. We examined 44 large teleseismic earthquakes (Mw >= 7.4) that occurred between 2001 and 2011 at epicentral distances greater than 2000 km from Anza; this distance was chosen such that surface waves are clearly separated from the body waves arrivals. The events occur at a range of

backazimuths, from 128 to 352 degrees (see Table 2.1). Figure 2.3 shows the locations of the 44 events relative to the Anza array. We also utilize data from 17 small local earthquakes that occurred in 2002 (M_L 1.2-1.47; Table 2.2) to compare frequency spectra between tremor, noise, and local earthquakes (Figure 2.4).

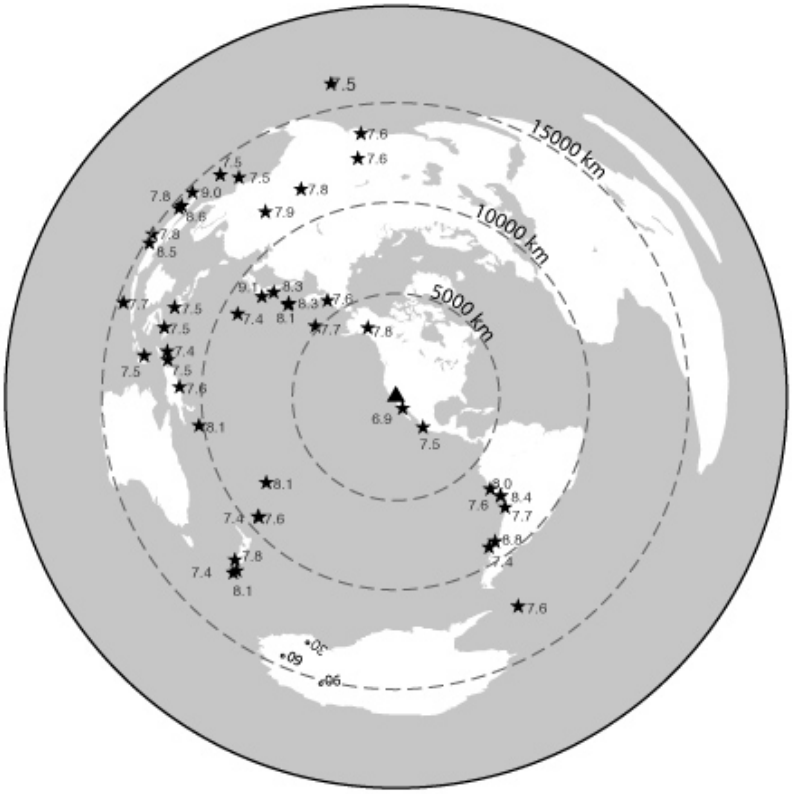

Figure 2.3 Global map of 44 teleseismic earthquakes examined.
Black stars are teleseismic earthquake epicenters with magnitudes (Mw) indicated. The triangle in the center of this map represents the approximate location of the seismic stations near Anza. The gray dashed circles mark equal distance contour to Anza every 5000 km.

#	date/time	latitude	logtitude	azimuth (degrees)	distance (km)	Mw	depth (km)	dominant period(T)	observed FP strain	observed FN strain	estimated FP strain	estimated FN strain	FP velocity (normalized)	FN velocity (normalized)	FN stress (kPa)	FP stress (kPa)
1	2001/1/26:03:16:54.9	23.6	70.2	352	13603	7.6	19.8	34	X	X	32	27	0.04	0.02	1.43	1.72
2	2001/6/23:20:34:23.3	-17.3	-72.7	133	7344	8.4	29.6	59	159	255	162	231	0.19	0.18	12.46	8.81
3	2001/7/7:9:39:1.8	-17.5	-72.5	133	7376	7.6	25.0	59	X	X	19	15	0.02	0.01	0.81	1.02
4	2001/11/14:9:27:15.9	35.8	92.9	335	11698	7.8	15.0	43	X	X	46	54	0.05	0.04	2.93	2.50
5	2002/3/5:21:16:23.3	5.9	124.3	292	12240	7.5	28.7	56	X	X	11	4	0.01	0.00	0.22	0.61
6	2002/9/8:18:44:38.3	-3.3	143.4	273	11114	7.6	19.5	33	X	X	26	26	0.03	0.02	1.40	1.43
7	2002/10/10:10:50:41.9	-1.8	134.3	279	11858	7.5	15.0	68	X	X	20	28	0.02	0.02	1.50	1.07
8	2002/11/3:22:13:28.0	63.2	-144.9	338	3820	7.8	15.0	24	X	X	870	1,315	1.00	1.00	71.04	47.43
9	2003/1/22:02:06:48.9	18.9	-103.9	139	2085	7.5	26.0	23	X	X	106	156	0.12	0.12	8.40	5.79
10	2003/7/15:20:28:37.6	-1.4	69.5	348	16373	7.5	15.0	59	X	X	14	19	0.02	0.01	1.04	0.76
11	2003/8/4:4:37:42.5	-60.8	-43.2	150	12416	7.6	15.0	69	X	X	15	17	0.02	0.01	0.92	0.80
12	2003/9/25:19:50:38.2	42.2	143.8	311	8251	8.3	28.2	66	X	X	121	66	0.14	0.05	3.59	6.61
13	2003/11/17:6:43:31.0	51.1	177.9	311	5503	7.7	21.7	48	X	X	22	17	0.03	0.01	0.89	1.19
14	2004/11/11:21:26:58.0	-7.9	125.1	279	13078	7.5	17.0	41	8	5	6	8	0.01	0.01	0.41	0.33
15	2004/12/23:14:59:30.9	-49.9	161.3	223	12275	8.1	27.5	80	X	X	121	24	0.14	0.02	1.29	6.61
16	2004/12/26:1:1:9.0	3.1	94.3	315	14789	9.0	28.6	55	X	X	264	171	0.30	0.13	9.23	14.40
17	2005/3/28:16:10:31.5	1.7	97.1	311	14724	8.6	25.8	37	61	78	57	67	0.06	0.05	3.63	3.08
18	2005/10/8:3:50:51.5	34.4	73.5	351	12376	7.6	12.0	45	20	28	26	26	0.03	0.02	1.38	1.44
19	2006/4/20:23:25:17.6	60.9	167.1	325	6056	7.6	12.0	50	46	46	41	64	0.05	0.05	0.65	0.47
20	2006/7/17:8:20:38.4	-10.3	107.8	289	14789	7.7	20.0	37	4	3	7	5	0.01	0.00	0.29	0.36
21	2006/11/15:11:15:8.0	46.7	154.3	311	7282	8.3	13.5	99	60	55	50	71	0.06	0.05	3.81	2.74
22	2007/1/13:4:23:48.1	46.2	154.8	310	7273	8.1	12.0	37	114	124	92	108	0.11	0.08	5.82	5.02
23	2007/1/21:11:28:1.0	1.1	126.2	287	12399	7.5	22.2	59	5	9	8	12	0.01	0.01	0.62	0.46
24	2007/4/1:20:40:38.9	-7.8	156.3	262	10195	8.1	14.1	41	X	X	33	29	0.04	0.02	1.57	1.79
25	2007/8/15:23:41:57.9	-13.7	-77.0	135	6746	8.0	33.8	52	63	72	75	47	0.09	0.04	2.52	4.07
26	2007/9/12:11:11:15.6	-3.8	101.0	302	14883	8.5	24.4	31	20	22	37	48	0.04	0.04	2.62	2.01
27	2007/9/30:5:23:51.5	-49.3	164.0	223	12066	7.4	12.6	19	9	7	12	7	0.01	0.01	0.39	0.68
28	2007/11/14:15:41:11.2	-22.6	-70.6	135	7943	7.7	37.6	85	14	24	22	17	0.03	0.01	0.90	1.20
29	2008/5/12:6:28:40.4	31.4	104.1	325	11602	7.9	12.8	48	48	31	47	60	0.05	0.05	3.24	2.56
30	2009/1/3:19:44:9.0	-0.6	132.5	281	11946	7.4	18.2	80	17	10	24	20	0.03	0.02	1.07	1.33
31	2009/7/15:9:22:49.6	-45.9	166.3	225	11723	7.8	23.5	59	24	16	29	18	0.03	0.01	1.00	1.60
32	***2009/08/03:18:00:06.5***	***29.2***	***-113.5***	***146***	***583***	***6.9***	***12.2***	***10***	***1497***	***1937***	***1,002***	***2,342***	***1.15***	***1.78***	***126.45***	***54.60***
33	2009/8/10:19:56:5.0	14.2	92.9	324	13834	7.5	22.0	51	9	9	9	10	0.01	0.01	0.53	0.48
34	2009/9/29:17:48:26.8*	-15.1	-172.0	237	7967	8.1	12.0	51	65	108	78	153	0.09	0.12	8.27	4.23
35	2010/2/27:6:35:14.5	-36.0	-73.2	145	8973	8.8	23.2	100	246	278	268	322	0.31	0.22	15.55	13.47
36	2010/2/27:8:1:29.8	-38.1	-75.4	148	9051	7.4	19.9	77	X	X	23	46	0.03	0.03	2.48	1.28
37	2010/4/6:22:15:19.1	2.1	96.7	312	14712	7.8	17.6	24	13	17	20	12	0.02	0.01	0.64	1.07
38	2010/6/12:19:27:0.4	7.9	91.7	322	14509	7.5	33.1	65	16	11	12	24	0.01	0.02	1.32	0.64
39	2010/10/25:14:42:59.8	-3.7	99.3	304	15007	7.8	12.0	24	4	5	5	5	0.01	0.00	0.29	0.25
40	2010/12/21:17:19:53.6*	27.1	143.8	298	9169	7.4	15.6	46	13	14	16	15	0.02	0.01	0.82	0.88
41	2011/3/11:5:47:32.8	37.5	143.1	307	8585	9.1	20.0	103	223	286	257	296	0.30	0.23	16.01	14.02
44	2011/7/6:19:3:32.5	-29.2	-175.8	229	9345	7.6	22.3	69	12	22	16	26	0.02	0.02	1.39	0.89
45	2011/10/21:17:57:28.3	-29.0	-176.2	229	9360	7.4	33.0	46	8	22	21	15	0.02	0.01	0.79	1.15

Table 2.1 44 large teleseismic events selected and examined for NVT triggering.
One regional event, the 2009 Mw 6.9 Gulf of California earthquake (#32), is included due to the large strain it induced at Anza. The back-azimuths are measured from station RDM. An X in the observed fault-parallel (FP) and fault-normal (FN) strain columns indicates that surface strain measurements are not available or not complete for the event.

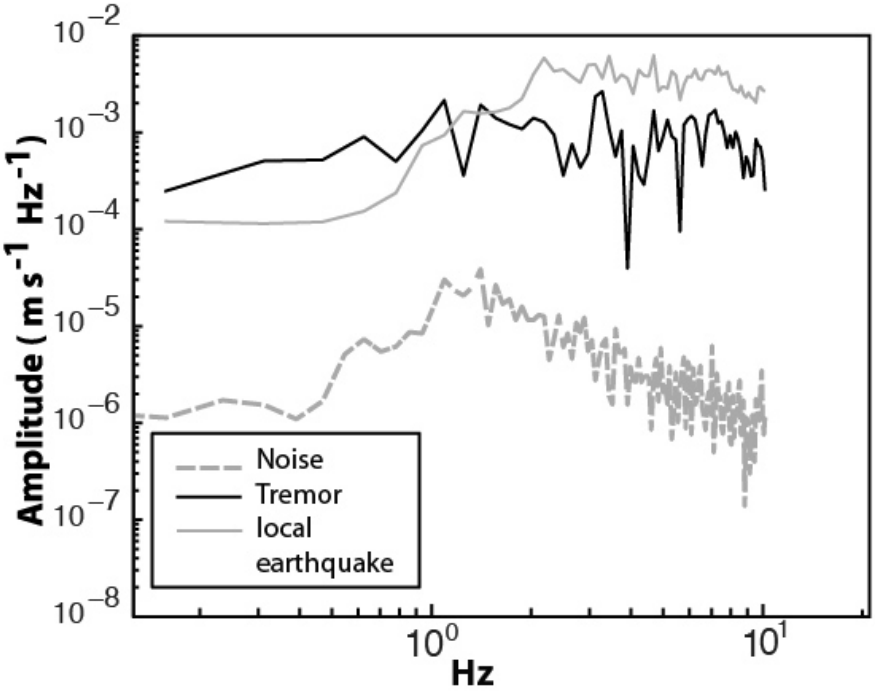

Figure 2.4 Comparison of the frequency spectra of a small earthquake, tremor and noise. These curves are taken from station RDM, north component. The spectrum of small earthquakes is averaged from displacement record of 17 local earthquakes selected in the Anza region (Table 2). The noise curve is averaged from 17 time windows before each P picks of local earthquakes. These spectra are generated from displacement records of similar time duration. Note that tremor is lacking in frequency above 6 Hz compared to the earthquake spectra. However, tremor abounds in low frequency energy below 6 Hz relative to noise. Note that record above 10 Hz (Nyquist frequency) may have artificial effect, which is not valid.

2.3.2 Tremor Identification and Template Method

To identify tremor, we visually examine a window around the teleseismic arrivals, from the onset of the P wave arrival until amplitudes return to background noise levels. We band-pass filter the data between 2-6 Hz and visually inspect the three components for tremor. By visual inspection, we find only one episode of triggered tremor that occurs during the 3 November 2002 Mw 7.8 Denali earthquake. As previous studies have indicated (e.g. Aguiar et al., 2009; Brown, 2010; Chao et al., 2012a), triggered tremor

might be obscured by background noise. To ensure that even low amplitude tremor episodes are detected, we also manually select LFE (low-frequency earthquake) templates from the tremor episode identified during the Denali earthquake. Here, we adopt the template matching method of Shelly et al. (2006). The template method assumes repeated LFEs occur close to or at the same location, therefore generating waveforms with high similarity. We select 6-second windows around times of higher amplitude tremor, e.g. LFEs, on 11 stations that record the tremor at high signal to noise ratios (Figure 2.5). We center the 6-second window on the maximum amplitude of the envelope function, assuming the high amplitude burst was coincident with the tremor S-wave arrival. To define a template, the same time window is chosen for the two horizontal components on a given station. Using this method, we initially select five templates from the Denali tremor episode. As shown in Figure 4, we verify the templates are tremor by comparing the frequency spectra of the tremor to background noise and a set of 17 local earthquakes (M_L 1.2-1.47; Table 2.2). We then cross correlate the template LFEs across the 44 time series at the station sample rate to search for repeated LFEs. We cross correlate the templates across a window that starts 1 hour before the teleseismic P-wave arrival and ends 1 hour after the main teleseismic energy has passed. Following the method of Shelly et al. (2006), we fix the move-out across the array for each LFE template during cross correlation. This fixed move-out limits detection to signals highly similar to the template LFE, requiring similar hypocenter location and source mechanism.

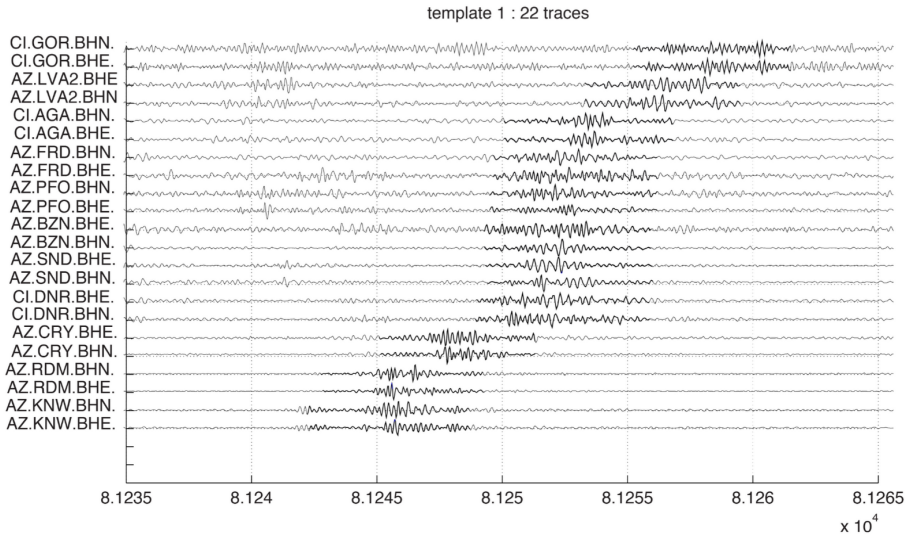

Figure 2.5 A handpicked tremor template during the Denali earthquake surface wave.
The template waveforms are shown in descending order of arrival times. The bold portion of each trace is the 6-second template window for each component (horizontal) and station. We picked the template to span the maximum amplitude of the envelope function, which is assumed to be the S-arrival of each LFE. The time of this LFE template relative to other LFEs in the tremor episode is shown in Figure 2.6(a) (gray portion). This template is used to search for repeating LFEs within the continuous time-series of the 44 teleseismic events.

year	month	day	hour	minutes	seconds	magnitude	latitude	longitude	depth
2002	1	21	17	37	23.21	1.29	33.645	-116.786	17.4
2002	2	11	5	55	15	1.21	33.984	-116.607	12.4
2002	3	2	14	41	44.82	1.21	33.713	-116.825	15
2002	4	2	15	27	21.52	1.22	33.695	-116.763	15.9
2002	5	17	3	15	0.25	1.47	33.696	-116.719	18.4
2002	5	18	7	28	9.56	1.29	33.661	-116.721	17.4
2002	5	19	15	8	9.81	1.27	33.724	-116.755	18.6
2002	6	29	13	35	3.59	1.22	33.974	-116.744	17.1
2002	7	2	11	38	18.93	1.21	33.688	-116.719	17.4
2002	8	4	22	40	7.8	1.21	33.712	-116.819	15.3
2002	8	16	2	15	41.95	1.21	33.682	-116.777	15.2
2002	9	18	0	38	40.86	1.45	33.871	-116.803	15.2
2002	10	10	10	42	21.04	1.28	33.73	-116.776	18.4
2002	11	2	3	13	17.44	1.2	33.723	-116.775	17.8
2002	11	19	11	55	10.85	1.42	33.684	-116.75	18
2002	12	12	2	44	29.17	1.2	33.678	-116.672	17.1

Table 2.2 16 local earthquakes that have hypocenters close to the estimated tremor locations and similar velocity amplitude on S arrivals.

To determine when a repeat of the template event occurs, we first sum the correlation values across the horizontal components of 11 stations (22 components in total) and then determine if that summed correlation value exceeds an assigned threshold. The threshold is set to 4.0, corresponding to a correlation value of 0.18 or higher per trace, on average. Figure 2.6(a) shows the times when the correlation value exceeds the

defined threshold for a particular template during the Denali teleseismic arrivals. We use this threshold to search for repeated LFEs during all 44 teleseismic earthquakes. It is worth noting that the template method applied here can only detect LFEs that repeat with similar source characteristics at similar locations; an LFE that occurs at a different location from the template LFEs will not be identified.

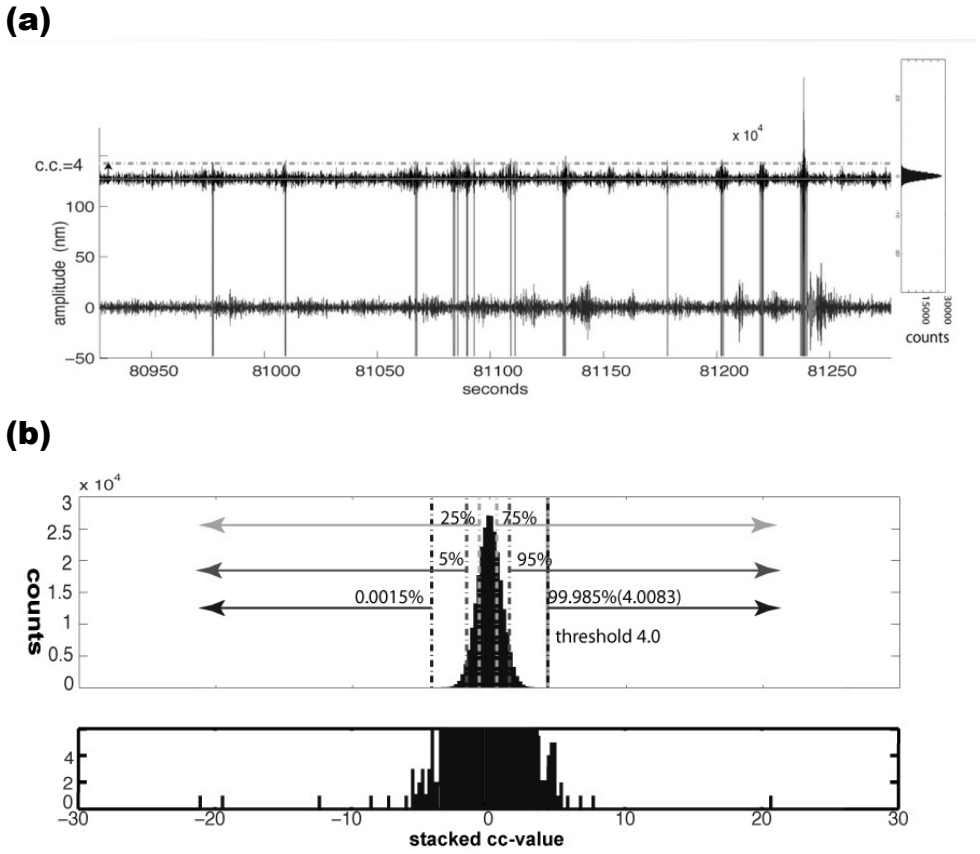

Figure 2.6 Illustration of cross correlating a template LFE across the filtered Denali time series. (a) Results after cross correlating a template LFE (Figure 4) across the filtered Denali time series. Lower trace shows the filtered time series from station KNW, component BHE. The light grey trace at time 81240 seconds corresponds to the time of template picked on this trace. Upper trace is the stacked cross correlation values (cc-values) versus time. The stacked cc-values result from cross correlating the template with a fixed relative move-out on each trace and summed over 22 components. Gray vertical lines indicate the time when cross correlation is above the threshold cc-value of 4.0 (horizontal grey dashed line), which we declare a detection. Note that the stacked cc-value is 22 when LFE template exactly matches the time series. The overall stacked cc-value has a normal distribution (small box at the right to black trace; see Figure 6b for details). (b) Histogram of stacked cross correlation values (cc-values) divided into 200 bins. The histogram shows the cc-values are normally distributed. The threshold cc-value of 4.0 only occurs in 0.0015% of the window. The dashed lines indicate probability of occurrence for different thresholds. The lower panel has enlarged scale on the y-axis in order to show the limited number of very high cc-values, which correlate to times near the tremor template.

2.3.3 Source Location

To estimate the location of tremor observed during the Denali earthquake, we manually pick the maximum amplitude of the LFE, assumed to be S-wave arrival, on each of the 11 stations. S-wave arrivals are picked on each of the five template events. The source location of the tremor is not precisely known because lower amplitude P-wave arrivals are not visible and S-wave picks are poorly constrained due to their emergent nature on the tremor records. Stacking the tremor templates did not significantly improve the visibility of the phase arrivals, so we instead chose to locate each of the templates independently to more precisely estimate location errors. We use the generalized-earthquake-location (GENLOC; Pavlis et al., 2004) package in Antelope to locate the LFEs. We adopt the velocity structure from the Southern California Earthquake Center Community Velocity Model (SCEC CVM-H 6.2; Suess and Shaw, 2003; Plesch, 2011). The velocity model contains 14 layers with 2-km depth intervals and a lateral extent of 20 km across the SJF fault plane, as defined by SCEC Community Fault Model (SCEC CFM; Plesch et al. 2007). Average error estimates from Antelope are approximately 0.1 km horizontally and 1 km in depth, but these do not reflect the true errors due to the emergent nature of the arrivals. More accurate estimates of the error in tremor locations are determined by simply examining the range of locations determined for the five LFE templates (Figure 2.1). Since the templates all correlate highly with each other, we can reasonably assume they come from a small source region. The average hypocentral location for the five events is (33.87, -116.98) with a standard deviation in

horizontal location of 7.5 km. The depths of the tremor are poorly constrained due to a lack of P-wave arrivals and vary between 5 and 21 km depth.

2.3.4 Surface Wave Stress and Strain Estimates

For each of the 44 teleseismic earthquakes, we measure the peak velocity amplitude of the surface wave first in the radial and transverse directions, to correlate tremor to the Rayleigh and Love wave arrivals. We then rotate the horizontal component seismogram to 317° (SJF fault strike) and 43° (fault normal). In doing so, the peak shear stress, contributed primarily by the Love wave (Hill, 2012a; 2012b), is resolved into the fault parallel and fault normal directions. To estimate the peak amplitude in the tremor region, we use peak amplitude measurements on station RDM as it is both close to the estimated tremor epicenters and has a high signal-to-noise ratio. Following the work of Mikumo and Aki (1964), Gomberg and Agnew (1996) and Gomberg and Johnson (2005), we can derive the strain by partial derivative of the displacement:

$$\varepsilon = \frac{\delta u}{\delta x} = \frac{\delta u}{\delta t}\frac{\delta t}{\delta x} = \frac{\delta u}{\delta t}\frac{1}{C} \tag{2.1}$$

where ε is the strain in the direction of propagation or normal to it, u is displacement, $\frac{\delta u}{\delta x}$ represents strain in the direction x, $\frac{\delta u}{\delta t}$ is the particle velocity observed on seismic velocity record, and $\frac{\delta x}{\delta t} = C$, is the local phase velocity of Rayleigh wave or Love wave. Note that the incoming surface wave is assumed to be a plane wave that propagates at one phase velocity, C, in the direction of propagation.

We use a phase velocity of 4.0 km/s, averaged from the observed phase velocities that range from 3.5-4.5 km/s. The phase velocities (C) are determined from the move-out of phase arrivals at several stations. We compare the strain estimates from the velocity seismograms with the strains observed at surface strainmeter PFO when fault normal and fault parallel strain records are available (Table 2.1). The peak velocities obtained at station PFO and RDM are similar, with less than 0.1% deviation; the distance between these two stations is negligible compared to the source-receiver distances (~1/100 of the distance between source and receiver) (Figure 2.7). The surface strains estimated from the seismic data are consistent with the measured surface strains with a linear regression fit of R^2=0.99 (Figure 2.7).

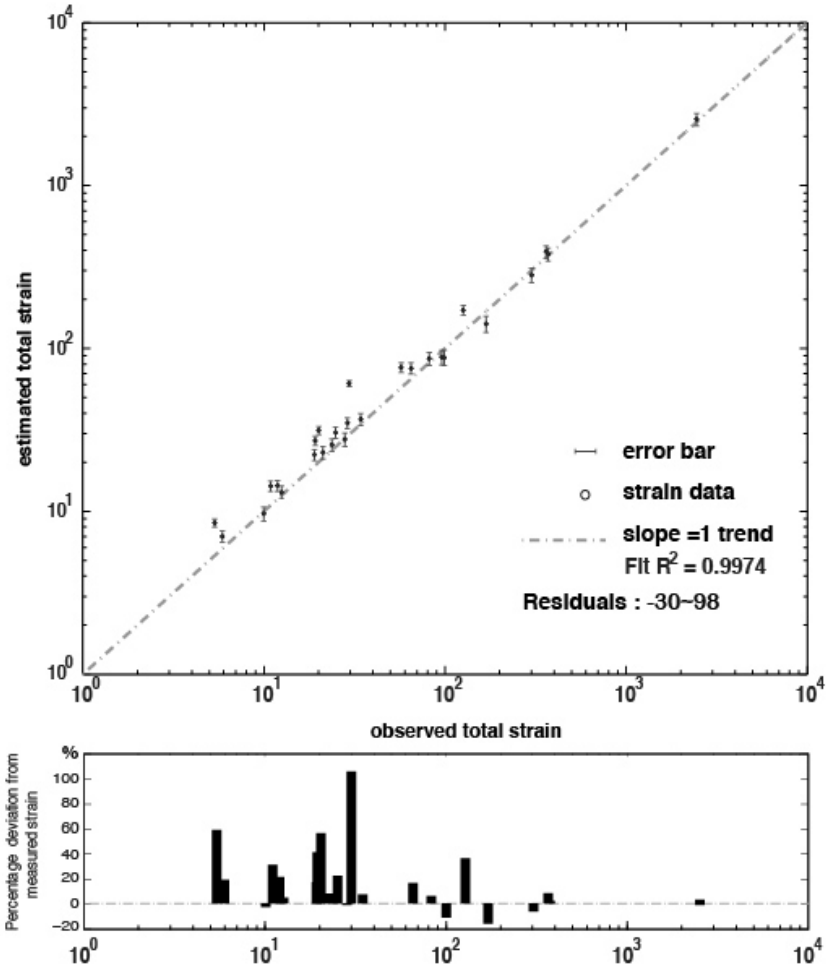

Figure 2.7 Comparison between the observed strain from strainmeter PFO and strain estimated from seismic velocity records.
(Top) Observed strain from strainmeter PFO and strain estimated from seismic velocity records on a log-log plot. The dashed grey line represents a slope of one. Error bars show the estimated uncertainty. The error bars on the y-axis represent an average 18% uncertainty that results from the variation of phase velocity (3.5-4.5 km/s). The total strain is calculated as the vector sum of fault normal and fault parallel strains. The R^2 value indicates how well the estimated total strains fits to a one-to-one relationship. (Bottom) Residuals between the estimated strain and the one-to-one trend line. Note the percentage values are plotted on a linear-log scale to match the logarithm x-axis on the top plot.

2.4 Results

2.4.1 Observed Tremor

In initial analysis of the 2002 Denali earthquake, we find the highest amplitude bursts are detected as repeats of the template event (Figure 2.6(a)). In fact, all of the selected template events from the Denali earthquake are found to correlate highly with each other suggesting a single, small source region for the tremor. We also determine the statistical significance of the summed correlation threshold using the Denali event as an example. During the 3.5-hour window around the Denali earthquake, we cross correlate a 6-second window at the sample rate (20 samples per second) resulting in over 25,000 correlation windows. The summed cc-values are normally distributed and 99.98% of the windows fall outside of the defined threshold (4.0). In other words, 0.02% of the windows exceed the summed threshold and are considered a repeated LFE. Extending the analysis to all 44 teleseismic earthquakes confirms only one episode of triggered tremor; only the 2002 M_w 7.8 Denali earthquake results in triggering of tremor. This tremor episode is composed of 12 LFE bursts in a 300 second period during the passage of the main surface wave arrivals (Figure 2.6(a)). The arrivals of these tremor bursts are slightly delayed compared to the peaks and troughs of the triggering wave. And, as shown in Figure 2.8, the amplitude of each tremor burst is not clearly modulated by the amplitude of the triggering surface wave.

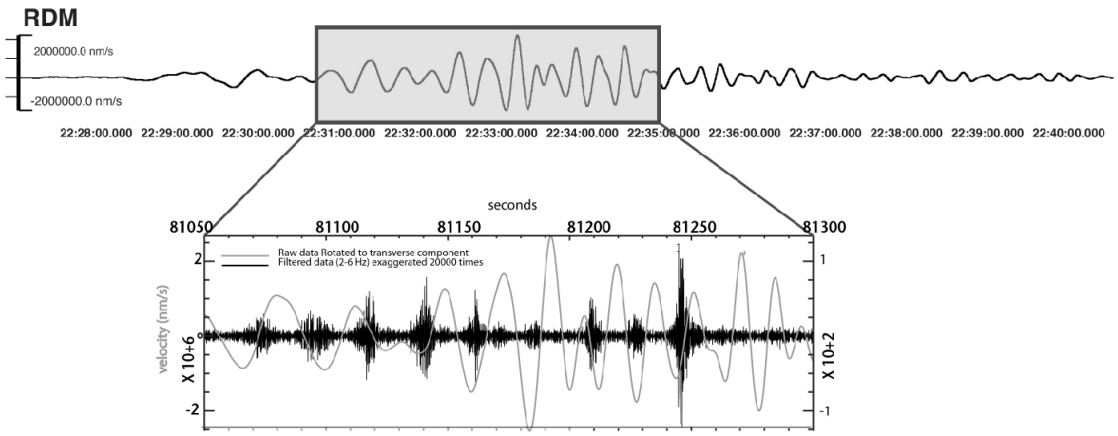

Figure 2.8 Example waveform of the surface wave of 2002 M_w 7.8 Denali earthquake and the filtered data illustrating triggered tremors.
Upper trace shows an example waveform during surface wave of 2002 M_w 7.8 Denali earthquake showing the original surface wave data (upper black trace) and the section enlarged below (shaded box). The lower trace shows the data filtered between 2-6 Hz (black trace) with clear tremor arrivals, and the original surface wave data (grey trace). Traces shown here are recorded on the transverse component of station RDM.

2.4.2 Triggering Factors: Amplitude and Period

Next, we examine whether a given amplitude and/or period of surface wave is required to trigger tremor. We consider the peak strain amplitude measured on surface waves is representative of the peak stresses on the fault. Here, we assume that when the peak stress exceeds a given threshold tremor (e.g. slip) will occur on the fault. We report only the peak stress, as it is a simple metric to compare the teleseimic events. We find that the 2002 Denali earthquake has high strain amplitudes in both fault-parallel and fault-normal directions. In Figure 2.9, we show polar plots of the peak stress on fault parallel and fault normal directions, versus back azimuth for all 44 teleseismic events estimated from velocity records (see Table 2.1). Most of the events produce significantly

lower strains than the Denali event; however, the 2009 M_w 6.9 Gulf of California earthquake produced strains approximately 1.5 times those of the Denali earthquake.

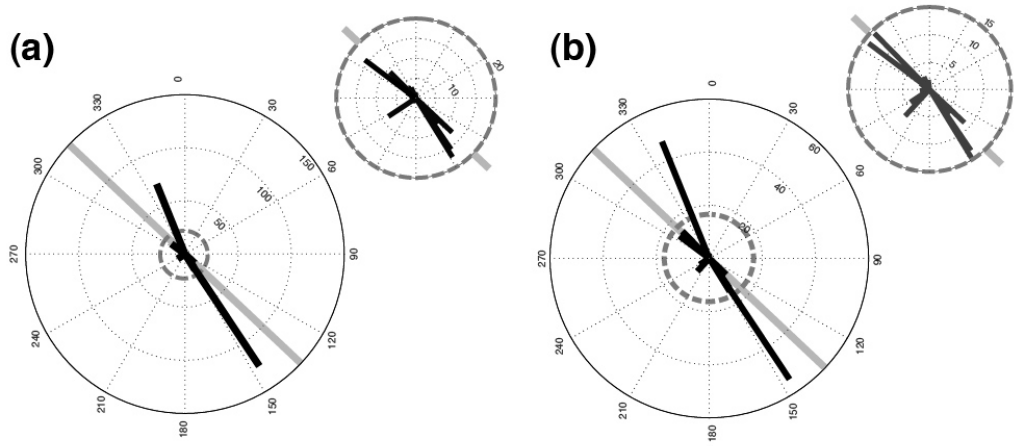

Figure 2.9 Polar plots of peak shear stress versus event back azimuth for the 44 teleseismic events.
Such shear stresses are estimated from seismic wave velocity in (a) fault-parallel and (b) fault-normal direction. Large polar plots show all 44 events scaled to the maximum observed shear stress. Smaller polar plots show the smaller strain values that are not visible on the full-scale plots. Note that the maximum radius of each circle is different, but the unit is in kPa. The light gray lines indicate the strike of the SJF (317 degrees).

We also determine the dominant period of the surface waves for each of the 44 teleseismic events. The dominant period is estimated within a window that encompasses the initial arrivals of the Love and Rayleigh wave. The dominant period given in Table 2.1 is defined as the highest peak in the frequency spectrum within the time window around the surface wave. The uncertainty in the measured dominant period shown in Figure 8 is defined as the range of periods with amplitudes equal to or greater than 60% of the peak amplitude. Windows encompassing just the Love or Rayleigh waves result in similar estimates of the dominant period as those determined for the combined window.

Figure 10 shows the peak amplitude versus dominant period for all 44 teleseismic events. The dominant period of the 2002 Denali earthquake is 23 seconds, which is less than the mean period of the 44 teleseismic surface waves (54.5 seconds) but not the shortest period observed.

2.5 Discussion

2.5.1 Triggered Tremor Source

Over a ten-year period, between 2001 and 2011, we observe only one episode of tremor triggered by teleseismic arrivals along the SJF near Anza, California. A five-minute long tremor episode comprises 12 tremor pulses occurred during the passage of teleseismic surface waves from the 2002 M7.8 Denali earthquake. The tremor episode was well recorded by 11 surface seismometers. Manually selected tremor templates around three tremor pulses, or LFEs, were found to be highly correlated with each other suggesting that the tremor originated in a small source region. Chao et al. (2012a) visually examined teleseismic waveforms on a single station in the Anza region (RDM) from year 2001 to 2009 and also suggest only one episode of triggered tremor occurred. However, they did not conduct detailed analysis of the tremor using template LFEs or locate the hypocenters.

Tremor templates locate on, or very close to, the SJF, but the depth of the tremor is not well constrained. Within errors, the tremor locates to the northwestern end of the Anza gap, where there is a distinct change in the seismicity (Figure 2.2) (e.g. Thatcher et al., 1975; Sanders and Kanamori, 1984). Seismicity rates within the Anza gap are lower

than adjacent sections of the fault (Sanders and Kanamori, 1984); although, the SJF has higher rates of moderate to large earthquakes compared to the other major strike-slip faults in the region, including the Elsinore and SAF (Petersen and Wesnousky, 1994). In addition, along the Anza section of the SJF, the fault exhibits significant geometrical complexity, with multiple fault strands visible at depth in a cross-section of the seismicity (Figure 2.2).

There is also a step in source depths along strike of the SJF, with earthquakes in the Anza Gap and farther south generally occurring shallower than 15 km and earthquakes northwest of the gap occurring at depths up to 20-25 km (Figure 2.2). Within the uncertainties in the estimated tremor source depths it is difficult to constrain whether the tremor is occurring at the same depth or deeper than the background seismicity. Along the SAF near Parkfield, currently the only other strike-slip fault where tremor has been well-established based on data from a locally dense array, the tremor is estimated to occur below the main seismogenic zone between 15-40 km depths (Nadeau and Dolenc, 2005; Peng et al., 2008; Peng et al., 2009), with more precise locations around 25 km (Shelly, 2009). Tremor observed both on strike-slip faults and along subduction zones are typically located below the main seismogenic zone, in the transition between the shallow, locked fault and deeper, creeping portions of the fault (e.g. Ito et al., 2007; Schwartz and Rokosky, 2007).

2.5.2 Stress Amplitude Required for Triggering

The dynamic stress change induced by surface waves (e.g. ~10 kPa; Hill, 2008; Rubinstein et al., 2008) is typically a small fraction of the background lithospheric stress

(1-100 MPa; Kanamori, 1980; Rubinstein et al., 2010). However, studies have shown that earthquakes (e.g. Hill et al., 1993; Gomberg et al., 2003; Prejean et al., 2004) and, more recently, tremor (e.g. Rubinstein et al., 2007; Miyazawa et al., 2008; Peng and Chao, 2008) can be triggered by passing teleseismic waves. The maximum velocity amplitude measured on the transverse component of station RDM is 3.48 mm/second. Thus, from Equation 1, the peak shear strain is 1.32 mstrain. This value is on the same order as strain values reported to trigger tremor in previous studies (Miyazawa and Mori, 2006; Miyazawa et al., 2008; Rubinstein, 2009).

Next, we estimate the maximum shear stress using $\tau_{max} = 2\mu(\frac{\delta\mu_x}{\delta y})$. We estimate the shear modulus, m, as 27.9 GPa from the shear wave velocity given in the Southern California Earthquake Center Community Velocity Model (SCEC CVM-H 6.2) (Suess and Shaw, 2003; Plesch, 2011). The peak shear stress parallel to fault strike is approximately 35 kPa. To constrain the peak shear stress necessary to trigger tremor, we also estimate the peak shear stress induced by the 2010 M_w 7.4, the aftershock of M_w 8.8 Maule earthquake, which has next highest peak velocity compared to the Denali earthquake but did not triggered tremor. We estimate the peak shear stress as 17 kPa. Thus, if a purely amplitude based threshold is necessary to trigger tremor along the SJF, the threshold is likely to be between 17 kPa and 35 kPa.

The threshold we obtained is at the high end of most values previously reported for triggered tremor along subduction zones. Most studies report the dynamic stress threshold sufficient to trigger tremor using peak ground velocity (PGV) rather than strain or stress (e.g. Rubinstein et al., 2007, 2009; Chao et al., 2012a, 2012b). In Cascadia on

Vancouver Island, the peak stresses reported to trigger tremor were 43 kPa for Love wave and 12 kPa for Rayleigh wave, based on the peak velocity amplitude measures (Rubinstein et al., 2007). In Taiwan under the central range detachment, Peng and Chao (2008) first reported that Love waves from the 2001 M_w 7.8 Kunlun earthquake triggered tremor with an estimated shear stress of ~60 kPa. However, more recent observations of tremor triggered during several teleseimic events suggest the minimum shear stress required may be as low as 7-8 kPa (Chao et al., 2012b). Miyazawa et al. (2008) reported that the 2008 M_w 7.9 Wenchuan earthquake triggered NVT in Shihoku, Japan, with shear stress change on the order of 30 kPa, and normal stress change of 40 kPa. These stress changes are estimated at tremor source depth, around 30 km. According to Hill (2012b; Appendix), the shear strain decreases by, at most, 12% from surface to 15 km depth, for a 20-second period Love wave. Even with such decay with depth, the stress changes Chao et al. (2012b) report for Taiwan would still be lower than our estimate of stress changes along the SJF.

We also compare our estimated triggering threshold to previous studies of triggered tremor along the SAF, which may be a better analog to the SJF than subduction zone settings. During the Denali earthquake, Peng et al. (2008) examined triggered tremor on the SAF and estimated peak shear stress changes of approximately 10-20 kPa, at the tremor source depth. This shear stress change is smaller than what we estimate here for the SJF (17-35 kPa). In a more extensive study, Peng et al. (2009) examined 31 teleseismic earthquakes and found 10 examples of triggered tremor; they estimate the threshold required to trigger tremor along the SAF near Cholame is ~2-3 kPa. Hill et al.

(2012c) report that the 11 March 2011 M_w 9.0 Tohoku earthquake triggered tremor along the Parkfield section of SAF; with an estimated peak dynamic Coulomb stress of 0.7-10 kPa. And, Thomas et al. (2009) report modulation of tremor amplitudes by tidal stresses on the order of 0.1 kPa. Chao et al. (2012a) determined the strain triggering thresholds of tremor for both northern and southern California. To appropriately compare the triggering thresholds, it is necessary to report the thresholds in consistent method and unit (e.g. stress). We converted the PGV thresholds reported in their study (Figure 5; Chao et al., 2012a) to stress using method described in section 3.3. The peak stress thresholds are approximately 27, 1.4, and 34 kPa for northern, central, and southern California, respectively. The threshold we obtain here for the SJF (17-35 kPa) is in good agreement with the 34 kPa reported in their study for the same section of the SJF. Thus, the SJF appears to require a higher stress threshold to trigger tremor than the well-studied SAF in central California. The higher stress threshold combined with the infrequent occurrence of triggering may suggest that material properties along the SJF are not as favorable for tremor production as in other locations. More specifically, in contrast to the relatively weak Parkfield-Cholame section of SAF (e.g. Carpenter et al., 2011), the strength of the SJF fault may be greater. This is also suggested by the fact that there is minimal direct evidence for aseismic creep or slow-slip in this region.

It is worth noting that we do not observe a clear modulation of the tremor amplitude as the amplitude of Denali surface wave changes. This is in contrast to triggered tremor observed at Parkfield or along subduction zones, where the tremor amplitudes appear to be modulated by small stress perturbations (e.g. tides, Rubinstein et

al., 2008; Thomas et al., 2009; teleseismic waves, Chao et al., 2012a, 2012b). This may suggest that the SJF has a less well-developed fault core (e.g. higher coefficient of friction), lower pore fluid pressure (e.g. higher effective normal stress) or is not as critically stress.

2.5.3 2009 M_w 6.9 Gulf of California Earthquake

While the amplitude of induced shear strain during surface waves may play an important role in triggering tremor, whether this factor solely controls the triggering of tremor remains an open question. In the case of earthquake triggering, Gomberg and Johnson (2005) suggest that strain amplitudes that exceed a threshold may be a critical, but not the only condition necessary to trigger earthquakes remotely. However, they suggest that triggering is not a function of the dominant period of the imposed stress. In order to validate whether this is true for tremor, we examine a regional earthquake that induces peak strains larger than those observed during the 2002 Denali earthquake. The 2009 M_w 6.9 Gulf of California earthquake occurred significantly closer to the Anza array (583 km) than the 44 teleseismic events that we evaluated in the previous sections.

The peak strain observations from the Gulf of California earthquake are 1937 and 1497 strain in the fault normal and fault parallel directions, respectively (Table 2.1; shaded column). These strains, estimated from seismic velocity records, are ~1.5 times larger, on average, than those induced by the 2002 Denali earthquake (Table 2.1). However, the 10.2 seconds dominant period of this event is significantly shorter than the dominant period during the Denali earthquake and is also the shortest period observed of all the events examined (Figure 2.10). Surface waves with short dominant periods decay more

rapidly with depth. So, we expect a 30% decrease in amplitude at 15 km depth for a Love wave with a dominant period of 10 seconds, compared to a 12% decrease for a dominant period of 20 seconds (Hill, 2012b; Appendix). However, the estimated strain induced by the 2009 Gulf of California earthquake at the estimated tremor depths is still ~1.4 times larger than strain induced by the 2002 Denali earthquake. While the 2009 Gulf of California earthquake induces larger strains, it does not trigger any observable tremor in the Anza region. If exceeding a given strain threshold were the only condition necessary to trigger tremor, then we would expect to have observed tremor during this event.

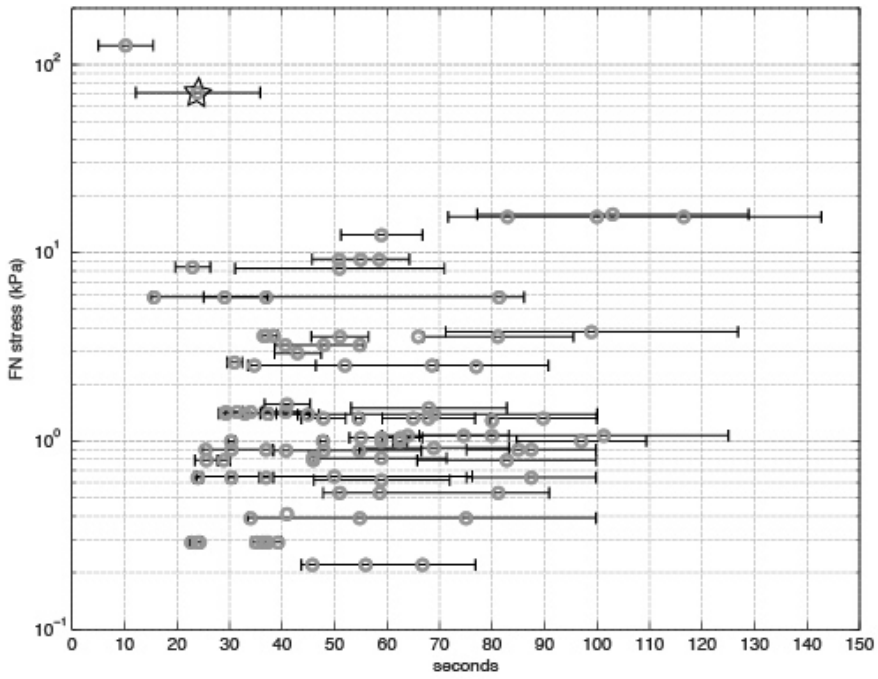

Figure 2.10 Peak shear stress versus dominant periods.
Peak stress is estimated from observations at seismic station RDM. The error bars indicate uncertainties of dominant periods measured from the frequency spectra (see text in the section of triggering factors: Amplitude and period). The star highlights the 2002 Denali earthquake that triggered tremor.

2.5.4 Dominant Period Required for Triggering

Among recent tremor studies, the period of the incoming surface wave is also considered a crucial factor in remote triggering of tremor (Hill, 2010; Rubinstein et al., 2009; Chao et al., 2011, 2012a). Rubinstein et al. (2009) show that tremor-triggering events have predominant periods between 20-100 s along the Cascadia subduction zone. Chao et al. (2012b) suggests that periods above 30 seconds do not trigger tremor on the detachment fault beneath Taiwan. For low angle thrust faults in subduction zones, triggered tremor were observed during Rayleigh wave with 10-30 second periods (15-30 seconds for southwest Japan, Miyazawa et al., 2008; ~20-40 seconds for Cascadia, Rubinstein et al., 2009; 10-30 seconds for Taiwan, Chao et al., 2012b). Along the SAF at Parkfield, surface waves of 20-30 second period trigger tremor, although the exact values for each event were not documented (Peng and Chao, 2008). We select teleseismic earthquakes with surface waves of a wide range of dominant periods (18.5-103 seconds; Table 2.1 and Figure 2.10). Only one observed triggered tremor episode is observed and triggered by Love wave with a period of 23.5 seconds period; this period falls within the range observed in previous studies. The 2009 M_w 6.9 Gulf of California earthquake induced the highest strains, but had the shortest observed surface wave periods. And, the 2010 M_w 7.4, the aftershock of M_w 8.8 Maule earthquake induced relatively high strains, but had a relatively long period surface waves (76 seconds). Neither of these events triggered tremor in Anza region. Based on these observations, tremor in Anza region may respond to dynamic stress change that is dependent not only on exceeding a certain amplitude threshold, but also within a specific period range. However, further

observations of tremor triggered by large teleseismic earthquakes are needed to further constrain the stress threshold and range of periods for this region.

2.5.5 Love Wave Triggering

We examine whether the tremor episode that occurs during the Denali earthquake was initiated by Love or Rayleigh energy. The horizontal components are rotated to radial and transverse directions to identify the Love and Rayleigh wave arrivals. We then plot the particle motion of the surface waves for several windows around the tremor episode. We show the onset of the tremor closely matches the Love wave arrival (Figure 8). And, the particle motion plots show energy primarily in the transverse direction at time of the initial tremor onset (Figure 2.11). Tremor continues after the Rayleigh wave arrival, but the peaks in the tremor are not clearly modulated by the larger Rayleigh wave amplitudes. Therefore, it is most likely that the tremor is triggered primarily by the Love wave.

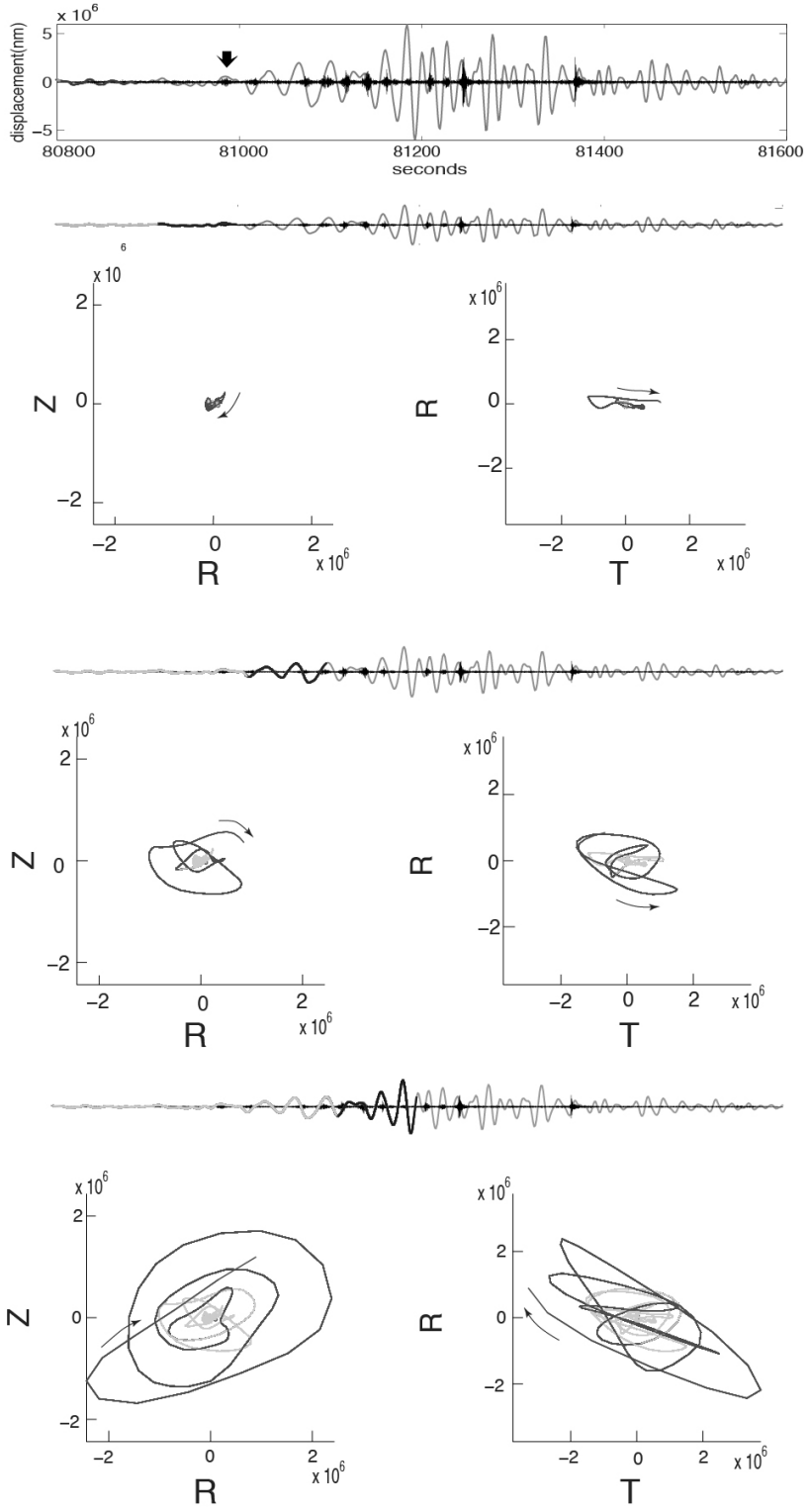
x 10^6
displacement(nm)
seconds
Z
R
T

Figure 2.11 Particle motion plots of the displacement records during different windows of the surface wave arrivals.
Upper plot shows the surface wave record of Denali earthquake rotated to the transverse direction (gray trace) and the up-scaled, filtered trace (black trace) The bold black arrow indicates the start of clear tremor arrivals detected manually and by cross correlation. The lower plots show the particle motion for three consecutive time windows. Gray and black waveform traces are as described above. The heavy black portion of the trace corresponds to the 40-second window used to plot the two particle-motion plots and the light gray trace shows the previous 60 seconds. The thin black arrows on the particle motion plots indicate the direction of motion at the end of the 40-second window. The two particle-motions are (left) in the vertical (Z) and radial (R) directions (to identify Rayleigh arrivals), and (right) in radial (R) and transverse (T) directions (to identify Love wave arrivals).

Hill (2012a) examined how the triggering potential of Love and Rayleigh wave varies with back-azimuth, for vertical strike-slip faults. For the idealized case, the Love wave triggering potential is at a maximum when the back azimuth is parallel or normal to fault strike and minimized at 45 degrees to fault strike (Hill, 2012a). The Denali earthquake has a back-azimuth of 338 degrees, which is approximately 18 degrees from the fault parallel direction (strike 320 degrees). If we examine the 2009 M_w 6.9 Gulf of California event, the only other teleseismic earthquake with larger amplitude of surface wave arrivals, we find that the back azimuth was also favorably oriented relative to the fault strike. This event had back-azimuth of 146 degrees, approximately 16 degrees from fault parallel. Thus, the back azimuths of these two events were favorable to trigger tremor. Triggered tremor was only observed during the Denali earthquake again suggesting amplitude was not the single controlling factor.

2.6 Conclusion and Summary

Over a 10 yr period, between 2001 and 2011, we observed only one episode of tremor triggered by teleseismic arrivals along the SJF near Anza, California. A 5 min long tremor episode comprising 12 tremor pulses occurred during the passage of teleseismic Love waves from the 2002 M 7.8 Denali earthquake. The tremor episode was well recorded by 11 surface seismometers. Manually selected templates from the tremor pulses, or LFEs, were found to be highly correlated with each other, suggesting that the tremor originated in a small source region. Although our estimate of tremor depth is not well constrained (5–21 km depth), the triggered tremor or LFEs in Anza appear to be

shallower than observed in other regions. Out of all the earthquakes examined, Denali-earthquake surface waves (Love waves) had the second-highest peak shear stress and the second-longest dominant period (22.8 s). This suggests that high peak stress is an important, but not sufficient, condition to trigger tremor and that the dominant period of the surface waves may also play a role. Triggered tremor appears to occur less frequently along SJF compared to other regions that are known to have tremor. And the peak shear stress required to trigger tremor is higher than most other regions where tremor are reported. This is likely related to the specific frictional properties of the SJF fault in this location, which result in only occasional tremor. Alternately, as the overall slip rate along the SJF fault is lower than the SAF, for example, this may result in relatively infrequent triggered tremor.

Chapter 3 Enhanced Imaging of non-volcanic Tremor at the Parkfield-Cholame Section on San Andreas Fault Using a mini-array

3.5 Introduction

3.1.1 Remotely Triggered Tectonic Tremors

The minimum shear stress required to trigger NVT has been reported in many places where the triggered NVTs were observed (Nadeau and Guilhem, 2009; Chao et al., 2011; Chao and Peng, 2012; Peng et al., 2013; Wang et al., 2013; Fuchs et al., 2014). It is important to know the shear stress threshold for triggering because it implies the in-situ stress condition on the fault. In particular, we can also obtain partial information about the strength of the fault when the shear stress threshold for triggering of NVT or earthquake is known. Common definition of the strength of a fault is that how durable the fault can resist increasing shear stress until failure occurs. If the threshold is high for triggering, the difference between background stress and the yield stress is large. Conversely, low threshold indicates the difference between background stress and the yield stress is small. It could be that the fault is quite close to failure, or the background yield stress for the fault is so low that a small amount of shear stress can surpass it easily. In the later case, it would support, for example, the 'weak fault' scenario (Rice, 1992; Lockner et al., 2011; Carpenter et al., 2011) that gouge and/or high pore-fluid on the fault decreases the yield stress of SAF significantly. The shear stress from tectonic loading is minute (~1-5 Pa/day) that the spontaneous failure of a fault due to such stress is on a fairly long-term scale, despite other external loadings. The consequence of such slow

stress loading takes years to hundreds of years to observe. Conversely, the observations of triggering of NVTs provide exceptional chances to reveal the stress loading and failure process in a shorter time scale. The triggering events usually apply shear stress on the scales of several kPa for minutes, which is much higher than tectonic loading (~<5Pa /day). It has been suggested that the NVTs are sensitive to small shear stress perturbation (~tens kPa) due to low effective normal stress resulted from high pore-fluid at the tremor source (Brown et al., 2005; Shelly et al., 2006). Inspired by such possibilities, observations are necessary to constrain the threshold shear stress that triggers NVT . In particularly, the Parkfield-Cholame section of SAF has had multiple studies of triggered NVT, owing to its abundant number of NVT including ambient and triggered NVTs. It is a good candidate of location to commence observation of the minimum threshold of shear stress for triggering with innovative methods and data, which has not been implemented before.

Peng et al. (2009) visually observed 31 teleseismic earthquakes of large magnitude (M_w >= 7.5) and found 21 triggered NVT along the Parkfield near Cholame on the SAF. They inferred the triggering threshold for NVT to be ~2-3 kPa, based on the measurement of peak ground velocity (PGV). Rubinstein et al.(2009) examined the data during and immediately after 30 teleseismic large earthquakes (M_w >=7.0) and 17 regional earthquakes (M_w >=6.0) on the border region of Cascadia. They found 4 triggered NVT among all events. The smallest peak shear stress inferred among the 4 triggering wave for the triggered tremor they reported is ~7.7 kPa ($1x10^{-4}$ m/s PGV). Chao and Peng (2012) used the same approach to compare the triggering threshold of the

triggering of tremors in California. They visually inspected 12 triggered tremors out of 42 large (M_w >= 7.5) earthquakes along SAF and SJF. In northern and southern California, there were not clear thresholds for the lack of triggered NVT among all 42 events. Meanwhile, in central California along Parkfield-Cholame section of SAF, there were 12 triggered tremors, suggesting the threshold fell at ~0.03 cm/s PGV. Such value of PGV converts to ~22.5 kPa with a shear modulus of 30GPa and method provided in Chapter 2 (equation 2.1). Similarly, Guilhem et al. (2010) observed 4 occurrences of triggered NVT out of 99 regional earthquakes (M_L >= 5; ~100km distance) in the same region. They filtered the data to higher frequency band (20-50 Hz rather than the general 1-15 Hz) to avoid coda interference with tremor detection. They visually inspected and searched for the triggered NVTs, while the inferred minimum triggering dynamic stress is ~1 kPa. Their study suggested that tremor triggering by earthquake at regional scale does occur and the threshold of shear stress is reduced.

The definition of tremor and the detection methods varies among different studies. The studies described in previous paragraph all used visual inspection to identify NVT, which can be as precise as to discriminate each LFEs within ETS episodes from local earthquakes or noise. Some other studies (e.g. Nadeau and Dolenc, 2005) define one occurrence of NVT as one episode of tremors consisted with multiple LFEs, because they detected such episodes using cross-correlation of the waveforms or envelope functions on large dataset. Without visual verification, such detections could under-estimate the rate of individual NVT. Or, the reported number or rate of NVT is in units (e.g. hours/day; mins/month) hardly comparable with other studies which are reporting LFEs. Among the

different detection methods, the ability to detect NVT also varies. These details all affects the threshold of shear stress required to trigger NVT that was reported in different studies.

3.1.2 Tremor Detection Methods

Visual inspection is still the most authentic way to report the occurrence of NVT (e.g. Peng and Chao, 2008; Peng et al., 2009), since the characteristics of the NVT were better understood from 2002 until 2006. The visual inspection from an experienced seismologist is convincing because of its accuracy on judgments, flexibility to distinguish the difference between different kinds of signals, or the ability to group same kind of signals, even though differences exist in signals within the same group. Yet, in most regions, using solely visual inspection as the detection method leaves the work laborious and unrealistic for the monitoring of continuous data on multiple stations. Therefore, methods derived to accommodate the large quantity of data, can be designed after good understanding of the signal characteristics of tremor. Conventional methods of NVT detection and location match the original waveforms (Shelly et al., 2007b) or the envelope function of NVT or LFE waveforms on multiple stations (Obara, 2002; Rubinstine et al., 2010). The envelope function is the absolute-valued Hilbert transform of the filtered seismic waveform (commonly 2-12 Hz), which brackets the outline of the filtered waveform. For example, Shelly et al. (2007b) first visually identify sets of LFEs and utilize these particular LFEs as templates to automatically search for matches in the filtered waveforms during other times. This method enhances detection precision, but is limited to detect the repeating NVTs occurring from the same sets of sources. Brown et

al., (2007, 2008) developed an autocorrelation method which searches for the LFEs in continuous data. All these methods rely on the intrinsic quality of data, such as high signal-to-noise ratio and high sample rates. Stacking of multiple records from different stations enhances the energy of individual NVT bursts, but precise picking of NVT arrivals is necessary. The NVT arrivals at different stations form a move-out delay, which is crucial information to properly locate individual NVT. Searching the NVT source grid by grid of the potential hypocentral locations to minimize the error between predicted and observed arrivals, or visually picking arrivals are two ways to obtain the move-out for stacking. Unfortunately, obtaining move-outs in good precision at all times is still quite challenging. Often the signal is well under the noise level to be picked, or the alignment of the arrivals is poor owing to sample mismatch, or that NVT series occurred in such close the time-interval that they overlap each other. Therefore, some NVT might not be detected and reported because of these difficulties. Nevertheless, visual inspection is always necessary to assure the occurrence of NVT, especially when inspecting whether the detection method properly detects tremor signal with a reasonable move-out. Network stations would receive NVT signal with good amplitude if stations were deployed close to the NVT source. In recent years, more stations are deployed specifically for monitoring and detecting NVT in regions where NVT has been previously reported. Advanced seismic equipment enables the mobility of station deployment and the sensitivity of signal recording. As a consequence, more NVTs are detected, albeit with source locations that are not precise yet.

Besides the conventional methods, several studies have applied Beam-Backprojection (BBP) method combined with seismic arrays to observe NVTs in Cascadia (Ghosh et al., 2010; Ghosh et al., 2012) and along the central SAF (Fletcher et al., 2010; Ryberg et al., 2010). This method enhances the detection, and especially the location of NVTs, when there are multiple array clusters surrounding the region where NVT occurs (Ghosh et al., 2012). A station array highly improves the sensitivity of NVT detection. The stacking of multiple records from stations in close proximity emphasizes signal in a fixed range of frequency, and the signal-to-noise ratio is also improved when the records are summed. Such a method makes it possible to study phase details, for example the PcP and PdP phases, which are usually not seen in records of single stations (Rost and Thomas, 2002). Ghosh et al.(2009, 2012) used this method and reported about 5 times more tremor hours (number of detected tremors/ hour) for the time during 1-4 months of the tremor episode.

The Parkfield-Cholame section of SAF provides a good opportunity to investigate the activity of tectonic tremor in great quantity of seismic data. This section of SAF is an ideal region, where high density and frequent NVTs have been well reported (Nadeau and Dolenc, 2005; Shelly et al., 2009; Peng et al., 2009; Thomas et al., 2011).The sensitivity of single mini-array permits the detection of triggered tremors which may have been too weak for conventional methods. We can test how well the BBP method operates and detects NVT in this region. Such details of NVT activities can illustrate the triggering, temporal transition and the strength of source for NVT. Hence, it will provide more information to understand the NVT mechanism. We take advantage of our newly-

deployed mini-array near the SAF and observe NVTs which are not reported in other studies.

3.1.3 Beam-Backprojection Method (BBP)

The BBP method described here refers to the incorporation of both the beamforming and backprojection methods used in array seismology (Rost and Thomas, 2002). The beamforming method is also called array beamforming. The beamforming is generally a signal processing technique used with sensors in an array (or in arrays) for directional signal reception or transmission (Van Veen and Buckley, 1988). This technique collects or transmits the elements of the signals in the array such that signals at particular angles would constructively interfere, while others destructively interfere. Beamforming can be used both in the receiver or the source end of the transmitting signal. It is widely applicable in different fields, like sonar (e.g. Georage et al., 2000), radar (Harjes and Henger, 1973), wireless communication (e.g. Lehne and Pettersen, 1999), radio (e.g. Oyman et al., 2003), and seismology (Berteussen, 1976; Kruger and Weber, 1992; Neal and Pavlis, 1992). In seismology, beamforming detects and estimates the source direction of the signal-of-interest, regardless of earthquakes, tremor, or other seismic signals, in the data received at the seismological arrays (Husebye and Ruud, 1989). It optimally filters, sums the data, and accepts the outputs based on constructive interferences (Rost and Thomas, 2002). The limitation of the beamforming method in seismology lies in that seismic arrays need to be designed and installed to receive the seismic signal of interest. Different seismic signals at different distances and frequency band would require different array configurations. In addition, precise location of the

source of the seismic signal requires several arrays instead of single array. The equipment, maintenance of reception and installation of arrays cost quite some resources. We used the beamforming method specifically in our study because we do not need to precisely locate the detected NVTs in this study. The location of events would require 'back-projecting' the array energy, while detection mainly involves how the 'beam' appears in the slowness domain. The beamforming method illustrates energy from the waveforms by stacking them in slowness space. That is, the vector velocity of a wavefront incident to the array stations is presented in slowness and azimuth. It is worth noting that all phase arrivals are assumed to be plane waves. Any time-window of waveforms coming from a certain event origin sum constructively with the set of slowness and azimuth corresponding to that particular origin, while all other origins yield relatively destructive interference. The slowness map is constructed in 2D space such that there are two axes representing the slowness values in NS and EW directions of the array (e.g. Figure 3.4). The peak amplitude values of the summed waveform data of the array stations according to relative time-shifts are marked in different colors. These time-shifts are determined by the slowness mismatch assuming that the signal incident to all array stations from a source of the particular NS and EW slowness. The resulted amplitude of each summation with identical NS and EW slowness are plotted to the slowness map. On a slowness map, one enclosed colored area would represent the constructive summation of a coherent signal. If there is a set of waveforms from the array stations including one clear event signal, the summation of the waveforms accordingly on the slowness map will produce a clear focus of the peak amplitude, or a focus beam (See example, Figure 3.1).

Note that on the slowness map, the distance from the map center (0,0) to the particular coordinate of NS and EW slowness represents the magnitude of slowness. The azimuth of this slowness vector indicates where the energy should come from. When we do not know whether the set of waveforms contain signal of an event or not, we sum the waveforms according to all possible slowness and azimuth on the slowness map. The azimuth is formed joining the focused beam to the center of the array. The center of all stations in the array is considered as the reference point of receiver, which corresponds to zero time-shift. Waveforms at different stations are converted to the frequency domain and then shifted according to the source-receiver slowness. We search for the event origin by examining the slowness map generated. If there is a clear focused beam on the slowness map, it may point to sources radiating coherent seismic energy. The details on how we discriminate constructive interferences from destructive interferences will be discussed in greater length in 3.2.3.

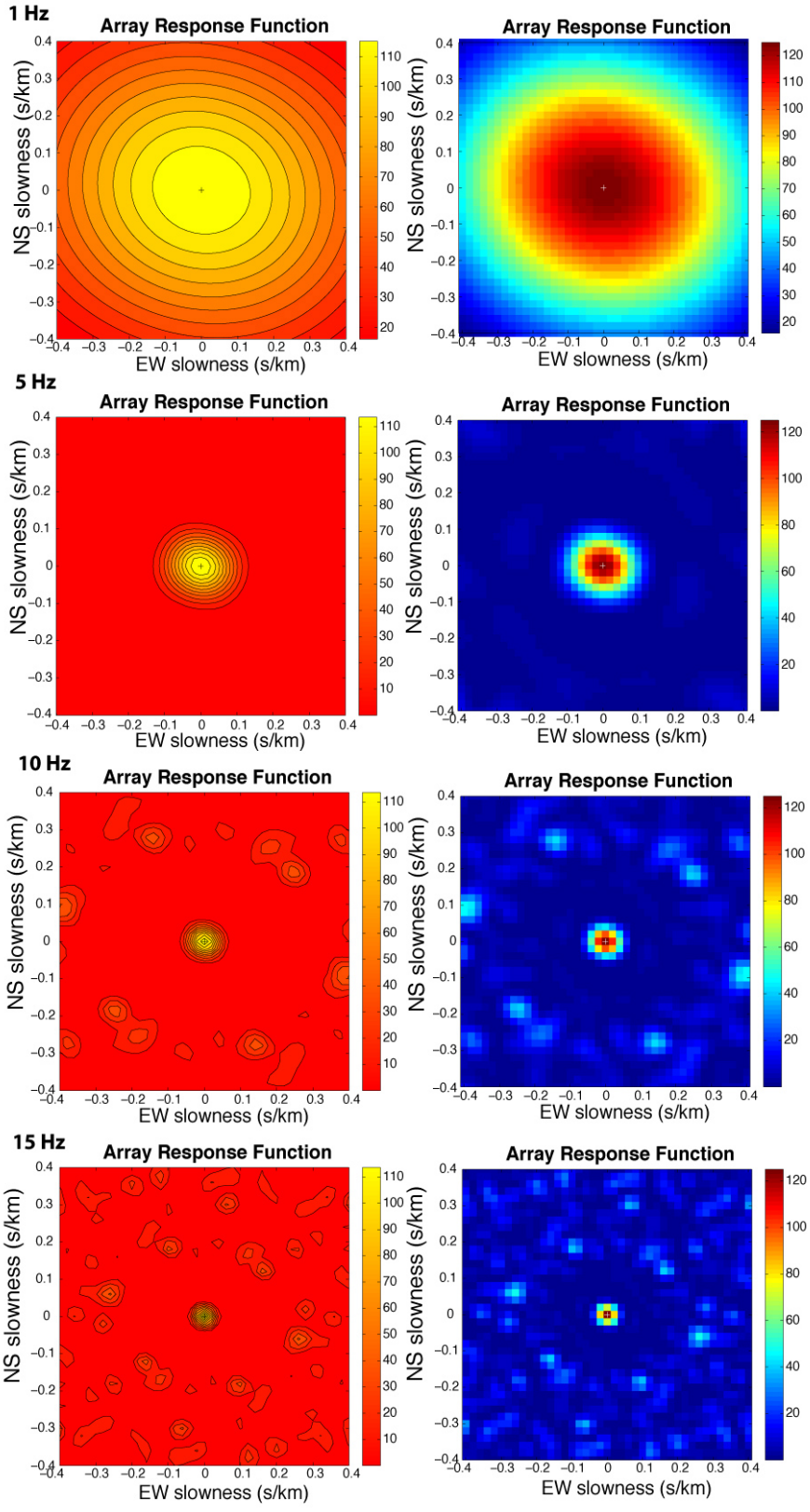
1 Hz
Array Response Function
NS slowness (s/km)
EW slowness (s/km)
Array Response Function
NS slowness (s/km)
EW slowness (s/km)
5 Hz
Array Response Function
NS slowness (s/km)
EW slowness (s/km)
Array Response Function
NS slowness (s/km)
EW slowness (s/km)
10 Hz
Array Response Function
NS slowness (s/km)
EW slowness (s/km)
Array Response Function
NS slowness (s/km)
EW slowness (s/km)
15 Hz
Array Response Function
NS slowness (s/km)
EW slowness (s/km)
Array Response Function
NS slowness (s/km)
EW slowness (s/km)

Figure 3.1 Array Response Function (ARF) of the UCR mini-array.
We show here the response of the array to monochromatic sine waves of period 1, 5, 10 and 15 Hz. These maps assume that signal is coming vertically from any depth (no constraint) at the array center. The focused 'beam' locates at the center of the slowness map. The contoured slowness map (left column) and rainbow-colored slowness map (right column) shows the clear focus at the center and some side-lobs at different frequencies. However, the focused beam is clearly identifiable. The beam is slightly elongated along the fault-parallel direction of SAF, which is specifically designed that all sources along SAF can be imaged.

We validate the correctness of this method by test beamforming both a synthetic signal and some small earthquakes on the SAF. The synthetic signal is a monochromatic sine wave with single frequency, which helps illustrate the resolution and imaging power of our array (Figure 3.1). In the case of beamforming the earthquakes, the focused beam on the slowness map is consistent with predicted slowness values based on the actual origins. The difference between two sets of slowness values can be attributed to the uncertainty in the velocity model, and thus the ray path.

3.5 Data and Methods

3.2.1 UCR mini-array

We utilize data from a mini-array ~8km away from the Parkfield-Cholame section of the SAF (Figure 3.2, right panel). This is a single mini-array consisting of 18 stations, with ~1.5 km aperture and 300 m spacing (Figure 3.2, left panel). The mini-array uses surface broadband sensors and a sample rate of 100 samples per second. The stations were deployed by students and postdocs from UC Riverside since April 10th, 2013, and are still in service as of the writing of this dissertation, October, 2014. The mini-array is designed to image signals from all directions, but the frequency sensitivity is specifically designed for imaging NVT signals (see Figure 3.1). We design the station spacing and aperture of the array so that the Array Response Function (ARF; Rost, 2002) is most sensitive to signal of 2-15 Hz (Fig 3.1). This is the most common frequency range to observe NVT (Gomberg et al., 2008; Peng et al, 2008). When we locate the hypocenters of the NVT events, we use a velocity structure retrieved from the P-wave tomography

result by Thurber et al. (2006) (Figure 3.4). We use a grid search approach, which optimizes the match between event slowness calculated from actual shear wave arrival and the slowness predicted by the source grid. Due to the uncontrollable weather and maintenance, not all the stations in the array provide high quality data at all times. Figure 3.3 shows an example of the variation in data availability for different days during 2013.

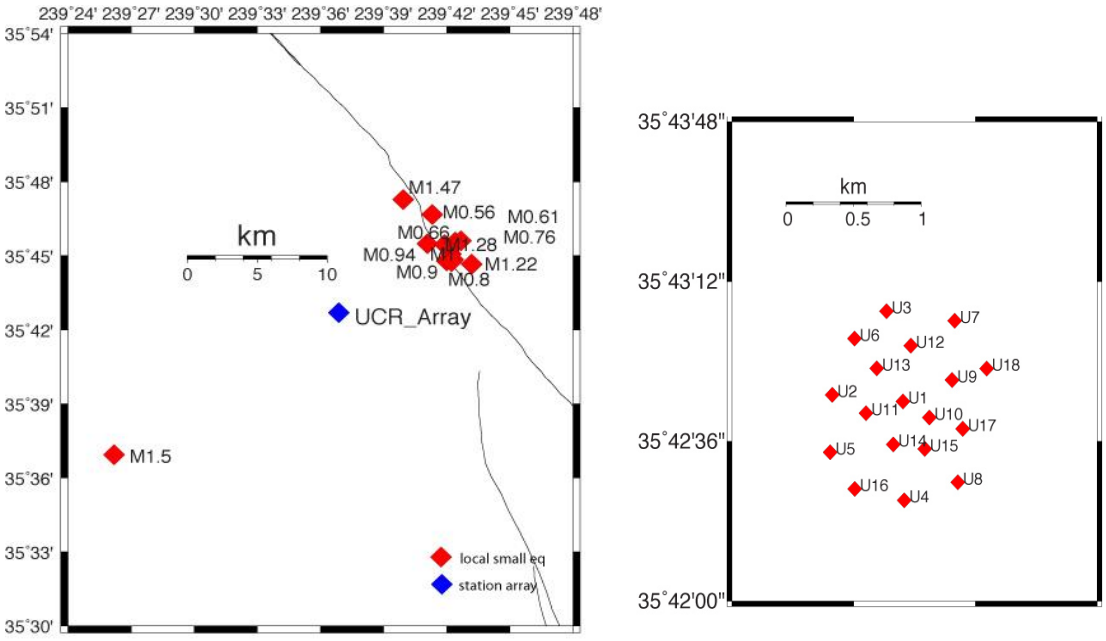

Figure 3.2 The relative location of UCR array to the SAF surface trace and the station distribution in the UCR array.
In the Left panel, the red diamonds show the 13 local earthquakes we used to distinguish the spectrum of tremor from earthquake and background noise. The SAF surface trace spans from the north center (35.9 degrees north) of the map to west of latitude 35.65 degrees. The Right panel shows the station distribution of the UCR array. The red diamonds mark the location of the individual stations. Station name is station number appended with 'U'.

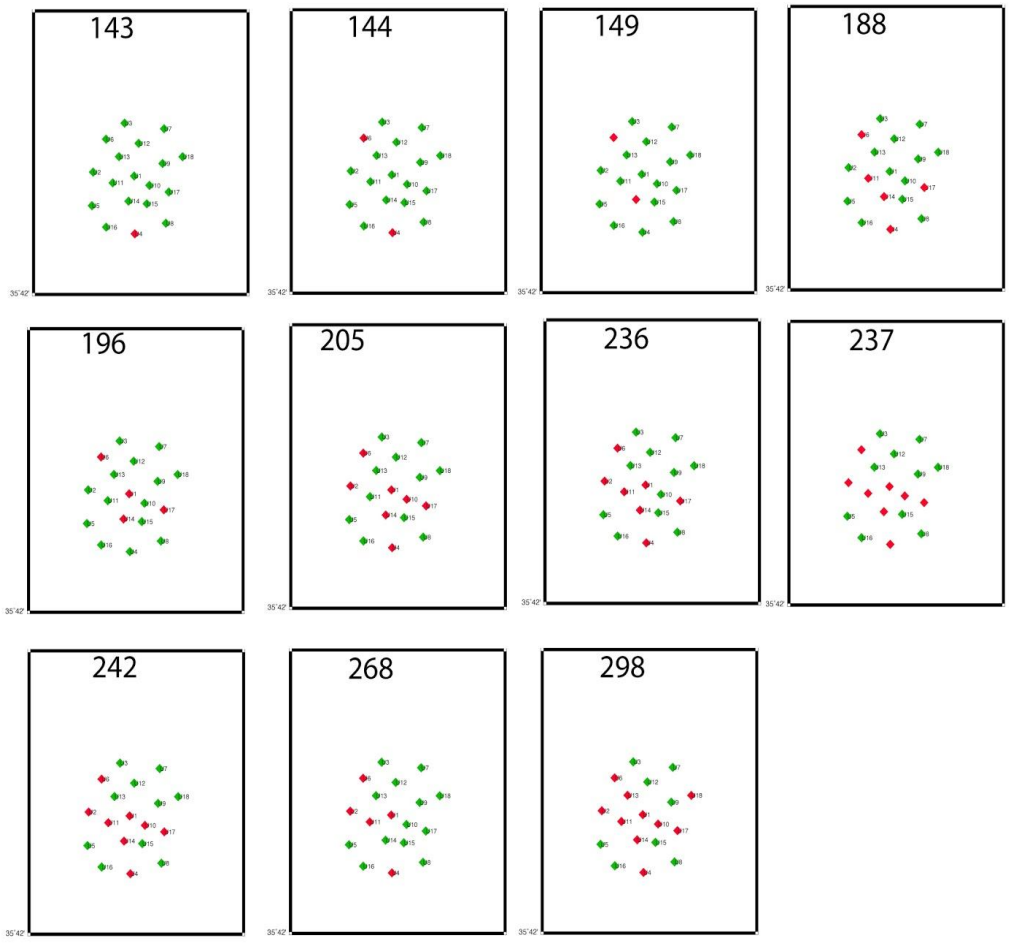

Figure 3.3 The station availability on different days in 2013.
The number at the upper left on each map shows the Julian day, in response to the 11 selected events in our study. The green diamonds show the available and/or stations with good data quality. The red diamonds show stations with either no or low quality data.

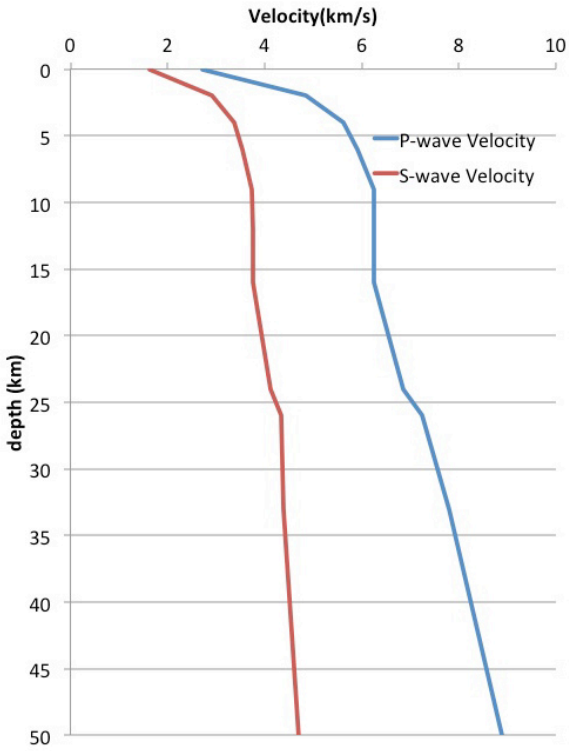

depth (km)	P-wave Velocity(km/s)	S-wave Velocity(km/s)
0	2.7195	1.6317
2	4.8518	2.91108
4	5.6297	3.37782
6	5.9074	3.54444
9	6.2411	3.74466
12	6.2495	3.7497
16	6.2558	3.75348
24	6.8616	4.11696
26	7.2548	4.35288
33	7.8	4.4
50	8.9	4.7

Figure 3.4 The Velocity model modified from the P-wave tomography model by Thurber et al.(2006).
The P-and S-wave velocity values versus depth is given in the table in the right panel. Only P-wave velocity above 26 km is derived from Thurber et al.(2006), which is the most recent dataset available for the velocity model of the Parkfield-Cholame section of the SAF. The P-and S-wave velocity data below 26 km until 50 km is the default setting from TauP toolkit (Crotwell and Owens, 1999). Meanwhile, the S-wave velocity from depth 0 to 26 km is 0.6 times of the P-wave velocity.

3.2.2 Teleseismic Events and Local Earthquakes

We select 11 events occurring from the start of the operation of the mini-array, May, 2013, until end of year 2013. There are 7 teleseismic earthquakes and 4 regional earthquakes (Figure 3.5). The teleseismic earthquakes are selected for magnitude (M_w) over 7.0 and with distance beyond 4500 km (60 degrees great circle arc) from the global CMT catalogue (Lamont-Doherty Earth Observatory, LDEO, of Columbia University). The regional earthquakes are selected for magnitude (M_L) over 4.0 and with distance

ranges from 138-191 km, through the Advance National Science System (ANSS) composite earthquake catalogue (Table 3.1). Some large teleseismic or regional events during the time frame of our investigation were not used because data was either not in good quality or the station was discontinued for service reasons. We include the events that are covered with at least 8 stations in our array. We also confirm that the beam map produced from beamforming still retains fair quality and consistency with the stations available. We estimated the peak shear stress induced by these earthquakes using the peak particle velocity measured from waveforms on the horizontal channels (HHE and HHN), and convert it using the method given in Chapter 2, section 2.3.3. The peak shear stress we estimated ranges from 0.07 to 12.6 kPa. We also compare our estimated shear stress against the stress estimated from the empirical equation by Duncan and Waytt (2014):

$$\log_{10}(\epsilon) = 0.95\ M - 1.65\ \log_{10}(\Delta) - 2.8\ , \qquad (3.1)$$

where the ϵ is the predicted peak strain, the M is magnitude (M_w), $\Delta$is great circle distance in degrees. This equation applies to cases of the peak shear strain for teleseismic, regional and local earthquakes in general. Then, we convert this shear strain to shear stress with a shear modulus of 30GPa. The overall shear stresses are consistent between our estimates from peak ground velocity and the estimates from peak strains (Figure 3.6).

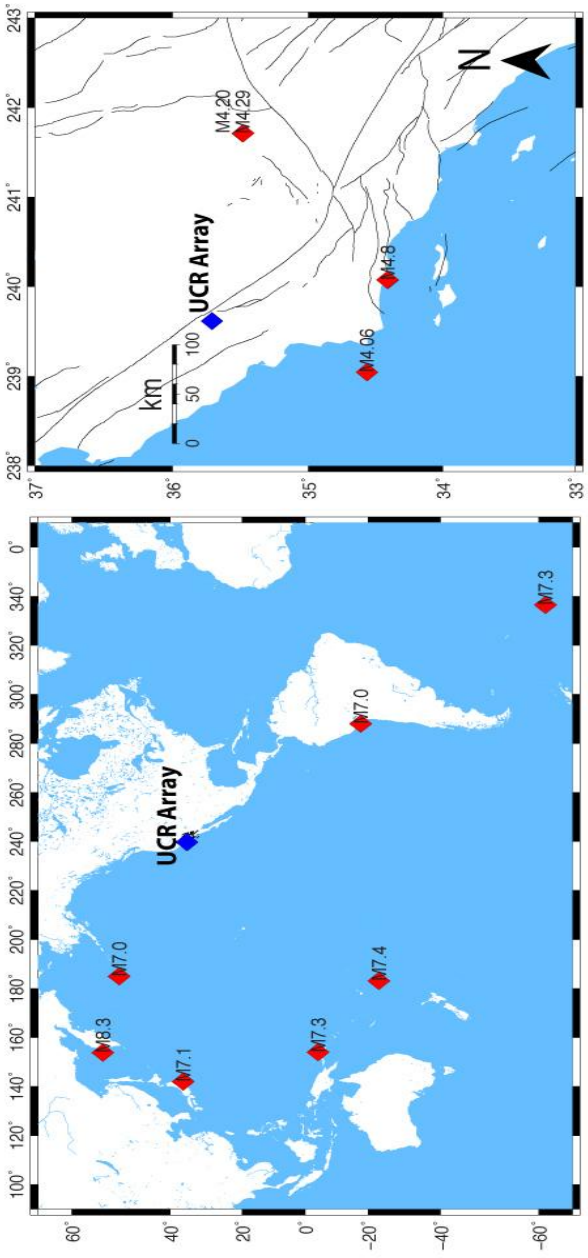

Figure 3.5 The locations of the selected 11 events, including 7 teleseismic earthquakes and 4 regional earthquakes.
The earthquakes are marked with red diamonds and the location of the UCR array is marked with blue spades. The teleseismic earthquake magnitudes are in M_w and the regional earthquake magnitudes are in M_L.

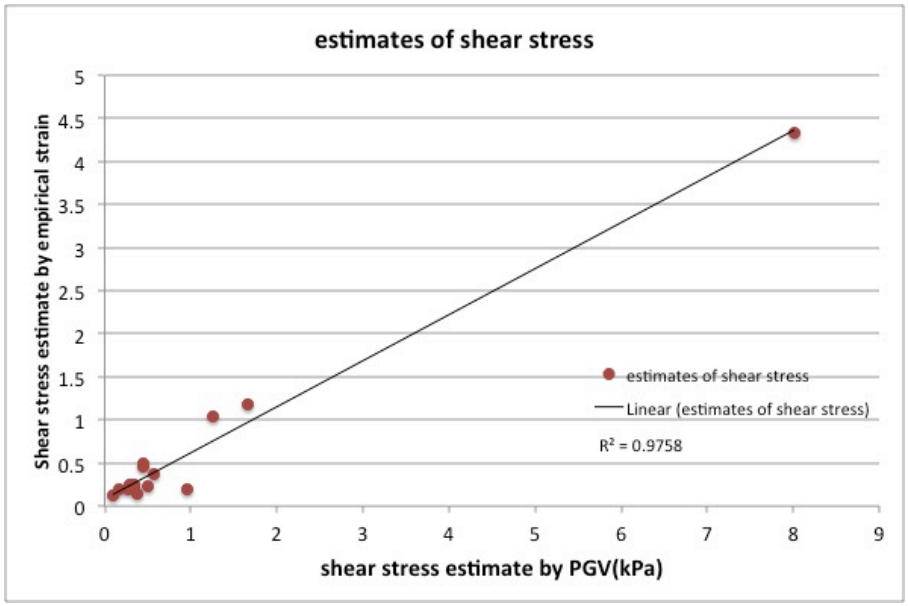

Figure 3.6 The comparison of peak shear stress estimates by two different methods.
The vertical axis corresponds to the converted peak shear stresses estimates by the empirical strain equation (Duncan and Waytt, 2014). The horizontal axis corresponds to the peak shear stress estimated by the PGV. The PGV is measured from the amplitude measured from the averaged waveforms. We find that the estimates are fairly consistent between two methods, that the relation between them is linear with high correlation coefficient.

Teleseismic Events																	
# of Events	Mw	# of Recording Stations	day of year	month	date	time	Depth	(rate) # of NVT bf	(rate) # of NVT during	(rate) # of NVT after	(rate) # of NVT during+after	distance in km	distance in degree	shear stress(kPa)	shear stress estimate by PGV	reported # of tremor by Tremorscope	duration of seismic signal
1	7.4	17	143	5	23	17:19:13	188	(912)38	(1181)41	(2544)106	(1924)147	8841	79.505	0.373	0.5685	5	3000
2	8.3	17	144	5	24	5:43:08	611	(600)25	(1961)59	(2856)119	(2481)178	6598	59.341	4.326	8.0093	2	2600
3	7.3	17	188	7	7	18:35:42	383	(696)29	(648)21	(2016)84	(1417)50	9881	88.859	0.249	0.3431	0	2800
4	7.3	17	196	7	15	14:04:07	21.5	(600)25	(1123)26	(1968)82	(1666)108	13778	123.9	0.144	0.3772	0	2000
5	7	15	242	8	30	16:25:09	26.7	(408)17	(372)28	(1944)81	(941)109	4618	41.526	0.454	0.4423	0	6500
6	7	13	268	9	25	16:42:52	46.1	(384)16	(451)20	(1968)82	(1186)102	7489	67.352	0.204	0.2758	0	3828
7	7.1	13	298	10	25	17:10:25	24.9	(1152)48	(280)12	(2088)87	(816)69	8088	72.736	0.224	0.3414	0	3700
Regional Events																	
8	4.8	16	149	5	29	14:38:03	7.95	(744)31	(2095)8	(1920)80	(1934)88	150.38	1.3524	1.049	1.2554	0	330
9	4.3	17	205	7	24	16:46:03	6.6	(984)41	(3702)9	(1584)66	(1701)75	191.32	1.7206	0.231	0.5073	0	210
10	4.1	15	236	8	24	1:16:31	3.17	(336)14	(0)0	(1128)47	(1074)47	137.5	1.2366	0.241	0.2954	0	180
11	4.2	15	237	8	25	18:50:29	2.30	(552)23	(1098)7	(648)27	(750)34	191.61	1.7232	0.189	0.9658	0	320

Table 3. 1 The 7 teleseismic and 4 regional events used in the investigation for triggering of NVT.

The location of the events are also plotted in Figure 4.4. The detected NVTs before, during and after these events are also given in the this table. The converted rate of NVT (per day) before, during and after these events are shown in red and parentheses. The rates are converted for the consistency that they can be compared. The time of earthquake durations are visually inspected by procedure described in this section and shown in figure 3.7, given in the last column.

We select 1 hour of data before the arrival of each event to determine the background rate of NVT. We select the time after the first arrival of the events, which includes the transient termination of the passage of the seismic waves radiated by the event in question, and 1-hour data after the event in question (Figure 3.7). We determine the termination of the passage of the seismic waves radiated by the event as the time at which the averaged waveform amplitude in 5-second window becomes equal or less than 10% of the peak amplitude of the event (Figure 3.7). The rate of NVT is calculated among these three phases of time: before, during and after the major events. We consider the rate as the number of NVT occurred divided by the period of time, then the rate is converted to number with identical unit (per day). It is worth noting that the period of time used in our calculation for rate of NVT during the major events varies (Table 3.1, last column), while for the rates of NVT before and after the major events, the period of time is always 1-hour. We also calculate rate of NVT for the time during and after 1-hour of the 11 events for comparison purpose. The time that includes during and after the 11 selected events is defined as the 'all-after' period. When we illustrate whether there is an increase of the rate of NVT, we calculate a ratio dividing the rate of NVT in a period of time by the rate of NVT before the potential triggering events. We calculate the ratio using the rate of NVT in units of per day.

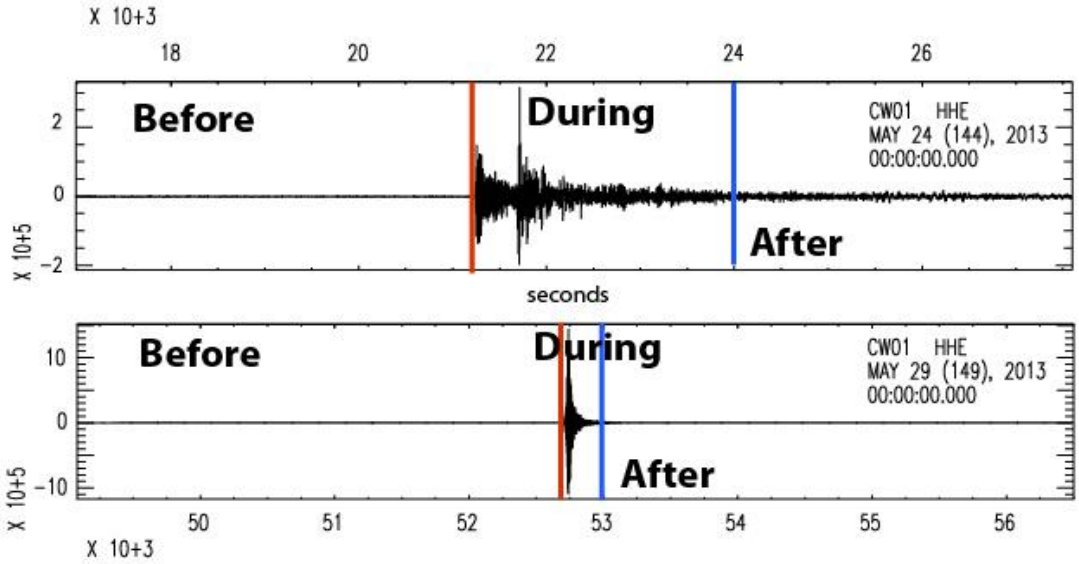

Figure 3.7 Waveform plots showing examples of how the time windows of before, during and after the 11 major events have been divided.
The upper panel shows an example for teleseismic event occurring on May, 24th, 2013, which lasted ~2700 seconds. The lower panel shows an example of regional earthquake on May 29th, 2013, which lasted ~330 seconds. The red vertical lines mark the first arrival of the two events, and the blue lines mark the termination of the events (definition in chapter 4.2.2)

We compare the spectrum among tremor, noise, and local earthquakes in order to validate that the potential signals we detected are tremor. We select 13 local earthquakes from ANSS catalogue since July 2013 until end of year 2013 (Table 3.2). These local earthquakes are primarily located on the SAF (Figure 3.2, right panel) and the magnitudes are from 0.6-1.5 (M_L). We chose these local earthquakes with small magnitudes to match the level of ground motion (derived from velocity record) to the tremor signal.

year	month	day	hour	min	seconds	lat	long	depth	magnitude (M_L)	yday
2013	7	4	7	0	0.68	35.758	-120.315	11.59	0.94	185
2013	7	22	9	41	17.19	35.758	-120.302	5.96	1.28	203
2013	7	26	1	14	40.59	35.751	-120.297	6.83	0.66	207
2013	7	28	6	5	8.97	35.747	-120.3	11.75	1	209
2013	7	28	6	6	22.23	35.748	-120.295	12.46	0.9	209
2013	8	16	21	24	42.94	35.788	-120.334	8.65	1.47	228
2013	8	26	6	7	2.9	35.778	-120.312	8.23	0.56	238
2013	10	9	9	25	32.82	35.616	-120.564	4.99	1.5	282
2013	10	14	10	43	48.04	35.745	-120.28	5.51	1.22	287
2013	10	20	3	31	57.26	35.759	-120.293	9.95	0.61	293
2013	11	19	11	53	22.64	35.746	-120.296	7.59	0.8	323
2013	12	7	3	52	3.6	35.76	-120.289	12.54	0.76	341

Table 3.2 The local earthquakes used in constructing the spectrum of earthquakes on the SAF. The surface locations of these earthquakes are also plotted in Figure 3.2.

3.2.3 Beamforming Detection

During the selected time window around each of the 11 events, We use the beamforming method described in section 3.1.3 to scan through the ~2 hours of data. Each time window is 30 seconds long, but the beamformed maps are calculated in 5-seconds shift. The 5-seconds shift guarantees that the back-projecting detection of NVT captures every possible LFE (likely 6-10 seconds; see Figure 3.7, ~from 12.5-21 s) combined in the NVT. The LFE event is usually shorter duration (6-10 seconds, e.g. Shelly, 2006) compared to the NVT episodes commonly described and detected in other studies (minutes to days, e.g. Wech and Creager, 2008; Rogers and Dragert, 2003). We build a screening process where the slowness maps are all formed, but only the potential maps with clear focuses are saved for further verification. The screening process automatically searches for distinct focuses of beam during each window. We impose a screening in which the peak amplitude of slowness is recorded, as well as those that are 90% of the amplitude of the peak. Then, the screening process selects those slowness

maps which include less than or equal to 3 focuses of beam. This eliminates the slowness maps that do not show significant focuses of beam. The slowness maps that are saved after the screening process generally suggest that there are NVTs within the specific time window (e.g. Figure 3.8, bottom panel). We limit the slowness of the signal between ± 0.4 in north-south and east-west directions (see Figure 3.8). This limitation confines the signal from those that are shallow, which mostly is noise from the surface. However, this limitation also exclude possible tremor signal from shallow depth ($\leq$ 2 km).

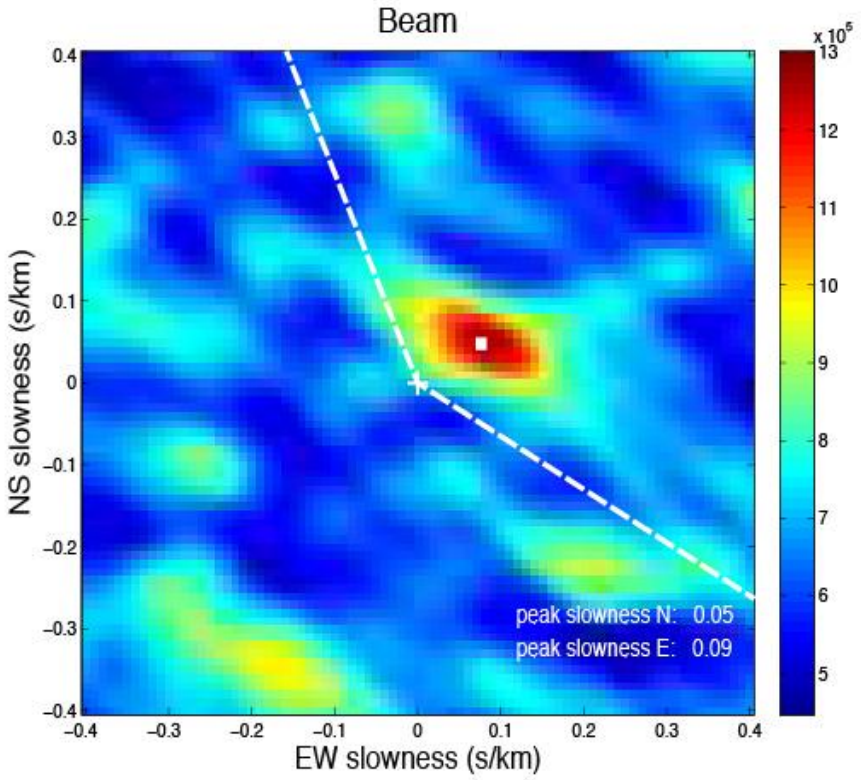
Beam
x 10^5
13
12
11
10
9
8
7
6
5
0.4
0.3
0.2
0.1
0
−0.1
−0.2
−0.3
−0.4
NS slowness (s/km)
peak slowness N: 0.05
peak slowness E: 0.09
−0.4 −0.3 −0.2 −0.1 0 0.1 0.2 0.3 0.4
EW slowness (s/km)

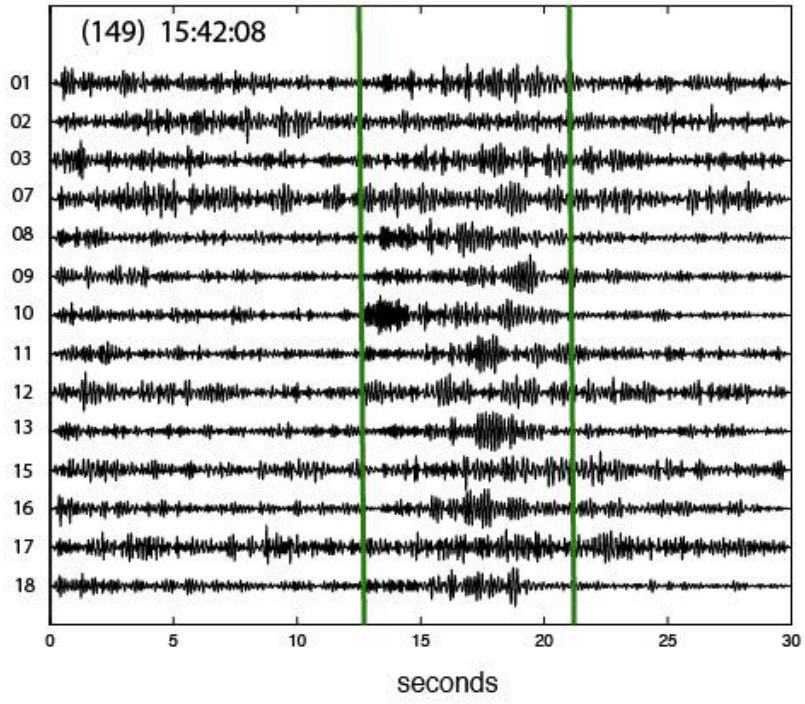
(149) 15:42:08
01
02
03
07
08
09
10
11
12
13
15
16
17
18
0 5 10 15 20 25 30
seconds

Figure 3.8 An example beam map and the waveforms from each station with the corresponding time window.

This example shows a detected tremor occurred on day May 29th, 2013, during a regional earthquake. The upper panel is the slowness map (or beam map). The center of the slowness map falls on the white cross. The small white square shows the peak amplitude of the focused beam, which corresponds to slowness 0.05 North and 0.09 E. The focused beam is determined by the enclosed, peak amplitude on the slowness map. This beam falls within the range of azimuths which limits the wave energy coming from the tremor source on the SAF. The white dash lines show the range of slownesses within azimuth -20~120 degrees. The closer is the slowness coordinate set to the center, the deeper the event energy comes from. The lower panel illustrates the detected 'tremor' bursts, which also equals to single LFE, on individual stations. Note that on the vertical axis the station number is marked as axis labels. There are 14 station data available for this particular day and time. The date and start time for this particular time window is marked at the upper left corner. The tremor burst is apparent on all station data during 12.5-21 seconds in the time window, which is bounded by the vertical green lines.

Among the slowness maps saved from the screening process, I visually inspect the slowness maps for confirmation of focused beams. In this process, I also inspect the source azimuth of the slowness maps to confirm that the beam locates within azimuth -20 to 120 degrees (Figure 3.8, top panel). This is the possible range of azimuths that indicates the source is coming from SAF. I visually inspect the waveform in each time window corresponding to the selected slowness maps. Through these visual inspections, we report only the ones with clear impulsive signals. The clear impulsive signal is defined as the enclosed focused beam of peak amplitudes with values at or above 10^5 times the averaged amplitude of the slowness map. This threshold value is empirically tested for beamforming NVT using data of the UCR array and in this region. Our final detection numbers of NVT is based on those time windows passed through final stage of inspection (e.g. Figure 3.8).

3.2.4 Spectrum of Detected Tremor

We further confirm detection of tremor by plotting the spectra of detected tremor against those of the noise and local earthquakes. We randomly select 13 time windows from the final detected NVTs using BBP and plot the averaged spectrum. In this comparison figure, we plot the spectra averaged from the 13 local earthquakes described in section 3.2.3. For the background noise, we use 30-second time windows before each 13 local earthquakes and averaged the spectra (Figure 3.9). The earthquakes selected are chosen to be of low magnitudes that match the amplitudes of tremor as close as possible. However, the earthquakes selected still have high magnitudes in average compared to tremor, that the spectra averaged from earthquakes have higher amplitudes than that of

tremor above 2 Hz (Figure 3.9). All spectra are calculated with waveform records that are not filtered.

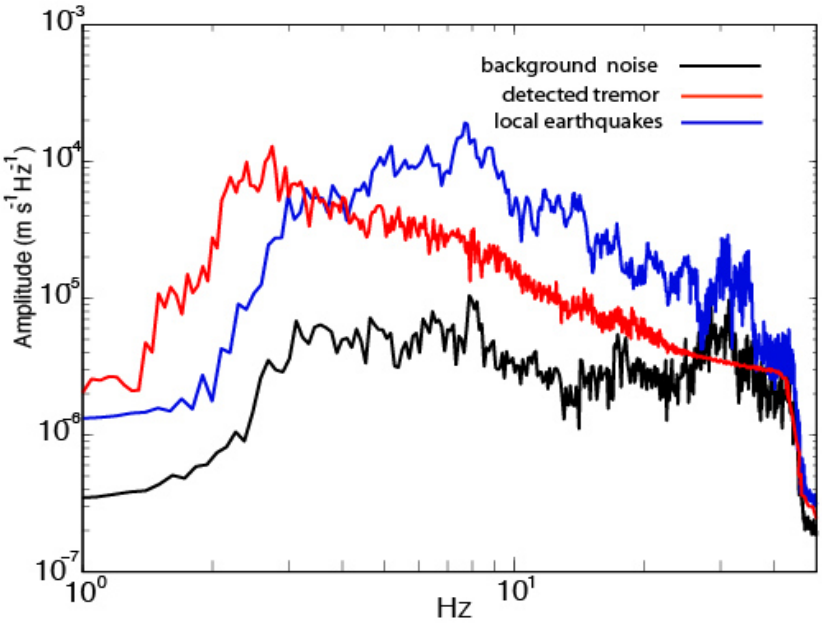

Figure 3.9 The average spectrum of the background noise, tremor, and local earthquakes. The spectrum in this figure is formed using record of station 03 only. The station 03 is selected purely for demonstration reason. We have confirmed that other station records performed consistently. The background noise and local earthquake spectra are averaged from the 12 selected earthquakes in Table 3.2. The background noise portion is 10 seconds time window picked before the first arrival the local earthquakes. The spectrum of the detected tremor is averaged from 12 randomly selected time windows, which are detected and visually confirmed as tremor.

3.5 Results

3.3.1 Detections

It is important to know a background rate of tremor as a reference, so that we can determine whether triggering of tremor occurs during or after the large stressing events. To obtain the background rate, we use 11 hours of data, consisting of each 1 hour before the selected large events. We also include 10 randomly selected 1-hour time windows of

the data from UCR array in 2013. All waveforms are visually inspected to eliminate the chance of including any local or regional earthquakes. Then, we detect the number of NVT in each of the 21 hours of data. It is worth noting that the NVT reported here is equivalent to LFE burst since the visual inspection limits the signal length (6-10 seconds) on the waveform. We obtain the number of NVT occurred during the passage of the 11 events (See section 3.2.2 for definition). However, the duration of the 11 events vary because teleseismic events are mostly long (~2000 s) and the regional earthquakes are short (~200 s). The rate of tremor reported in Table 3.1 is converted to the unit of 1/day in order to keep the consistency among the rate of before, during and after the selected events (Figure 3.8). We find most detections of NVT have sources from the SAF using the beamforming method, while less than 10% of the detections suggest sources of NVT not on the SAF. The detections suggested by beamforming method but later on rejected by manual inspection is ~ 13% of the total number of detections.

3.3.2 Background Rate of Tremor

To determine the background rate of tremor robustly, we randomly select 10 other 1 hour time period and gain detection numbers of NVTs. We use the 11 selected events of independent earthquakes that the 11 hours before these events can be used in the statistics. We assume this average will best replicate a random process, and the population of the tremor rate without any disturbance should be normal distributed. We calculate the mean of the rate of the tremor from 1 hour before the major events and 10 other randomly selected hours. The mean and the standard deviation value derived from

these 21 events should help us clarify the detection consistency and variation using beamforming. The standard deviation value represents the variability of the background tremor rate. We find that the background rate of tremor is averaged ~28/hr, or 672/day. The standard deviation is 11/hr, or 264/day (Table 3.1).

3.3.3 Induced Rate of Tremor

We do not see a consistent increase of tremor rate during the passage of the seismic wave of the selected 11 events, especially for the event of teleseismic earthquakes (Figure 3.10 (B)). We find that during the 1-hour after termination of the passage of the seismic waves radiated by the 11 events, the rate of tremor is 69/hr, or 1656/day. We find that both the tremor rate after, and when we include the tremor rate during and after the 11 selected events, had the rate increases noticeably in comparison with the rate before the major events. The rate of NVT increases by 2 times or above in 7 out of 11 events if the rate of NVT after the termination of the earthquake events is considered (Figure 3.10 (A) and (C)). The overall rate of tremor after the first arrival of the 11 events yields an average of 69/hr, or 1656/day (from Table 3.1). The average rate of tremor increases by ~2.4 times higher after the seismic wave of the events has passed through. For the time during the termination of the event waveform, 7 out of 11 tremor rates increase but not significantly. The teleseismic earthquakes seem induce greater increase of tremor rate relative to the regional earthquakes (Figure 3.10, event number 1-7). The standard error of the mean rate before these events is 261/day, and the standard error of the mean rate all-after these events is 599/day. The increase in the mean rate is from 669/hr to 1338/hr with the uncertainty lies in between 739/hr and 1937/hr. This

suggests that mean rate of tremor after the first arrival of the 11 events is significantly higher even including the uncertainty of the mean values. While all 11 events show an increase of tremor rate after the arrival of the waveform, we arbitrarily determine that the events showing increase of tremor rate of 2 times or more are considered successful triggering of NVT. We determine the ratio 2 in comparison to the beta-value in statistical seismology (Matthews and Reasenberg, 1988; Reasenberg and Simpson, 1992). The value of beta will be large and positive in regions where seismicity increases (Hough, 2005). A minimum ratio of 2 suggests a beta-statistic value of 8.44, while a beta-statistic over 3 is considerably high in terms of seismicity increase of earthquakes. The background rate of events and standard deviation used in calculating beta refers to the mean background rate of NVT, 28/hr and standard error of the mean, 11/hr. In this case, 7 out of the 11 events had shown significant triggering of the NVT. We plot the corresponding peak shear stress of each event and mark the triggering events as green bars. Higher peak shear stress does not necessary trigger more NVTs (Figure 3.11). We observe the triggering of NVT with respect to the induced peak shear stresses (Figure 3.12). The distance of the triggering event does not seem to affect the triggering of NVT. However, peak shear stress above 0.25 kPa usually triggers NVTs (Figure 3.11, purple line, and Figure 3.12, red dashed line).

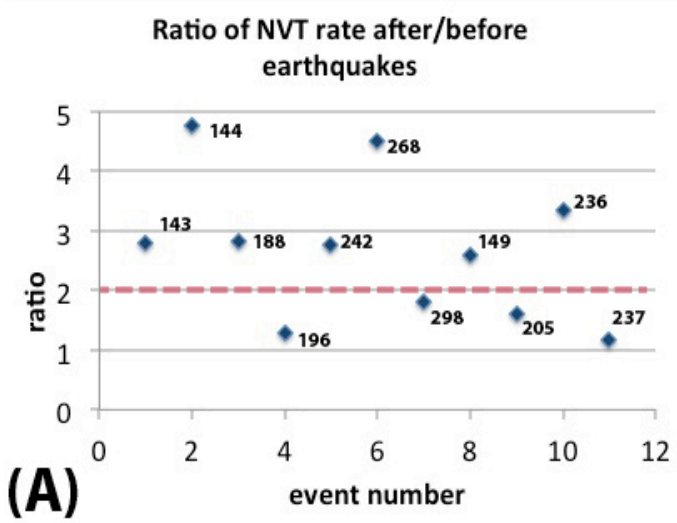
Ratio of NVT rate after/before earthquakes
ratio
event number
144
268
143
188
242
149
236
298
205
237
196
0
1
2
3
4
5
0
2
4
6
8
10
12

(A)

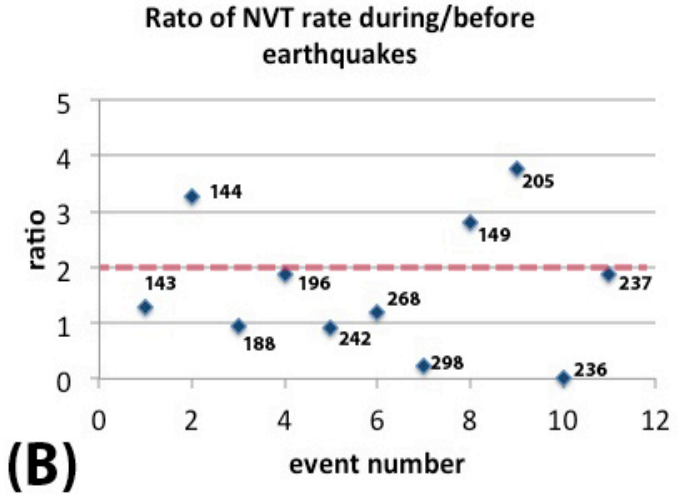
Rato of NVT rate during/before earthquakes
ratio
event number
144
205
149
143
196
237
268
188
242
298
236
0
1
2
3
4
5
0
2
4
6
8
10
12

(B)

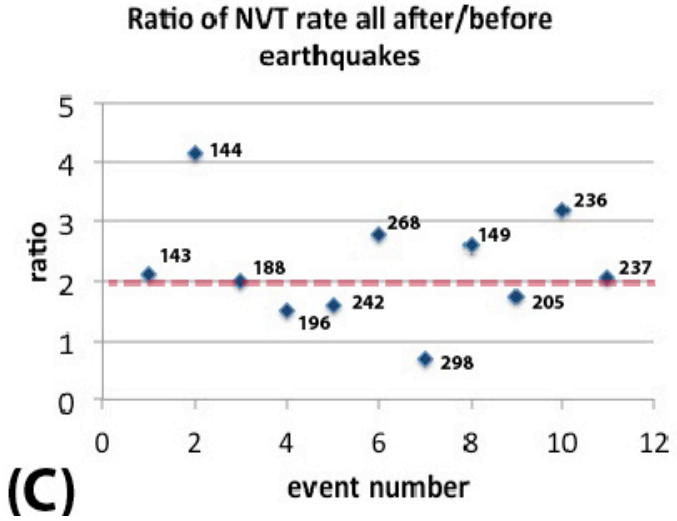
Ratio of NVT rate all after/before earthquakes
ratio
event number
144
236
268
149
143
188
237
205
242
196
298
0
1
2
3
4
5
0
2
4
6
8
10
12

(C)

Figure 3.10 Ratio of the rate of detected tremor after, during and all-after to the rate of NVT before the 11 major events.
The rate is converted to number of tremor per day, in order to be consistent and comparable among the three different time-durations. In all three plots, the blue diamonds show the ratio calculated as described in section 3.2.2, for the change of the rate of NVT after (panel A), during (panel B), or all-after (panel C) the potential triggering events. The red dashed lines mark the ratio value 2 as a minimum threshold, above which triggering of NVT occurred in this study.

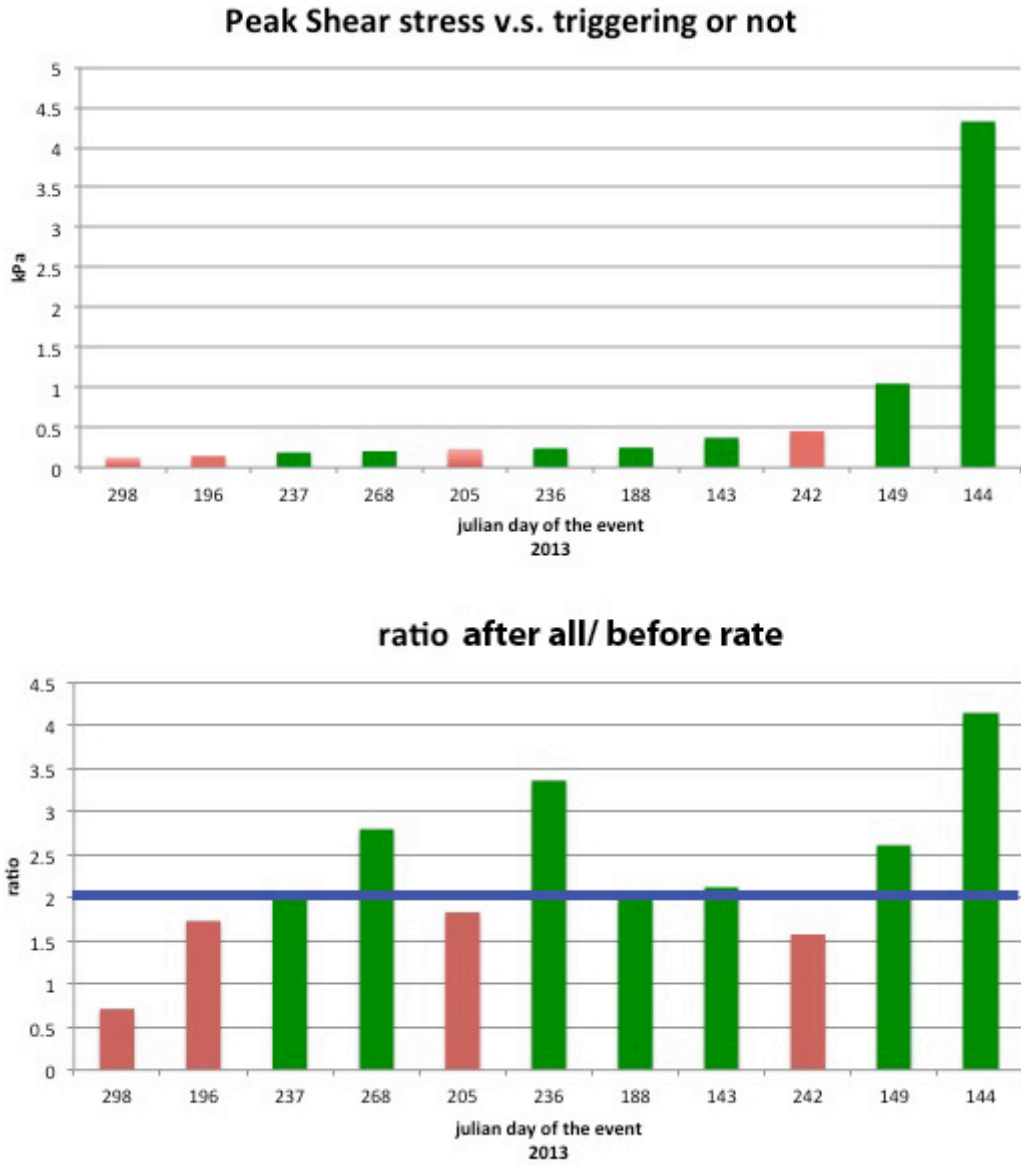

Figure 3.11 The peak shear stress induced by the 11 earthquakes, and the triggered NVT number with respect to the background rate of NVT.
The lower panel shows the ratio calculated based on the rate of NVT 1-hour before and after the first arrivals of all triggering events. The green colored bar corresponds to the events with ratio over 2 (purple line). The ratio 2 is an arbitrarily set threshold to distinguish triggering of NVT occurs or not. The upper panel shows the peak shear stresses of each event. All the events are dated by Julian day of 2013.

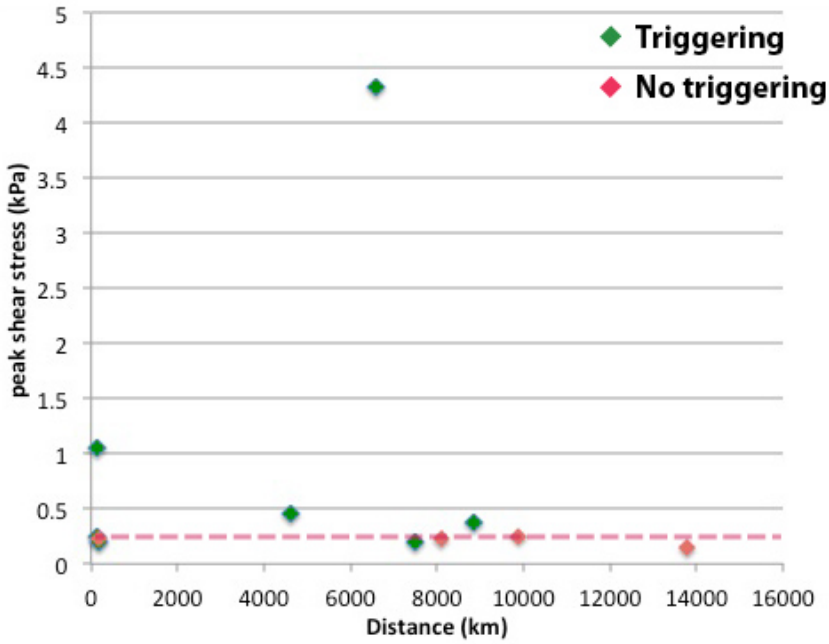

Figure 3. 12 The triggering of NVT with respect to the peak shear stress induced in the 11 events.
The green diamonds show the events with increase of the rate of NVT at or above ratio 2. The red diamonds show the events with no significant increase of the rate of NVT. The peak shear stress induced at the surface by each event is indicated on the vertical axis. Meanwhile, the horizontal axis indicates the great-circle distance between the source of the earthquakes and the center of the UCR array. The red dash line marks the minimum triggering threshold of peak shear stress, which is suggested by the triggering and non-triggering events.

3.5 Discussions

3.4.1 Enhanced Tremor Detection

Nadeau and Dolenc (2005) reported increase of tremor observations after the 2003 San Simeon Earthquake, while they state that the general background rate of tremor is detected as less than 5/day using the same detection method. They use the envelope function detection developed by Obara (2002) to look for tremor. They reported 110 triggered tremor detections with duration lasting 4-20 minutes in 0.2 years time. Nadeau

and the Seismologist from Berkeley Seismological Laboratory (BSL) later developed continuous monitoring project of the NVT near the Parkfield-Cholame section of the SAF. This project is called TremorScope and there is rapid update of data. The TremorScope catalogue reports 95 NVTs during the period of time we select the 11 earthquakes (May, 2013- December, 2013). During the days of our selected events, the maximum number of detected NVT is 5. The reported NVT may have different definitions of the duration of single detection between different detection methods. The detection method used in TremorScope and later published by Nadeau and Guilhem (2009) was automatically scanning root-mean-squared envelope function with an empirically defined threshold. Then, a visual inspection was carried out to exclude non-NVT signals. They use surface stations of SCSN and the HRSN, 8 borehole stations for better sensitivity to detect NVTs. The total number of detection reported by TremorScope during the same period of time are only 7 incidences, which fall on the Julian day of 143 and 144 (Event number 1 and 2 in Table 3.1). The detected rate of NVT by TremorScope is much lower than the background tremor rate we reported. TremorScope reported no detections while there is always a background rate of NVT detected by the beamforming method. In the work of Nadeau and Guilhem (2009), they report in total 2198 NVTs in 91 months. The NVT reported by them uses a 3 minutes window and 0.5 seconds step for detection. we suppose that all the windows contains at least 1 LFE or more. Converted to the 10-second window we used, the detection number of NVT yields a rate of NVT > ~15/day. This rate of NVT is still lower than our averaged background rate for an order or more. Shelly et al.(2009) examined one active day of tremor near Cholame using the

borehole HRSN data. They used the cross-correlation method to detect tremor, which they determine individual LFE bursts on the waveform, and they form the template for these tremors. They reported 149 correlated events during the day. With careful inspection and correlation to check the repeating nature of these NVTs, the rate they report is still ~6 times lower than the background average we obtained.

Horstmann et al.(2014) build an semi-automatic detection method for NVTs in large datasets. They utilize a combination of the envelope cross-correlation and the Self-Organize-Map (SOM) algorithm. They detect tremor using the semi-automatic method with 13 surface stations deployed close to the Parkfield-Cholame section of SAF. The detection made by their method during the 13 months station operation, reports 2606 NVTs in accumulation of 55 hrs. They test the accuracy of the method with visual inspection and report a 80% accuracy. This tremor rate converts to an average ~6.7/day, which is still lower than the average tremor rate we obtain.

The imaging strength supported by the specific designed array and beamforming method benefits the superior enhancement of tremor number detected in our study. The stacking at finer resolution in slowness also supports the imaging power of the beamforming method. The background tremor rate we found with a small pool of data is 50% more or above all tremor rate currently known at this region. We validate our tectonic tremor detection visually. We also distinguish the NVT spectrum from the spectrum of background noise and local earthquakes (Fig 3.9). We find that the beamforming method can serve as a robust screening process at the first step. In Ghosh et al.(2009, 2012), higher number of NVT detection is evident. The beamforming method

might be capable of detecting NVTs that are well below the noise level. Thus, the signal quality can be compromised, as long as there is more than enough stations data in this case.

3.4.2 The Threshold of Triggering Shear Stress for Tremor

We find that the triggering of NVT is apparent that 7 out of 11 teleseismic and regional earthquakes have triggered more NVTs, if the increase in rate of NVT above 2 is considered as a threshold. The minimum shear stress required for triggering is likely as low as 0.25 kPa. This minimum threshold is reduced from what previously reported, ~22.5 kPa, from the observation of 42 large teleseismic earthquakes (Chao and Peng, 2013). However, Gulihem et al. (2010) reported a smaller minimum threshold, ~1 kPa, based on observing 99 regional earthquakes (M5+). This result suggests that the threshold for NVT triggering at this region should be revised when the data is examined more thoroughly, or using other NVT detection methods. A smaller minimum threshold implies that the Parkfield-Cholame section of SAF is more susceptive to triggering than what we previously learnt. This section of SAF seems more susceptive to triggering than most other fault zone as well (e.g. minimum shear stress threshold in comparison to Anza along SJF; 17-35 kPa, Chapter 2, subduction zone at Japan; ~10kPa, Chao et al., 2013, or subduction zone at Sumbawa, Indonesia; ~8 kPa, Fuchs et al., 2014). There are several potential reasons why triggering of NVT is so prominent in this region. One is that this section of fault is preloaded to fairly close to failure, so that small amount of shear stress change can easily trigger NVT. Another reason is that the fault is intrinsically weak, provided the low friction coefficient caused by fault gouge, or low effective normal stress

caused by pore-fluids. Or, the fault gouge and pore-fluid are both present. This study does not help distinguish what causes the small shear stress threshold. However, our result affirms that triggering of NVT at this section is, that NVT would be triggered at a low minimum shear stress.

3.5 Conclusions

We examined the triggering of NVT by 7 teleseismic earthquakes and 4 regional earthquakes along the SAF, using the BBP method and the data from the UCR array. We find 7 out of 11 earthquakes had increased the rate of tremor significantly by 2 times or above. We consider that these events had triggered NVT along the SAF. The corresponding peak shear stress from these triggering earthquakes are mostly above 0.25 kPa. Our results suggests that the minimum shear stress required to trigger NVT in this region is reduced from the number previously reported by others (Gulihem et al.,2010; Chao and Peng, 2013). This reduction of the minimum shear stress implies that the Parkfield-Cholame section of SAF is very susceptive to triggering of NVT. It may further support the idea that this section of the SAF is quite weak, or the stress condition on the fault is on the brink of failure.

Chapter 4 Remote Triggering of Fault Zone Instability: A Numerical Simulation Using rate-and-state Friction

4.1 Introduction

The precise stress conditions for the triggering of tectonic tremor are not well understood. Numerous observations of triggered tremor have provided important insight to the understanding of triggering process (e.g. Rubinstien, 2007; Guilhem et al.,2010; Chao et al., 2013; Yang and Peng, 2013). These observations include reports on the threshold of the peak of the transient stress change, which can vary considerably from location to location. The different background tectonics, frictional properties of the host rock, and the stressing history on the fault cause these variations. Direct observations of the triggered events serve as one crucial way to understand this process empirically. However, what observations provide us are sporadic evidence, which is limited when we need to see a complete picture of the physics behind the triggering process. Therefore, numerical simulation is a way to systematically test the possible factors involved in the triggering process of NVT.

4.1.1 Triggering of Fault-Zone Instability

The physical mechanism of the instability of slip on a fault, which includes earthquake, SSE, LFE, and NVT, has been an issue of much debate in seismology. Through careful monitoring of the occurrence rate of these instabilities, possible changes of the temporal rate of these slip instabilities can be identified during some period or at some time. The temporal rate of events is referred to as ‘seismic rate’ in this study. The

change can be attributed to individual events that induce stress perturbations. Some phenomenon that can perturb the seismic rate include the passage of teleseismic surface waves, regional large or medium earthquakes, or tidal loading (Hill et al., 1993; Kilb et al., 2000; Tsuruoka et al., 1995). These events are said to 'remotely' and 'dynamically trigger' the slip instabilities. Observations of the triggering help us better confine what are the crucial factors involved in this transient process. In general, current scientific consensus suggests that the stress (and thus strain) at the location of triggered earthquake or tremor, has been increased by loading (Duncan and Wyatt, 2014) to some sort of threshold that instigates slip.

Gomberg and Johnson (2005) and Johnson and Jia (2005) extensively studied the dynamics of earthquake triggering. These studies primarily focused on estimating seismic response from the source on the fault implied by the field-based earthquake aftershocks and laboratory experiments based on rock physics. They modeled the triggering of earthquakes in the laboratory with gouge between the frictional surfaces resembling the fault plane. Gomberg and Johnson (2005) found that seismic waves cause further earthquakes at any distance if their amplitude exceeds several micro-strain, regardless of their frequency content. They finally concluded that remote triggering of earthquakes may require large dynamic deformations ($\geq 3\frac{cm}{s}$ PGV; ~23 kPa), perhaps as a result of strong directivity, thereby explaining why this process rarely occurs. The San Andreas Fault Observatory at Depth (SAFOD; 2010), a scientific borehole located northwest of Parkfield, California, near the southern end of the creeping zone of the SAF, investigated fault material at 2.7 km depth. The SAFOD core was analyzed and smectite clay mineral

was discovered as a thin (1.6-2.6 m), highly foliated gouge layer (Lockner et al., 2010) on the fault. In laboratory tests, the fault gouge presented a friction coefficient that is quite low (0.15-0.25), which supports the idea of weak strength on the SAF (Carpenter et al., 2010). These studies suggested that the triggering may not only be caused by transient loading of shear stress, but also decrease of shear strength due to the softening of fault materials.

Recently, the discovery of tectonic tremor has encouraged numerous observational studies targeting the triggering of tremor (Rubinstein et al., 2007; Shelly et al., 2007; Miyazawa et al., 2008; Nakata et al., 2008; Rubinstein et al., 2008; Peng et al., 2009; Rubinstein et al., 2009; Thomas et al., 2009). Tectonic tremor is abundant in number relative to local earthquakes in the transition zone on the fault, mostly associated with SSE or creep (Ide, 2008; Beroza et al., 2011). The triggering of tremor is also more frequently observed than triggered earthquakes because tremor is particularly sensitive to stress perturbations (Thomas et al., 2009; Miyazawa et al., 2005). The physics of the transient triggering process, either of small earthquakes or tremor, is similar in essence, but may reflect the slip instabilities resulted from different source mechanisms. It is important to understand the triggering process of tremor in order to have a better idea of the tremor mechanism. With the abundant evidences provided by observations, several studies have emerged to theoretically analyze the response in stress or strain change at the source region of the triggered event (Miyazawa and Mori, 2005; Miyazawa and Brodsky, 2008; Hill, 2012a, 2012b). Hill (2012a, 2012b, 2013) extensively analyzed the tremor triggering potential of passing surface waves. Hill (2008) derived the induced Coulomb

stress changes on vertical and dipping strike-slip and normal faults, due to incident of surface waves (Love and Rayleigh). The triggering of tremor mentioned in Hill's work (2010) suggests that the dynamic stresses induced by Love waves incident to strike-slip faults is more likely to trigger fault slip than those of the Rayleigh wave. To date, there have been few other numerical studies aiming toward the analysis of the triggering process of tectonic tremor.

Inspired by my observational study at Anza region along SJF, and many other observations on the triggering of tectonic tremor, the goal of this chapter is to examine the potential source conditions of triggered tremor, and the dynamic consequences of the triggering wave using a numerical approach. The precise level of stress change, type of the applied stress required for triggering, and the stress and friction history prior to triggering, are always information difficult to obtain from observational studies. Observational studies provide the empirical information sporadically, and most of the data are limited temporally and spatially. Our numerical approach will systematically investigate the nature of the incident wave and its strength in triggering fault-zone instabilities. The numerical approach provides a convenient way that we can vary the factors involved individually.

4.1.2 Previous Models of Triggering Process of Tremor

Few numerical or theoretical models have been carried out to analyze the triggering process of tectonic tremor. Conversely, the slip processes resembling earthquakes, slow-slip, and creep, after the onset of the initial instability, have been

modeled with multiple numerical methods (e.g. Lapusta and Liu, 1994; Matsuzawa et al., 2010; Noda and Lapusta, 2013). The nucleation and rupture process on a fault once a seismic event starts have also been extensively explored (e.g. Harris and Day, 1997; Ben-Zion and Andrews, 1998; Rubins and Ampuero, 2007). However, to model the triggering process prior a fault-zone instability is complex in that both high spatial and temporal resolution need to be achieved simultaneously. This is particularly true if minute slip or slip rate changes as a function of time during the slip process are the major focus. In a dynamic model, we must monitor the triggering of the instability in the spatial and temporal resolution well enough to resolve the onset of accelerating slip. It requires immense numerical calculation and storage to satisfactorily resolve spatial deformation on a realistic fault dimension while maintaining the temporal resolution during the time history.

Ader et al., (2012) tested the response of a velocity-strengthening fault to periodic stress loading with rate-and-state analytical solutions of a spring-slider. They tested specifically the sensitivity of the slip rate to periodicity of the stress loading. They used a combination of normal and shear stress changes of the same amplitudes and phase for simplicity. In their model, the period of the loading is normalized by the period at steady-state, which represents characteristic time scale for the friction to return to stability when perturbed. They found that beyond a certain period, shear stress loading with amplitude of ~2-4x10^{-4}*σ (where σ is background normal stress) or above, induced nonlinear slip rate fluctuations of high amplitude. When the period of loading fell in a specific range, their model produced a linear correlation between NVT rate and the amplitude of the

loading stress. They claimed that this slip rate amplification or fluctuation would represent NVT. However, the periods they tested are several orders (10^2- 10^4) larger than the characteristic frictional time scale of a typical fault at steady-state. Their periods of transient stress loading correspond to days or weeks, which consider perhaps the scale of slow-slip relative to the periodicity of teleseismic surface waves or regional earthquakes. Their focus was to explain the exponential relationship between slip rate and the amplitude of the stress loading. The rate of NVT they determine refers to the amplitude of the slip rate, thus directly proportional to the amplitude of the NVT waveform. Recently, Gershenzon and Bambakidis (2011) and Trugman et al.(2013) attempted to analyze the triggering of tremor using analytical solutions on their numerical Frenkel-Kontorova (FK)-type models (Gershenzon et al, 2009; Gershenzon et al, 2011). In their FK model, the dynamic frictional process between two surfaces is described by the nonlinear sine-Gordon (SG) equation. The solution of the SG equation in the limits of continuum are kinks and phonons, which they interpreted as slip pulses and seismic radiation. Gershenzon and Bambakidis (2011) constructed the plate dynamic model, which replicated tremor-like signal as an internal response of a frictional surface. Their model solved for the slip response triggered by an external stress perturbation with an emphasis on the seismic radiation and the frequency content of such response. They reported that the effective normal stress should be quite low (~0.1MPa) on a small fault dimension (~1.2km) for their model to generate signal consistent with the seismic characteristics of tremor. Their result suggests that tremor develops as non-impulsive seismic wave, which is consistent with general tremor observations. Trugman et al.

(2013) used a brittle-ductile friction model to model the triggering of tectonic tremor by teleseismic wave. The model uses a frictional parameterization that consists of discrete frictional contacts (or blocks) representing individual asperities. They applied a 20-second-period dynamic shear stress perturbation with a Gaussian wave packet as the loading from teleseismic earthquakes. The maximum shear stress used was 18 kPa. They simulated sequences of failures on individual contacts, which they claimed corresponded to each LFE in a tremor series. They established the parameter space where instantaneous triggering, delayed triggering, and no triggering occurred based upon the amplitude of the loading stresses and the background tectonic stress. However, they tested only a single period (20s) of stress loading. Meanwhile, the LFE events they simulated actually demonstrate slip rates that are barely at the lower end to be considered seismic rate (10^{-4}-10^{-3} m/s).

We aim to model the triggering of NVT by teleseismic surface waves with realistic parameters that best resemble the shear stress loading and the source of NVT. Our emphasis is on whether the triggering occurs under the tested stress or frictional conditions. Therefore, we ignore the slip process after a seismic slip has started. To avoid some of the computational issues that have hindered earlier studies, we build an analytical model, which conceptualizes the remote triggering process of tremor by teleseismic surface waves. We use the patch model by Dieterich (1979) with an analytical solution of rate-and-state friction. The strength of this solution is that the external stress loading can be easily applied to the patch model in terms of Coulomb stress, while the background frictional and stress conditions are pre-determined according to previous

estimates. In addition, the analytical solution of rate-and-state friction is very computationally efficient, so that modeling a long time duration is possible. The limitation of this model is that the spatial rupture process is not modeled realistically once the slip instability occurs. We confined our study to understand the effect of the triggering stress applied to specific background physical conditions, and to determine the factors that lead to the triggering of NVT.

4.1.3 Rate-and-state Friction

Dieterich (1979, 1981) developed the rate-and-state constitutive law for friction based on laboratory experiments at low slip rates (~10^{-9} - 10^{-5} m/s). The frictional slip phenomenon for earthquakes can as well be characterized by rate-and-state friction using quasi-static approximation on fault surfaces (Dieterich, 1992). Since this early work, earthquake rupture processes and nucleation have been modeled using rate-and-state friction in quite a few studies （e.g. Dieterich, 1987; Gomberg et al., 1998, 2000). These simulations achieved great success in understanding the slip behavior on the fault under different frictional regimes. The constitutive equation for rate-and-state friction states that:

$$\mu = \mu_0 + aln\left(\frac{V}{V_0}\right) + bln\left(\frac{V_0\theta}{D_c}\right) \quad (4.1)$$

Here, μ is the friction coefficient. It changes with slip velocity V and the state variable, θ, the averaged contact age at steady-state, over a critical slip distance D_c. The state variable reflects the sliding history effect, and consequently displacement and time-dependent effect to a frictional slip. μ_0 is the friction coefficient at a reference slip

velocity V_0. Parameters a and b are constants determined by sliding experiments in laboratory, usually thought of as the physical properties of the friction surface. The $aln\,(\frac{V}{V_0})$ part functions as a rate-dependent term for friction, and the part $bln\,(\frac{V_0\theta}{D_c})$ functions as a weakening term due to decrease of the average contact age as the fault slip accelerates. The evolution of θ with time or displacement has been discussed by Ruina (1980) and determined by Dieterich (1986):

$$\frac{d\theta}{dt} = 1 - \frac{\theta V}{D_c} \text{ , or the equivalent, } \frac{d\theta}{du} = \frac{1}{V} - \frac{\theta}{D_c} \tag{4.2}$$

In equation (4.2), u represents displacement. At steady state (when $\frac{\delta\theta}{\delta t} = 0$), the state value is fixed, $\theta = \theta_{ss} = \frac{D_c}{V}$. Then, equation (4.1) becomes:

$$\mu = \mu_0 + (a-b)ln\,(\frac{V}{V_0}) \tag{4.3}$$

This function describes the friction coefficient at steady state (Gu, 1984). The sign of parameter ($a-b$), determines how frictional strength changes according to velocity:

$$(a-b) = \frac{\partial \mu_{ss}}{\partial[ln(V)]} \tag{4.4}$$

If $(a-b)$>0, friction coefficient μ_{ss} increases as slip accelerates, representing rate-strengthening. The slip will be stable under this condition. On the contrary, if $(a-b)$<0, friction decreases as slip accelerates, representing rate-weakening. The slip will either be unstable or conditionally stable under a small range of loading rate perturbation and normal stress (Gu et al., 1984).

4.1.4 Current Knowledge of the Tremor Source

Observations of LFE and NVT at the transition zone on subduction slabs suggests that effective normal stress might be lower than lithostatic at the depth of those events, due to the presence of fluid on small asperities on the fault (Ito, 2009; Schwartz and Borosky, 2007, Rubinstein et al., 2007). Most studies suggest that the normal stress is on the scale of several tens of kPa. Meanwhile, the teleseismic triggering and tidal modulation of NVT suggests that the stress change necessary to initiate NVT is on the order of 2-40 kPa (Rubinstein et al., 2008; Peng and Chao, 2008; Thomas et al., 2009, or see summary in chapter 1). The low stress change required for triggering implies that state of shear stress on the asperity could be close to failure. The status of "close to failure" means that the shear stress on the asperity may be pre-loaded to the stage close to yield stress. Alternatively, the yield stress at the particular hypocentral region could be dramatically decreased from that implied by lithostatic stress. Nonetheless, the dimension of the asperity is thought to be small for LFE and NVT (~200-600 m; Ariyoshi et al., 2009; Ito et al., 2009; Shelly et al., 2011), implied by both the hypocenters of NVT associating with SSE and the rate of seismic moment release of NVT series in subduction zones (Bartlow et al., 2011; Ito et al., 2007). Zhang et al. (2011) show that the power spectrum of NVT in Cascadia demonstrates a high frequency fall off of f^{-2} to f^{-3}like earthquakes, instead of f^{-1} suggested by prior studies (Ide et al., 2007; Shelly et al., 2007). The f^{-2} to f^{-3} frequency fall off and 3-8 Hz corner frequency indicates that either the stress drop of NVT is as low as 0.2-5 kPa, or the presence of a much slower slip rate than earthquakes (~0.23 times the shear wave velocity). However, Zhang et al. (2011)

suggests that the f^{-2} to f^{-3} high frequency fall off supports that NVT is similar to small earthquakes. As a consequence, they estimate the asperity radius using the Brune source model (Brune, 1970), to be 105-428 m, which is in good agreement with what reported by Fletcher and MacGarr (2011). Fletcher and MacGarr (2011) investigate the averaged spectrum of NVT series near Cholame. They also observe f^{-2}fall off at high frequency, with a corner frequency range of 2.6-7.2 Hz. Using the Brune source model (Brune, 1970) modified by Boatwright et al., (1991), they estimate the asperity radius to be 200-560 m. They estimate the stress drop of NVT varying in the range of 1-40 kPa. Few studies that have successfully inferred the source dimension of NVT, aside from these estimates based on NVT spectrum. Ito et al.(2009) argue that the seismic moment rate of very low-frequency earthquakes (VLFE) is only ~0.1% the rates of short-term slow slip on subducting slab of southeastern Japan, thus the source areas of VLFE should be ~0.1% the area on which SSE occurs (on the order of hundreds of meter square with the slow slip area reported by Hiroes and Obara, 2005, 2006).

Rate-and-state friction accounts for past slip history (state, θ) and current slip rate (velocity, V). In the transition zone, (as defined in chapter 1) it is suggested that the effect of current slip velocity and the effect of slip history are closely matched in strength. That is, the difference between the constitutive parameters, a-b, in rate-and-state friction, is quite small (-0.001 ~0.004; Liu and Rice, 2005 ; Ader et al., 2012; Blanpied et al., 1991). This condition implies that, in the transition zone, fault friction is in between rate-strengthening and rate-weakening. Slip can be easily encouraged, but also easily hindered. These conditions of the rate-and-state friction allow slip onset, but then

effective hinders slip, in a spatial range that corresponds to the particular slow transient event of various sizes. The sizes of transient events correspond to the size of faulting area on which different slow transient events occur. The aseismic transient slips occupy a relatively large area (creep and SSE; 50~100 km^2), and seismic transient slips (VLF, NVT and LFE ; < $1km^2$, in descending order) on the fault occupy a smaller area. Aseismic slips are thought to occur in regions with the friction regime of rate-strengthening, while the seismic slips occur on the slip-weakening regime. The size of a fault can be easily varied in model experiments that we can simulate the slip processes of these smaller events.

The critical slip distance, D_c, represents a minimum slip distance over which the old contacts between two sides of the fault break and are renewed with new ones. The D_c in laboratory measures range from $2\times10^{-6} - 10^{-4}$m (Dieterich, 2007). These are orders of magnitude smaller than field estimates ($10^{-3} - 10^{-2}$ m). However, field-based estimates do not usually account for the existence of fault gouge and other possible weakening mechanisms involved, which would lead to increase of D_c. With the introduction of gouge, D_c may reduce 2 orders of magnitude depending on the thickness of the active shear band (Marone, 1998). As a consequence, the upper bound of D_c in laboratory scale is the estimated D_c values for mature faults that is commonly used. The initial slip rate is usually set as the tectonic plate rate (~1×10^{-9}m/s; Lapusta and Barbot, 2012) or lower in numerical models for transient slip processes. In the model, slip rates on the order of 10^{-12}m/s are considered locked, and above $10^{-1} - 1$m/s are considered seismic slip rates for earthquakes (Lapusta and Rosakis, 2007).

In short, the source of NVT is currently thought as asperity of small dimension (likely ~1x1 km^2) on the fault, where the constitutive rate-and-state friction parameter (a-b) <0, but very close to zero on the order of ~0.001-0.004. The asperity is likely embedded in a zone on the fault where the friction function as rate-strengthening. The background effective normal stress is low, likely on the order of tens of kPa. The slip rate of a NVT, that once slip is initiated, is at least 10^{-1} m/s or above.

Enlightened by the triggering observation of NVT in Anza (Chapter 2), we aim to replicate the triggering process of NVT with a model, in which the external loading resembles that of a remote teleseismic event. We construct an analytical model tailored to incorporate current estimates of the source mechanism of NVT, from observation, theory or laboratory experiments. We use the most numerically feasible method that can simulate the slip and slip rate acceleration before and during the transition to an actual seismic event. The slip event occurs on a single asperity with small dimension, replicating the tremor source. Meanwhile, the simulation reproduces the nucleation (triggering phase) as a function of time, with not only sufficient resolution, but also enough duration to resolve the time delay before slip rate goes unstable. We incorporate many physical conditions as close as possible to what are observed or estimated from previous studies. However, some conditions are compromised to the extent that they are applicable in the model. This work supports some of the previous estimates and observations of NVT mechanism, while revealing possible adjustments to others. It will help enhance our understanding about the mechanism of NVT.

Several numerical approximations have been used to dynamically simulate slip on a frictional fault plane embedded in an elastic medium, including the finite difference, finite element, spectral element, and boundary integral methods. Most dynamic models emphasize modeling the spatial and temporal stress and deformation responses once rupture begins. The reason is that dynamic modeling typically is computationally expensive. It calculates the stress and slip solutions on each spatial grid at each time step, stores the solutions, and moves forward to next time step. The computations increase dramatically if finer spatial or temporal resolution is required. Furthermore, the numerical time-marching methods are usually subjected to a stability condition for the solutions, called Courant–Friedrichs–Lewy (CFL) condition. The CFL states that $\frac{\Delta t \times V_s}{\Delta x} \leq C_{max}$(Courant et al., 1928), in which the Δt and Δx represents temporal and spatial resolutions, V_s is shear wave velocity, and C_{max} is an upper bound depending on the mathematical method used in the solution. In other words, the temporal resolution, Δt, is tied to spatial resolution, Δx (considering 1D here for simplicity). The smaller the dimension of asperity on the fault that we wish to investigate, the smaller the time increment required in our dynamic models. Under such condition, dynamic models for the source of NVT, which is usually orders of magnitude smaller spatially than that of typical earthquakes, require extremely small time increments (in $\leq$~0.001 seconds). In contrast, the remote triggering process of NVT is usually hundreds of seconds in time duration. The small time increments impose intensive computational requirements in storing the forwarded temporal solutions until the end of each test. Therefore, dynamic

modeling is not currently practical for multiple simulations and investigations of parameter space, as in our case.

Our goal is to capture the slip responses before the onset of dynamic rupture, starting from the locked state of the fault, to a mature rupture. Meanwhile, the quasi-static approximation using the analytical patch model accommodates rate-and-state friction effectively (detail explained in section 4.2.1). Thus, we choose the analytical solutions on a simplified patch model in our study.

4.2 Methods

4.2.1 The Rate-and-state Analytical Solutions

We use earthquake rate formulations based on rate-and-state friction (Dieterich, 1979, 1994, summarized in 2007). The equations express the effect of stress changes on earthquake rate in two aspects. One of the aspects is solely the slip and slip rate induced by stress change on a fault patch at steady-state. The other aspect focuses on the change in seismic rate induced by stress change on a fault, and consequentially the accumulated number of events over time. The original equation used the Coulomb stress function S (and as a result, the Coulomb stress rate $\dot{S}$), which combines the shear stress and normal stress rates:

$$\dot{S} = \dot{\tau} - \mu \times \dot{\sigma} \tag{4.5}$$

However, in our study, we only vary the shear stress rate for simplicity. Therefore, we substitute the Coulomb stress rate to shear stress rate, $\dot{\tau}$.

The slip and slip rate can be described in a pair of equations:

For slip: $\delta = \frac{-a}{h} \ln\left\{\frac{\dot{\delta}_0 h\sigma}{\dot{\tau}}\left[1 - \exp\left(\frac{\dot{\tau}t}{a\sigma}\right) + 1\right]\right\}$ (4.6)

For slip rate: $\dot{\delta} = \left\{\left[\frac{1}{\dot{\delta_0}} + \frac{h\sigma}{\dot{\tau}}\right]\left[\exp\left(\frac{-\dot{\tau}t}{a\sigma}\right) - \frac{h\sigma}{\dot{\tau}}\right]^{-1}\right\}$ (4.7)

when $\dot{\tau}$=constant but not zero over the time duration. Over a short time increment Δt, we assume that $\dot{\tau}$ equals to constant is reasonable and therefore equation (4.6-4.7) applicable. When $\dot{\tau}$ is zero, the equations are:

For slip: $\delta = \frac{-a}{h} \ln\left\{1 - \frac{\delta_0 \dot{h}t}{a}\right\}$ (4.8)

For slip rate: $\dot{\delta} = \left\{\frac{1}{\dot{\delta_0}} - \frac{-ht}{a}\right\}^{-1}$ (4.9)

in which a is the constitutive rate-and-state parameter, h is a term combining model and constitutive parameters such that $h = \frac{b}{D_c} - \frac{K}{\sigma}$, the K is fault stiffness, and b and D_c are other constitutive rate-and-state parameters described in 4.1.3. σ is background normal stress, $\dot{\delta_0}$ is initial slip rate on the fault, and t is the time duration in seconds.

These equations are the solutions derived analytically for a simplified 2D fault patch of fixed length (Dieterich, 1992). The patch model was embedded in an elastic medium, and subjected to a remotely applied stress. The slip and slip rate conditions along the fault were represented by the center-point of the patch. The numerical realization of this model was employed on a spring-slider of 1D freedom with spring stiffness K. This numerical model assumes that the slip evolving to nucleation of an instability is in progress, and that the slip rate is much greater than the steady-state slip rate ($\dot{\delta} \gg \frac{D_c}{\theta}$) during the simulation. These solutions have been shown to be consistent

with both detailed 2D simulations and laboratory observations of the nucleation process on a 2m fault (Dieterich, 1992; Dieterich and Kilgore, 1996a).

Additionally, with equations 4.5-4.8, the earthquake rate following a stress step can be solved and expressed in the following equations (Dieterich, 1994):

$$\gamma = \left(\gamma_0 - \frac{1}{\dot{\tau}}\right) \exp\left(\frac{-t\dot{\tau}}{a\sigma}\right) + \frac{1}{\dot{\tau}} \tag{4.10}$$

For seismic rate: $R = \frac{r_0}{\gamma \dot{\tau}_0}$ (4.11)

when $\dot{\tau}$ =constant but not zero. When $\dot{\tau}$ is zero,

$$\gamma = \gamma_0 + \frac{1}{a\sigma} \tag{4.12}$$

The variable γ is a parameter which affects how the seismic rate evolves with stress loading and time. This variable at steady-state is the inverse of the background tectonic rate, while R is current seismic rate. The γ_0 is the background seismic rate under tectonic stress loading. $\gamma_0$is γ at steady-state . This set of equations (4.10-4.12) is based on the assumption that seismicity is a sequence of nucleation events in which the stressing rate would determine the timing of the earthquakes (Dieterich 1979). This set of equations has also been implemented in a 1D spring-slider to model the effects of stress step, seismic transient stressing and tidal loading to the nucleation of earthquakes (Dieterich, 1987; Gomber et al., 1998, 2000).

We use equations (4.6-4.12) to numerically solve for slip rate, seismic rate, and accumulated number of seismic events induced by external shear stress loading. The accumulated number of seismic events with respect to time is calculated by integrating the seismic rate within the time duration that has lapsed. The external shear stress loading

is from either periodic sine functions, or from true teleseismic earthquake records. It is worth noting that the two sets of equations (4.6-4.9 and 4.10-4.12) refer to the same rate-and-state constitutive law, but are expressed in two different perspectives. We model the occurrence of an instability on a fault from the perspective of slip rate increase. The seismic rate on the fault increases during the stress loading, and we record the resulting change in the accumulated number of seismic events over the duration of each simulation. In both cases, we monitor the effect of external stress loading on the triggering of slip instability.

In the simulation of slip rate, we start by an initial slip rate, $\dot{\delta_0}$, based on tectonic shear stress loading rate:

$$\dot{\delta_0} = \left\{\left(\dot{\delta} + \frac{h\sigma}{\dot{\tau_t}}\right)\exp\left(\frac{t_{i0}\dot{\tau_t}}{a\sigma}\right) - \frac{h\sigma}{\dot{\tau_t}}\right\}^{-1} \tag{4.13}$$

which is derived from equation (4.7). In equation 4.13, $\dot{\delta}$ is the slip rate we determined as that of an instability (definition in 4.2.3), the $\dot{\tau_t}$ is the rate of tectonic shear stress loading, and the t_{i0} is the initial time to instability, or alternatively, thought of as the inverse of a background/initial seismic rate. In other words, the time to instability is the time between seismic events, and therefore, it also represents the inverse of the rate of the event.

We also calculate an initial shear stress:

$$\tau_0 = \sigma \times \left[\mu_0 + a\log\left(\frac{\dot{\delta_0}}{\dot{\delta_r}}\right) + b\log\left(\frac{\theta \times \dot{\delta_r}}{D_c}\right)\right] \tag{4.14}$$

Here, the background shear stress is determined by normal stress times the new friction coefficient, which is calculated from background slip rate, the default reference

slip rate, $\dot{\delta}_r$ (10^{-8} m/s in our models), and other constitutive rate-and-state parameters explained in section 4.1 (Dieterich, 1987) .

We incorporate the effect of external shear stress changes and form a current shear stress at each time step. Then, we solve for the new time to instability, t_i, based on the new shear stress after stress perturbation :

$$t_i = \frac{a\sigma}{\dot{\tau}_t}\left[\log\left(\frac{1}{\dot{\delta}_i} + \frac{h\sigma}{\dot{\tau}_t}\right) - \log\left(\dot{\delta} + \frac{h\sigma}{\dot{\tau}_t}\right)\right] \quad (4.15)$$

This new time to instability can be consequently supplied to equation (4.13), and solve for the new slip rate for next time step. The whole process forwards in each time step until the slip rate reaches the value we arbitrarily set for the instability.

It is worth noting that the time increments in this iteration are variable ($\Delta t \geq 10^{-10}$ seconds). This is because the length of the time increment depends on the value solved in equation (4.15), and this time step marches in large increments at low slip rate, from (4.13), but decreases rapidly while slip rate increases. In the case where we test applying true shear stress histories of the teleseismic waves used in Chapter 2, we start from a Δt= 0.025 second sample rate and decrease the time steps when slip rate starts to rapidly increase. We verify that all time increments are small enough to resolve the evolution of slip rate smoothly.

In the simulations of seismic rate and accumulated event numbers, we set up the background seismic rate, r0, and background tectonic stressing rate, $\frac{1}{\gamma_0}$. We test the effect of changing γ_0 in some simulations, but we set background tectonic stressing rate arbitrarily in all of our tests for consistency. Under such initial values, the external shear

stress loading, $\dot{\tau}$, adds up and form current shear stress. We update the γ in each step supplying $\dot{\tau}$ to equation (4.10), and sequentially update the new seismic rate R in equation (4.11). We can calculate accumulated number of event, N, over the duration of simulation as $N = R \times \Delta t$. In this set of simulations, we run the simulation until the termination of the external shear stress loading. However, the termination of the external loading is set well beyond the time of instability, or no triggering of instability could be confidently determined.

4.2.2 Physical Parameters for the Model

With the equations (4.6-4.15), we can solve for the slip rate, seismic rate, and the accumulated number of event, provided that the shear stress history and background parameters are given at any time during the simulation. For the source region, we set up background physical parameters on the fault that closely resemble the source properties of NVT based on observations (in section 4.1.4). We argue that the triggering of the instability in our model is comparable to the triggering of the NVT with such physical conditions. The background physical parameters common to our tests are given in Table 4.1.

Rate-and-state constitutive parameters	value	units
μ	0.3	N/A
a	0.008	N/A
b	0.012	N/A
a-b	-0.004	N/A
θ	3.1536E+08	seconds
D_c	1.113E-05	meters
physcial paramters		
tectonic stressing rate	2	Pa/day
initial time to instability (1/background seismic rate)	10	months
background normal stress	50-700	kPa

Table 4.1 Common background physical parameters on the fault patch in our model.

For the rate-and-state constitutive parameters, we used a small friction coefficient (0.3, which is half of the value of 0.6 that is typically used to model earthquakes; Dieterich, 1992; Dunham et al., 2011) to simulate a weak fault. This friction coefficient is set arbitrarily and should be considered a weak effective friction coefficient due to possible gouge material on the fault zone (explained in section 4.1.4). We use (a-b) = -0.004 for a mildly rate-weakening frictional regime, which is consistent with the high end of what used in Liu and Rice (2005). The state variable, θ, is equivalent to an age of ~10 years, which represents a young asperity on the fault. In other words, the asperity on the fault has been stable from failure for an average of 10 years. The 10-years-age is significantly short compared to characteristic earthquake recurrence interval (250-10000 years; Brenda et al., 2013). This is an arbitrary guess to the average age of the asperity, which is considered the source of NVT on the fault. Some of the rate-and-state parameters are conventional values, like the a, b and D_c, since we have no direct

estimates or reference to change them from the conventional values (a and b values, Dieterich, 1992; Dc, Dieterich, 1981a, 1992). We did not vary the rate-and-state parameters in each simulation, because we want them kept as control factors while focusing on the background stress conditions and the triggering stresses. In addition, since the analytical solutions from equations (4.6-4.15) correspond to the patch model of Dieterich (1992, 1987), which involves no parameter relative to the dimension of the asperity, we do not need to set the fault dimension in our analytical simulation.

For the stress conditions on the fault, we vary the background normal stresses in the range of 50-700 kPa. The background normal stresses in our tests are small relative to those estimated on the fault zone for earthquakes (50-200 MPa). We assume the background normal stress is low, which is implied by the low effective normal stress caused by potential pore-fluid at the source of NVT (Ito, 2009; Schwartz and Borosky, 2007, Rubinstein et al., 2007). The value of normal stress is kept constant in each simulation, but they may differ among tests when necessary (detail explained in section 3.2.4).

We validate how well the analytical solution performs relative to a 2D dynamic model in a comparison test. We choose the Boundary Integral Equation method (BIEM) for the dynamic model, which is quite numerically efficient in physical situations such as ours, with homogeneous material and no free surface. Fukuyama and Madariaga (1995,1998) implemented and then improved the Boundary Integral Equation (BIE) while solving earthquake problems. This method solves the wave-equation in a homogeneous 3D elastic medium. The solution is symmetrical across the crack (or fault

plane), with boundary conditions of stress, displacement, and friction. Most important of all, only the fault plane is discretized and there is no computation required in the surrounding 3D medium. The BIEM uses analytical Green's functions, so it reduces computation in that all the interactions between element pairs involved in the problem are solved only once. The solutions are then used repeatedly in all model tests with the same geometry and friction law, but different initial stresses if desired. The spatial convolution is done in the frequency domain. These solutions make the BIEM method more numerically efficient than finite element or finite difference methods for the physical configurations we desire. Our specific implementation is the Multi-Dimensional Spectral Boundary Integral Code (MDSBI) written by Eric M. Dunham from Stanford University to simulate slip resembling the triggering of NVT (Dunham and Rice, 2008). Dunham incorporates several versions of rate-and-state friction and accounts for slip-strengthening as well as rate-strengthening friction. MDSBI provides for us a convenient tool to simulate NVT nucleation dynamically using rate-and-state friction.

Our model for the comparison test is conceptualized and illustrated in Figure 4.1.

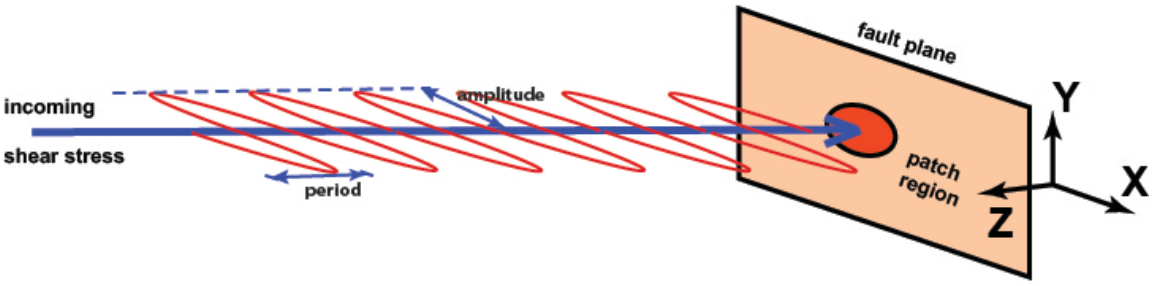

Figure 4.1 Illustration of the setting simplified to model triggering of tremor by transient shear stress change.
We assume the orange patch represents the source of tremor (or instability) on a 2D fault (in XY plane). The transient shear stress change is induced by teleseismic wave with single period and amplitude at each test. The periodic change of shear stress is shown here as the red curve. The purple arrow pointing toward the fault plane is the incoming direction of the wave, perpendicular to the fault (Z direction).

In the dynamic model, the fault is set as a vertical, right-lateral, strike-slip plane. The source on which the instability occurs is set as a circular asperity on the fault plane. The fault plane is preloaded by a regional stress field close to critical-failure stress (yield stress), and then slips under rate-and-state friction. We adopt the definition of 'asperity' as an area on the fault that is previously locked (slip rate fairly close to 0); hence shear stress accumulates here and is closer to failure stress than the surrounding region. In the dynamic model, we test in multiple simulations and find the yield stress of the in good approximation. Then, we set the initial shear stress in several kPa range, which is fairly close to the yield stress at the start of with the comparison test. Therefore, in the analytical model, the initial slip rate and time to instability can be defined by the same value of initial shear stress as that in the dynamic model. In this comparison test, we use the same set of parameters for the background physical conditions on the fault, as well as apply identical periodic loading of shear stress to the fault (detail described in section 4.2.3), in both the dynamic and analytical models. The major difference lies in that we set up the fault dimension for the dynamic model as a patch of 10x10 km^2, with a 2 km radius circular asperity embedded in the center. The dimension of the asperity is slightly larger than the scale of those estimated by previous studies ($\sim \leq 1 km^2$; See summary in section 4.1.4). This dimension is set in compromise to accommodate a numerical time increment practical to our case. Specifically, the time increment of the simulation is reduced to 0.001 seconds, which is small relative to the total duration of a teleseismic wave (~ hundreds of seconds). The small time increment imposes a numerical burden on the dynamic model from simulating a large number of time steps, which ties into the

limitation of dynamic models described in section 4.1. The total duration of the simulation is also consequently set to 5 seconds in order to accommodate such numerical limitation. We simulate a short duration of shear stress loading with much shorter period than the natural periods of the teleseismic surface wave. This is done in order to accommodate the requirements in dynamic model and make the comparison test feasible. Later in our simulation tests using rate-and-state analytical solutions, we retain the natural characteristics on periods and duration of teleseismic surface waves. The parameters of the fault for this validation is given in Table 4.2. These parameters are generally similar to those in Table 4.1. However, some of them are modified specifically for the computation limits of the dynamic model, in order to fit the purpose of the comparison test.

General model settings in the dynamic model		**units**
Grid spacing	100	meters
fault elements in x and y	100x100	N/A
asperity radius	2	km
asperity central point	(x,y)=(0,-10)	km
time increment	0.001	seconds
Compress wave(P) velocity	6.00	km/s
Phase velocity(shear wave velocity)	3.4641	km/s
constitutive parameters in rate-and-state friction		
reference friction coefficient	0.6	N/A
a	0.008	N/A
b	0.012	N/A
D_c	1.11E-05	meters
reference slip rate	1.00E-08	m/s
Initial physical conditions		
background shear stress	40 on the asperity	kPa
	39 elsewhere on the fault	kPa
background normal stress	54.5	kPa
θ	4.63E+06	seconds
Peak amplitude of loading shear stress	1.5	kPa

Table 4.2 The model parameters used in the dynamic model and in the comparison test.

4.2.3 Shear Stress Loading and definition of triggering

We apply an external shear stress loading to the model to resemble the transient stress loading from the teleseismic earthquakes. We first simplified the external shear stress to a sinusoidal function with period ω and amplitude A:

$$\tau = A\sin(-\omega t) \tag{4.16}$$

In the above equation, the ω is angular frequency.

In addition to testing our models with periodic loading, we also apply the shear stress loading of each 44 teleseismic earthquakes, obtained from the velocity waveforms of these earthquakes. We project the waveforms to radial and transverse directions with respect to the strike and dip of SJF (317 degrees NE and vertical dip). Although the particle motion of the wave in radial direction induces equivalently change of the normal stress and shear stress on the fault, which is also a crucial factor in the triggering process, we select only the transverse direction for simplicity. This simplification means that our models don't include the effect of the reduction of normal stress, which can also encourage the triggering of NVTs; triggering may be less likely in our models than in real life. The peak amplitudes of the velocity record in transverse direction closely approximate the shear wave energy, especially that Love wave would contribute most to inducing the shear wave energy (Hill, 2012b). We convert the peak ground velocity measured for each earthquake to peak shear stress, with shear modulus 30 GPa, and phase velocity of 4 km/s using equation (4.1). Then, we scale the velocity records (teleseismic earthquake data used in Chapter 2) in transverse direction to a set of peak shear stress values to obtain the shear stress loading histories from all 44 events.

The shear stress records described above are applied to the analytical model in sequences of tests (described in 4.2.4). Our model solves for slip rate or seismic rate in each time step. The seismic rate referred in our study refers to the recurrence rate of NVT or the instability that resembles the triggered NVT (in units of number per day). The seismic rate is directly related to time to instability in that the seismic rate is the reciprocal of the time it takes for the next event occurs. We arbitrarily set that when the slip rate exceeds 10^{-3} m/s, the slip is unstable. We define the triggering of NVT has occurred when this threshold slip rate is reached. We have confirmed in numerous tests that a slip that evolves to this slip rate would continue to accelerate to infinity within the next few time steps. Thus, the choice of this threshold slip rate has negligible effect on estimate of the time-to-failure..

4.2.4 Designed Tests for the Triggering of the NVT

First, we performed a sequence of tests applying a synthetic, sinusoidal shear stress loading to the analytical model. This set of tests was designed to clarify the effect of the period and amplitude of the external loading on the triggering process. In these tests, we systematically vary the period ω, and the shear stress amplitude A of the external loading in equation 4.16. We first vary the period of the stress loading in the range of 10-70 seconds, with 10-second increments, while we fix the background normal stress and amplitude of the shear stress loading for each period. Then, we test varying the background normal stress with respect to each period in the first test. In these simulations, we found that with a fixed period, the effect of increasing the amplitude of the external loading was similar to that of decreasing the background normal stress.

Hence, we represent the amplitude of loading stress and the background normal stress as a composite parameter, normalized stress, in our result figures. This is referred as $\frac{\tau}{\sigma}$.

We test the effect of the periodic shear stress loading both on the slip rate instability, seismic rate, and consequently the accumulated seismic numbers. In the tests of the slip rate instability, we record the time when slip rate reaches 10^{-3} m/s in each test of a fixed period and specific normalized stress. The time of instabilities are recorded in units of seconds. At times, we would convert the time of instabilities to the number of cycles derived from the corresponding external loading period. In the tests of the accumulated seismic events, we run the simulations fixing the period of stress loading or background seismic rate one at a time, and observe the effect of individual parameters to the triggering of NVT based on the accumulated number of NVT.

Second, we apply the estimated time histories of shear stress loading from 44 teleseismic large earthquakes ($M_w \geq 7.0$) to the model, which solves slip rate at each time step until instability occurs. In this set of tests, shear stress loading from the true teleseismic records is the information used to constrain the background physical conditions (e.g. Figure 4.2). The shear stress change is constructed from the peak shear stress records of the teleseismic earthquakes shown in Chapter 2. We know there is one triggering of NVT out of the 44 events: the 2002 Denali earthquake triggered 12 NVTs. With such information, we search in the parameter space of the background normal stress and background seismic rate for the parameter sets that permit the triggering of NVT consistent with the observed triggering pattern. We sequentially change the background normal stress and the background seismic rate, run the simulation of slip rate, and then

record whether triggering of instability occurs or not (e.g. Figure 4.3). This procedure is done with two major teleseismic records, the 2002 Denali and the 2009 Gulf of California earthquakes, since the other 42 events induced relatively low peak shear stress which triggered no tremor. In this set of tests, we only record whether triggering of NVT occurs or not, during the 800-second of the shear stress loading. We ignore the complexity about matching the timing of the triggered NVT solely for simplicity.

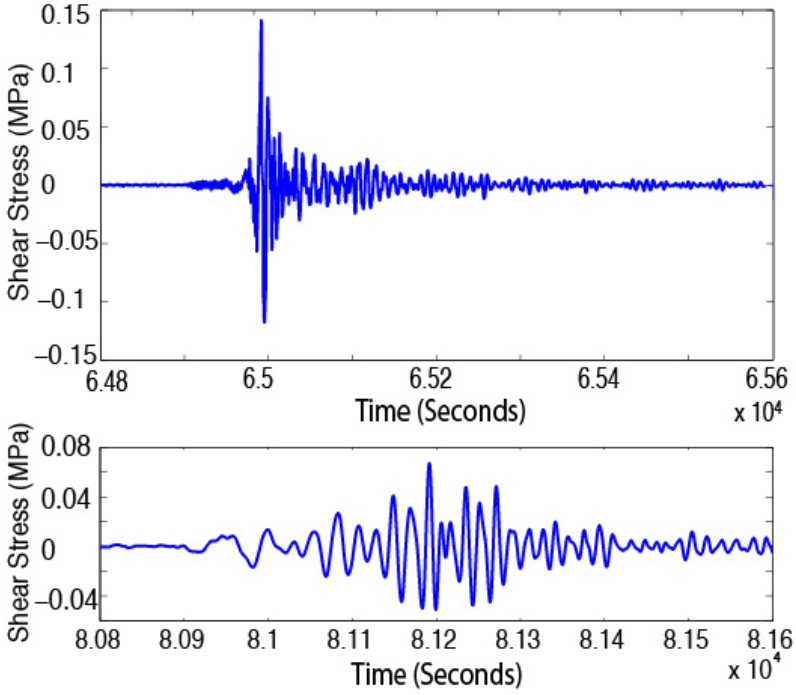

Figure 4.2 The shear stress histories as external loading to the model.
The shear stress histories are demonstrated here based on two major events. The upper panel shows the shear stress induced by 2009 Gulf of Mexico (M_w 6.5) earthquake. The lower panel shows the shear stress induced by 2002 Denali earthquake (M_w 7.8). Note that the time durations are cropped to match the same scale, while the amplitudes are in the unit of stress (MPa).

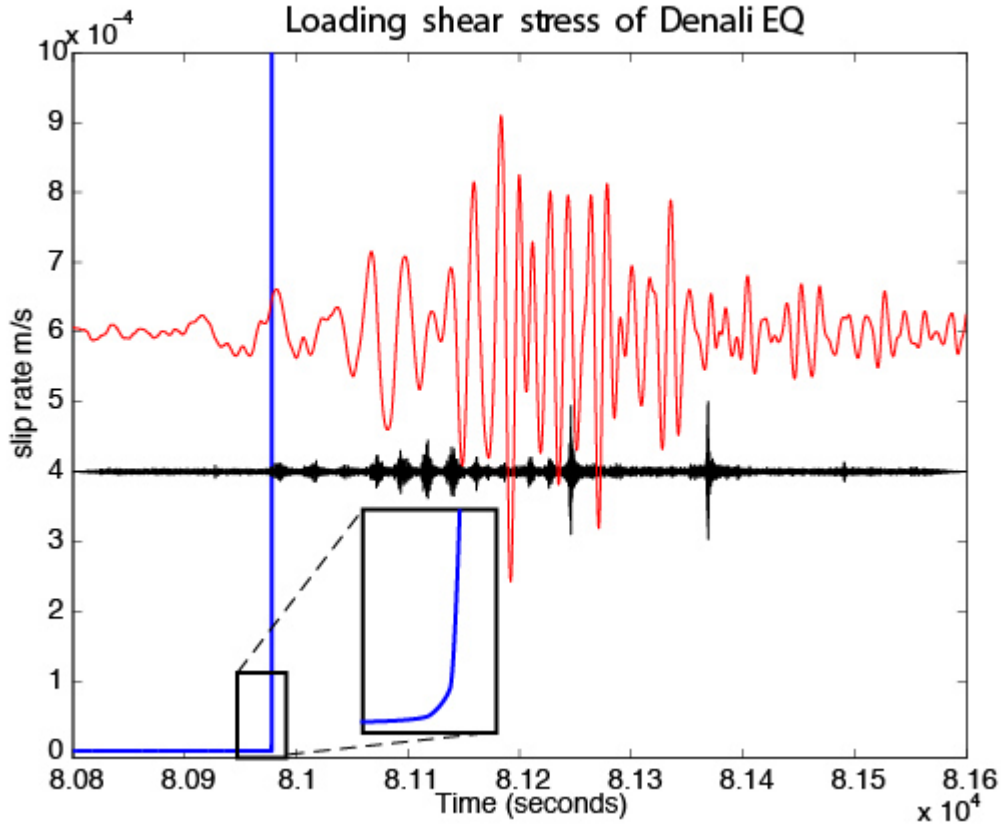

Figure 4.3 Example simulation of slip rate using the true shear stress loading from 2002 Denali earthquake (M_w 7.8).
The parameters in this particular test are: background normal stress 400 kPa, and background seismic rate 3.3e-3/day (equivalent to time to instability of 10 months). The blue line shows the slip rate record. At 80987 seconds, the slip rate accelerates rapidly to beyond 10-3 m/s, indicating that instability has occurred. The black rectangular in the inset shows a zoom-in to the detail of the slip rate curvature close to the time of instability. The red curve is the shear stress loading history overlaid to this plot for the illustration of the shear stress loading. The black curve shows the waveform filtered from 2-15 Hz to illustrate the triggered NVT bursts along with the teleseismic surface wave and the triggered onset of slip rate. Note that the amplitudes of red and black curves are not to scale, only for illustration purpose. True amplitude of the red curve can be referred from Figure 4.2

Likewise, we perform the tests solving the induced accumulated number of events due to the true shear stress loading from the two earthquakes (e.g. Figure 4.4). We apply shear stress loading records from the 2002 Denali earthquake and 2009 Gulf of California earthquake. We search the parameter space of background normal stress and background

seismic rate for a zone that would satisfy the true number of triggered NVTs in both cases. From the observations we found that Denali earthquake triggered 12 NVT bursts during the 800-second simulation. Meanwhile, the Gulf of California earthquake triggered none. For the case of Gulf of California earthquake, we take the results of fairly small number of accumulated events, likely on the order of 0.001/day (equivalent to $\leq$0.01 per 800 seconds). Such small number best represents the fact that there is no triggering of NVT by the Gulf of California earthquake.

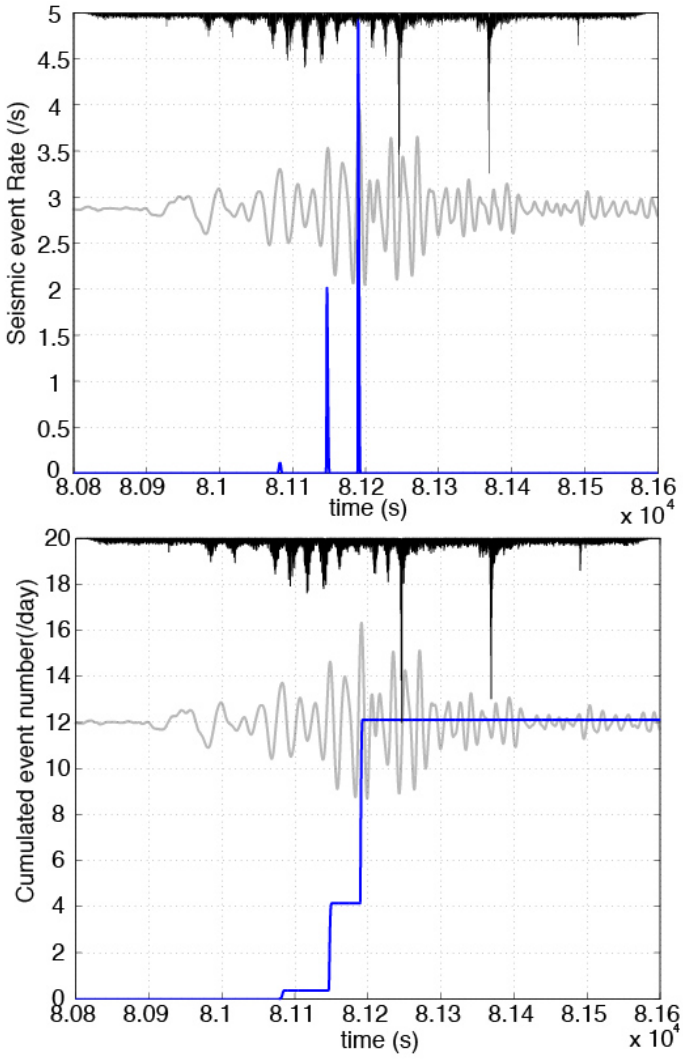

Figure 4.4 An example of the induced seismic rate and the accumulated number of events by the shear stress loading of the 2002 Denali earthquake.
The procedure used to solve for the blue curves are identical to what used in plotting figure 4.7, bottom panel. The blue curve in the top panel shows the seismic rate solved by equation (4.10). The blue curve in the bottom panel shows the accumulated number of events. The gray curves in the background show the shear stress loading of the 2002 Denali earthquake. The black curves on the top show the negative absolute amplitudes of the velocity waveform of 2002 Denali earthquake, filtered to 2-15 Hz. The gray curves are plotted to illustrate the timing of peak seismic rate coincident to the shear stress loading. The black curves are plotted to illustrate the triggered bursts of NVTs in the actual data. In this particular example, we use background seismic rate of 0.2/day.

4.3 Results

4.3.1 Comparison of the Analytical Solution with BIEM Dynamic Solution

We perform a test comparing models of the same physical configuration on the fault and the external stress loading, using our dynamic model and the analytical solutions of rate-and-state (equation 4.12-4.14). The background physical parameters for this comparison test are given in Table 3.2. The shear stress loading is sinusoidal with 2-second period and a peak shear stress of 1.5 kPa. In this case, the initial stage of the shear stress over normal stress is 0.734 (unitless). This value is equivalent to an initial stage of dynamic friction coefficient ($\tau = \mu \times \sigma$; thus $\mu = \frac{\tau}{\sigma}$). The 0.734 is larger than the steady-state friction coefficient, 0.6, set in the simulation. In rate-and-state friction, this condition is unstable and the instability is determined to occur. With identical settings, we find that the slip rates generated by both the analytical model and the dynamic model trigger the instability at the third cycle of periodic loading (red and blue curve; Figure 4.5). In the first and second cycle of periodic loading, there are slight bulges of slip rate increases. We note slight delays (~0.5 seconds) of the slip rate increase in the dynamic model relative to that of the analytical model. These delays result from an averaging effect of the slip from the dynamic model due to the finite rupture propagation speed in the dynamic models. The blue curve shown in Figure 4.5 is the averaged slip rate on the entire asperity (or patch) in the dynamic model. The slip rate increase initiated from the center of the spherical asperity in the BIEM model. This slip rate at the centroid remained the highest over the fault, and propagated radially to the edge of the asperity over the time of the simulation. The slip rate of the dynamic model at the centroid has the highest

amplitude within the bulges, and the peak amplitudes are slightly higher than that of the analytical model. The smearing out of the slip rate in the dynamic model is a spatial effect not captured in the analytical model. However, we find that overall the analytical model behaves in a manner consistent with the dynamic model. Hence, it is shown to be legitimate to take the advantage of the efficiency of the analytical solutions. It is especially true when we need to explore the parameter space that is not available to the dynamical model due to computational expense.

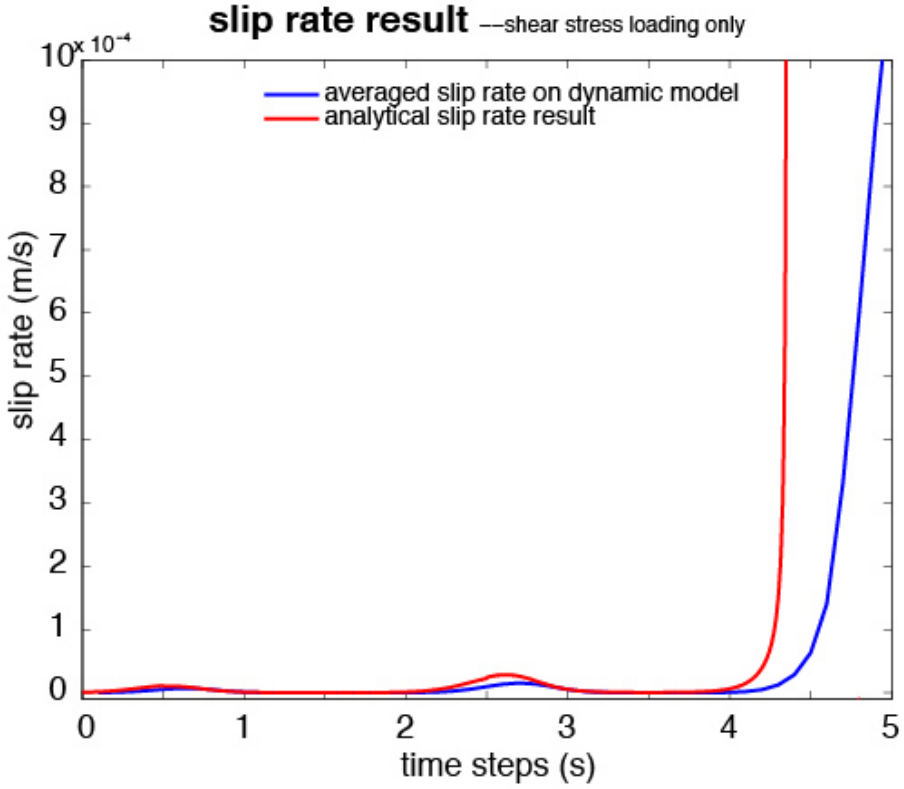

Figure 4.5 Comparison of the slip rate results from rate-and-state analytical model and from BIEM dynamic model.
The blue line represents the slip rate averaged over the entire area of the patch on the dynamic model. The red line represents the slip rate of the analytical model. The curvature of the slip rate from the dynamic model is averaged across the patch and is therefore slightly different from that of the analytical model. The slip rate at the third onset rapidly rises to beyond 10^{-3} m/s, and we consider that triggering occurs.

4.3.2 NVT Triggering by Periodic Shear Stress Change

From the simulations in which the shear stress loading consists of monochromatic sine waves, we observe that the period has only a weak effect on the time of triggering (Figure 4.6 (B)). In Figure 4.6(A) or (B), we see that the time of triggering increases slightly as the period of the loading increases. However, over the space of parameters we tested, only in a small range of normalized stress did this mild effect take place. In addition, the effect of triggering delay is more prominent when the loading is at short periods (10-40 seconds). At periods beyond 40 seconds, the slip rate becomes insensitive to the period of the loading. Rather, in the parameter space we tested, the triggering of the NVT is more sensitive to the relative amplitude of shear stress loading to background normal stress than the period of the loading. We find that there are distinct range of normalized stress in which triggering of NVT would and would not occur. For a ratio of 0.098 - 0.13 of the normalized stress, we find that the triggering occurs but can be delayed after several cycles of the stress loading. However, below 0.098, the triggering of NVT does not occur. Above 0.13, the triggering of NVT instantaneously occurs in the first period of the loading. That is to say, in terms of a background normal stress of 70 kPa, the shear stress loading with a peak value below 6.86 kPa would not trigger any NVT. Alternatively, the shear stress loading with a peak value above 9.1 kPa would always trigger NVT spontaneously and almost immediately. This estimate is based on the assumption that the background normal stress is in the range of 70-165 kPa, which is low in order to resemble source of NVT. We note that the background seismic rate is 0.0033/day in our models. This background seismic rate corresponds to only 1 NVT

occurring on average of 10 months, if there is no external loading other than the tectonic stress. Under the effects of periodic shear stress loading with a peak value above 6.86 kPa, NVT would be triggered within 10-70 seconds.

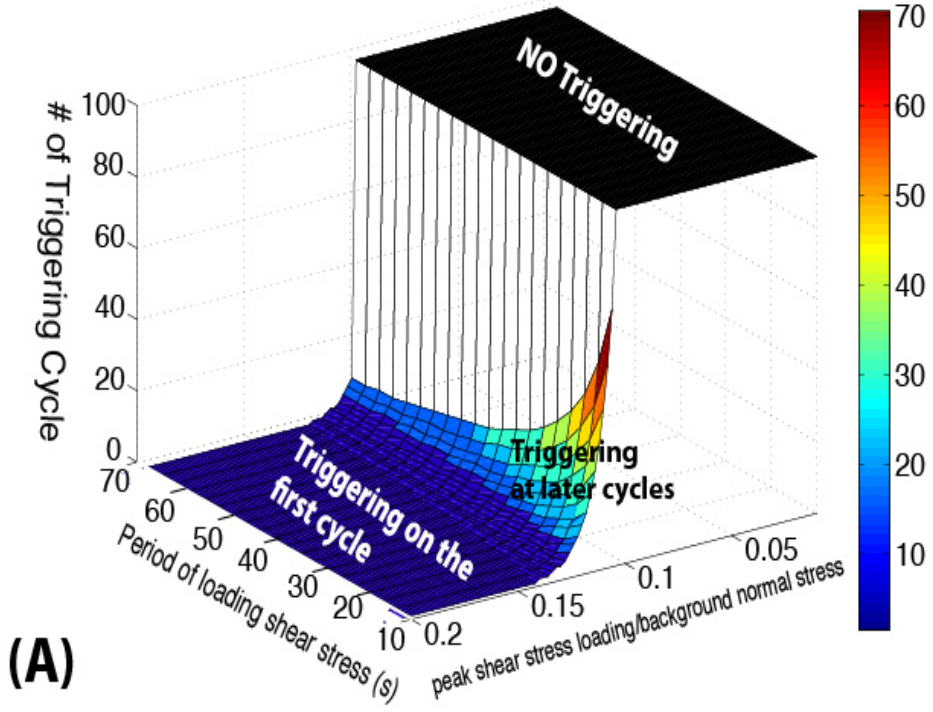
NO Triggering
Triggering on the first cycle
Triggering at later cycles
# of Triggering Cycle
100
80
60
40
20
0
70
60
50
40
30
20
10
Period of loading shear stress (s)
0.2
0.15
0.1
0.05
peak shear stress loading/background normal stress
70
60
50
40
30
20
10

(A)

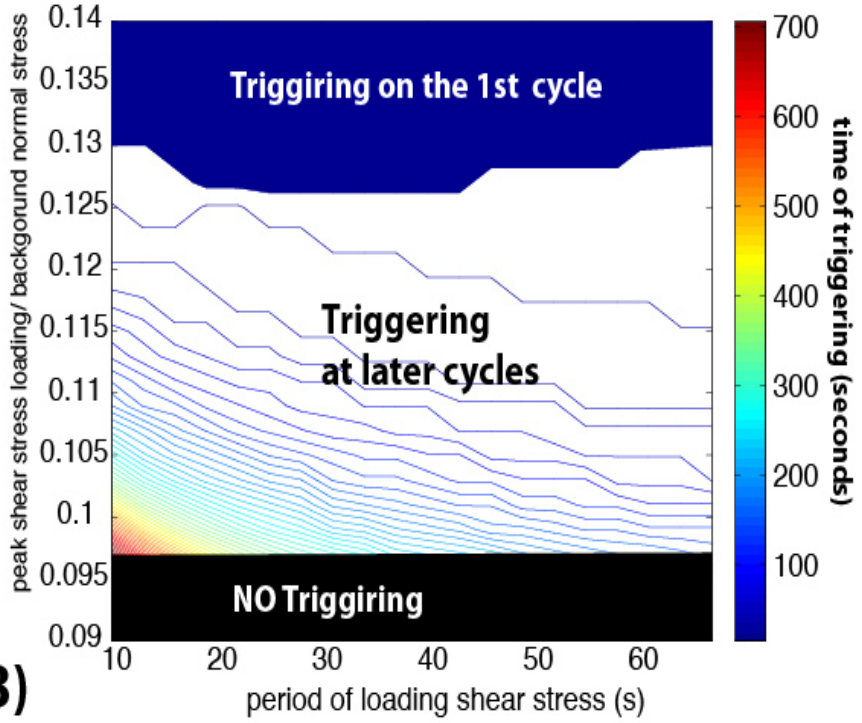
Triggiring on the 1st cycle
Triggering
at later cycles
NO Triggiring
peak shear stress loading/ backgorund normal stress
0.14
0.135
0.13
0.125
0.12
0.115
0.11
0.105
0.1
0.095
0.09
10
20
30
40
50
60
period of loading shear stress (s)
700
600
500
400
300
200
100
time of triggering (seconds)

(B)

Figure 4. 6 The triggering of the instability with respect to two sets of parameters in the test with periodic shear stress loading.
In panel (B), the triggering is plotted in 2D, and can be viewed as the approximate of the overhead shot of panel (A). The time to triggering of the instability is plotted using colored contours. The parameter space below normalized stress of 0.098 permits no triggering of instability until the end of the simulation time duration (800 seconds), which is represented in the black area in both panels. The actual value of time is represented by a close estimate that equals to the number of cycle in which the instability is triggered, multiplied by the period. Above a normalized stress of ~0.13, the triggering of NVT instantaneously occurs in the first cycle of the periodic shear stress loading, which is represented in the blue area for both panels. The contours are color-coded to show the timing of the instability occurs during later cycles of shear stress loading in the range of parameter space where triggering is delayed but still occurs. Note that the time shown in panel (A) on the z-axis is converted to the number of cycle in which the instability was triggered. The conversion helps to highlight the delayed triggering of NVT at small periods. It is worth noting that triggering at the 10th cycle of a 10-second period is not distinguishable from triggering at the 5th cycle of a 20-second period, if the triggering is presented as time in panel (B).

Further, we test the change of seismic rate when we apply periodic shear stress loading. In these models, we apply 6 cycles of the loading instead of a continuous sinusoidal function. In the context of seismic rate, we note that there is always a nonzero seismic rate regardless of rapid triggering of an instability or not. The triggering of NVT becomes apparent when the seismic rate accelerates rapidly in a short time. We choose to report the total accumulated number of events once the shear stress loading terminates (Figure 4.7; third row). Otherwise, the events would continue to accumulate during the entire simulation. We consider that the increase of the accumulated number of events represents the number of NVT that have been triggered. Our tests apply 2 types of sinusoidal shear stress loading to the analytical solutions (4.9-4.11). In the first case, the shear stress loading is a monochromatic sine wave of 6 cycles (Figure 4.7; top-left panel). In the other case, the shear stress loading is modulated by an envelope to resemble a teleseismic wave (Figure 4.7; top-right panel). Compared to the monochromatic result, the envelope modulation of the shape of the sinusoidal stress loading hinders nucleation of NVT (Figure 4.7; third row). This effect is due to the fact that only the central cycles contribute similar level of shear stress loading as the shear stress loading from the monochromatic case. The seismic rate increase seems mostly proportional to the amplitude of shear stress loading. However, the envelope modulated stress loading induced seismic rate increases that are not symmetric over the duration of the loading. This pattern presents the nonlinearity in the solution of seismic rate in rate-and-state friction. The overall accumulated events induced by the monochromatic stress loading is

3 times more than that induced by stress loading with envelope modulation (Figure 4.7; third row).

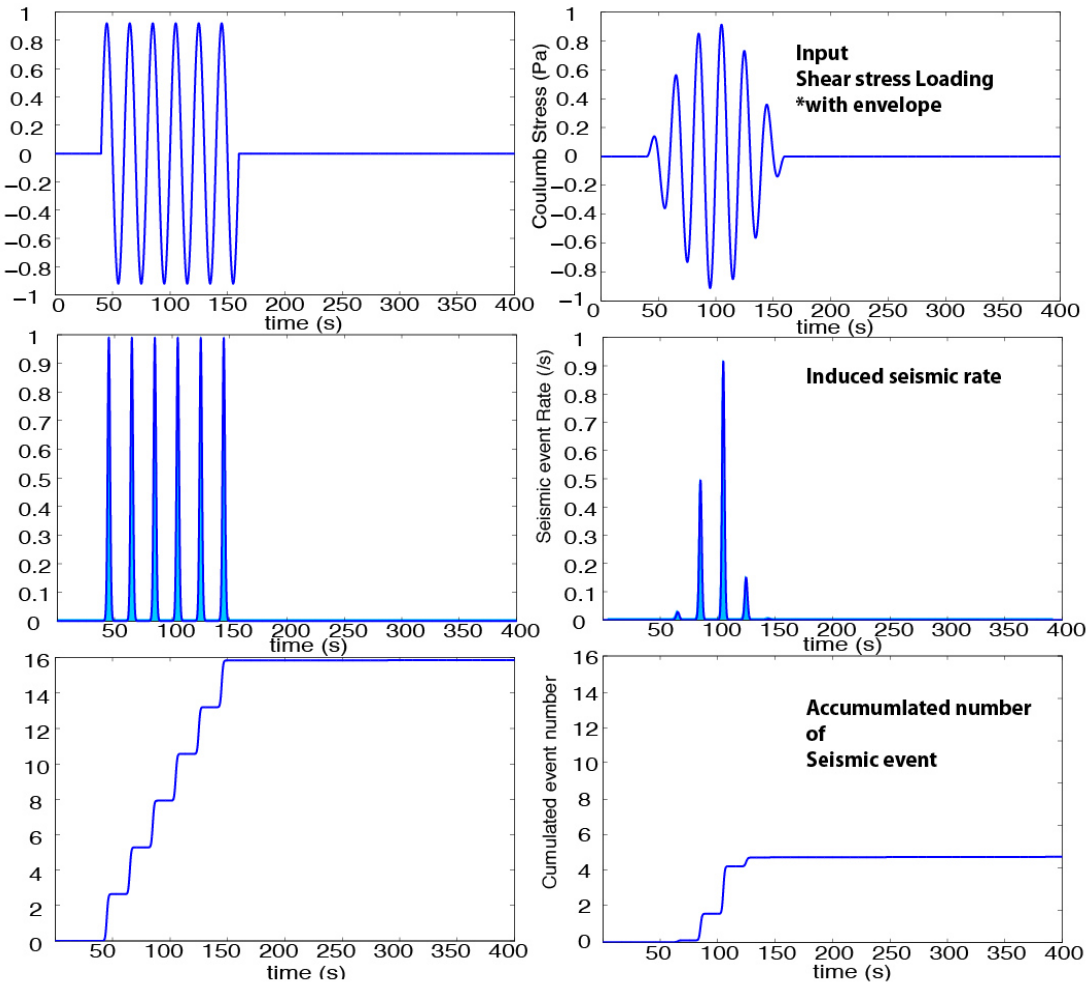

Figure 4.7 Demonstration of results from two tests that the change of seismic rate are induced by external envelope-modulated and monochromatic shear stress loading.
The plots on the left column show the results of the sinusoidal loading without modulation. The plots on the right column show the results of the loading with enveloped modulated shape. The plots in the first row of both columns show the loading history in shear stress (in kPa). Note that the peak amplitudes are 0.92 in this specific case. The plots in the second row of both columns show the seismic rates induced by the loading of shear stress in the first row. The plots in the third row of both columns show the accumulated number of events. The ultimate accumulated number of events are calculated from the area below the curve of the seismic rate (light blue, second row), which is in consequence of the integral of the seismic rate along time. The background normal stress in both cases are 6 kPa. The background seismic rate in both cases are 1.1574 /day.

Then, we investigate the effect of period based on the total number of events. We find that the total number of NVT increases linearly as the period increases (Figure 4.9). We demonstrate this pattern using a test with the same background parameters (normal stress, 6 kPa, and seismic rate, 1.1574/day), using monochromatic loading (same peak amplitude with Figure 4.7, second column) with 3 different periods, 10, 30 and 50 seconds. We see that in an example Figure 4.10, the 10-second-period monochromatic loading induces 7.93 NVTs (red curve). When we triple the period of the monochromatic wave, the loading induces triple of 7.93, 23.75 NVTs (blue curve). Likewise, when we increase 5 times the period of the monochromatic wave, the loading induces 5 times of 7.93, 39.55 NVTs (blue curve). The accumulated number of events in the simulations are not integer because these values are integrated from the seismic rates with respect to time. This representation of the number of event is close to a representation in probability. The normalized stress of this test is 0.153. In this range of normalized stress, the triggering of NVT spontaneously occurs, and the first triggering mostly occurs in the first cycle. If we refer to what is suggested by our previous test (Figure 4.6), this pattern is similar to the results based on the time to instability. The number of triggered events simply increase linearly with the increase of period, because triggering of NVT occurs almost spontaneously in response to each cycle of the external loading. This result indicates consistency between the analytical solution of the seismic rate, and the solution of the slip rate.

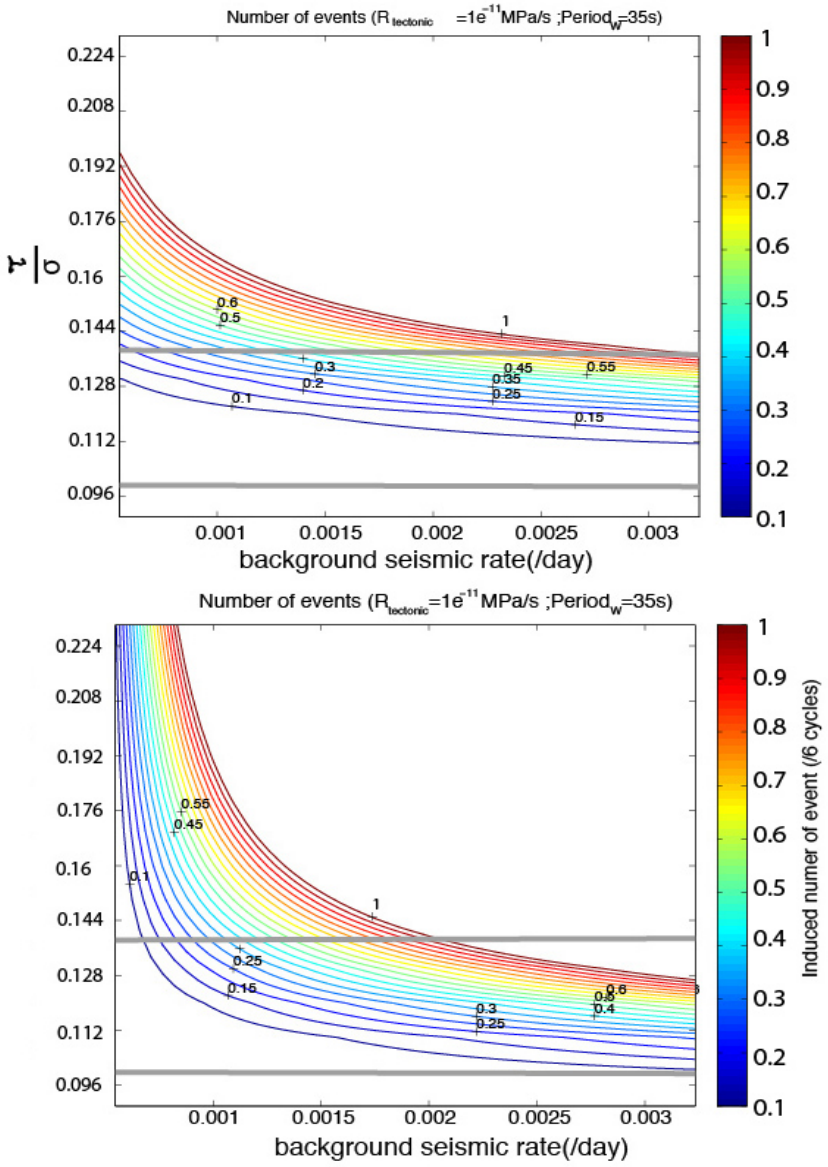

Figure 4.8 The composite test results of induced number of event using both type of stress loadings.

The upper panel shows the case in which stress loading is envelope-modulated, and the lower panel shows the case without envelope modulation. In this case, the variables are the background seismic rate (per day) and the normalized stress (relative peak amplitude of the shear stress to background normal stress). The numbers of NVTs induced by the 6 cycle loadings are plotted as colored contours. Note that the trends of the contour lines are different solely due to the difference on the shear stress loadings. The vertical axis corresponds to a normalized stress that is the peak amplitude of the shear stress loading divided by background.

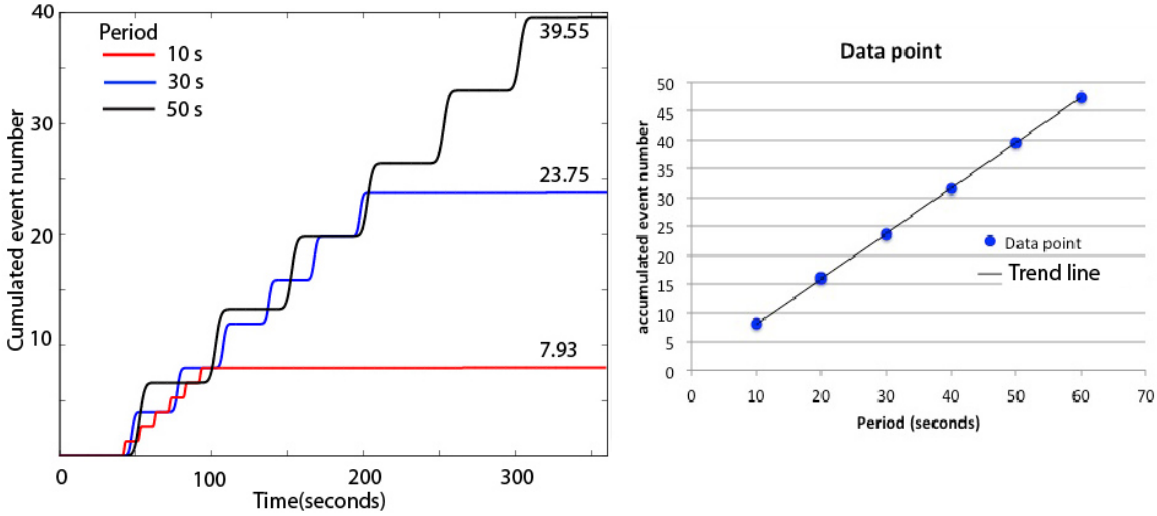

Figure 4.9 The accumulated number of events with monochromatic shear stress loading of 3 different periods.
The background normal stresses in all three cases are 6 kPa. The peak amplitude of the monochromatic loadings are all 0.92 kPa. The background seismic rate in both cases are 1.1574 /day. The left panel shows the cumulated event numbers increase with respect to time in the simulations with different periods. The right panel shows the final values of accumulated event number against the value of period used in the simulations. The ultimate accumulated number of events linearly increase with increase of period. The linear increase pattern is observed when normalized stress is beyond ~0.13, which is 0.153 in this case.

4.3.3 NVT Triggering by Teleseismic Stress Change

In the next level of tests, we apply the estimated shear stress loading from 44 large (M_w >=7.0) earthquakes measured at the Anza region using the analytical model. This set of tests is designed to search for constraints on the background stresses and tremor rate of the Anza region along the SJF. In the set of tests solving slip rates (equation 4.12-4.14), we check whether triggering occurs given the values of background normal stress and background tremor rate. The result is plotted in Figure 4.10. In Figure 4.10(A), the shear stress loading due to teleseismic surface wave from the Denali

earthquake was applied. We tested background normal stress in the range of 50-700 kPa. The amplitude of the shear stress loading at each time step is retrieved from the record of the 44 large teleseismic earthquakes (as used in Chapter 2). However, the 42 earthquakes, except for the 2002 Denali earthquake and 2009 Gulf of California earthquake induced low shear stresses that do not contribute information constraining the background normal stress or tremor rate. The shear stress loadings of the Denali earthquake (Figure 4.10(A)) and the Gulf of California earthquake (Figure 4.10(B)) provide amplitudes large enough that confining the background physical conditions is possible in this test. In both (A) and (B), we mark the asterisk red if no triggering of instability occurs during the entire shear stress loading. That is, the slip rate never exceeds 10^{-3} m/s. We mark the asterisk green if ever the triggering occurs, regardless of the actual timing during the entire shear stress loading. In Figure 4.10(A), we see that the boundary between triggering or no-triggering lies around background normal stress of 500-600 kPa, for each background seismic rate. In Figure 4.10(B), we see that the boundary between triggering or no-triggering lies around background normal stress of 400-500 kPa. Given the fact that 2002 Denali earthquake had triggered NVT and Gulf of California earthquake had triggered none, an intersection which contains all parameter sets satisfying the fact can be found. We overlay (A) and (B) to find the intersection, the green zone in Figure 4.10(C). In this green zone, the range of background seismic rate and background normal stress permits only the triggering of NVT by the shear stress loading of 2002 Denali earthquake, but no triggering by the 2009 Gulf of California earthquake. We find that this intersection provides constraint to the background normal stress (~400-700 kPa) with any given

background seismic rate. However, there seems to be little constraint for background seismic rate. Based on the range of background seismic rate we tested, further extrapolation of the seismic rate to a higher value would also fail to confine any boundary to the seismic rate. This result suggests that the background normal stress on the source of NVT in Anza section of SJF may well be ~400-700 kPa. If we know the background rate of NVT, the background normal stress can even be estimated in a smaller range.

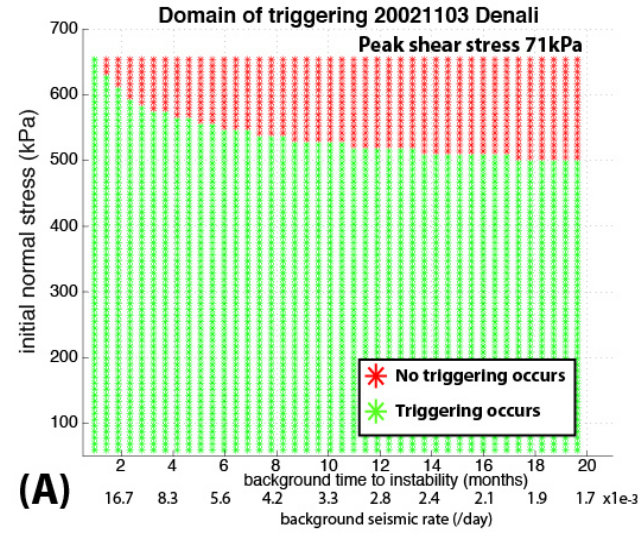
Domain of triggering 20021103 Denali
Peak shear stress 71kPa
initial normal stress (kPa)
700
600
500
400
300
200
100
No triggering occurs
Triggering occurs
2 4 6 8 10 12 14 16 18 20
background time to instability (months)
16.7 8.3 5.6 4.2 3.3 2.8 2.4 2.1 1.9 1.7 x1e-3
background seismic rate (/day)
(A)

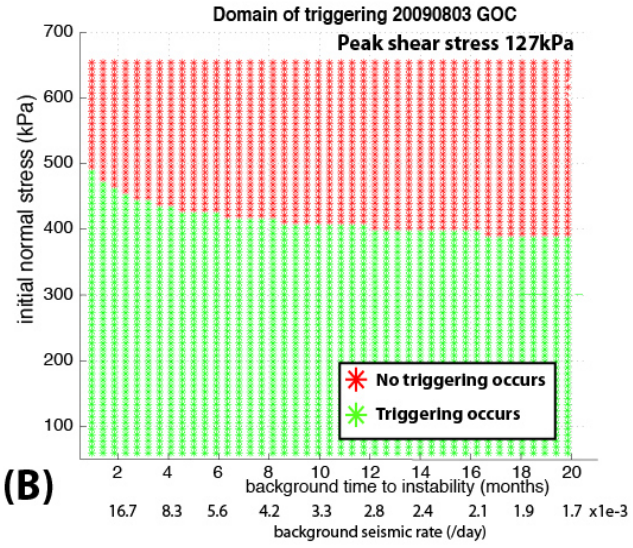
Domain of triggering 20090803 GOC
Peak shear stress 127kPa
initial normal stress (kPa)
700
600
500
400
300
200
100
No triggering occurs
Triggering occurs
2 4 6 8 10 12 14 16 18 20
background time to instability (months)
16.7 8.3 5.6 4.2 3.3 2.8 2.4 2.1 1.9 1.7 x1e-3
background seismic rate (/day)
(B)

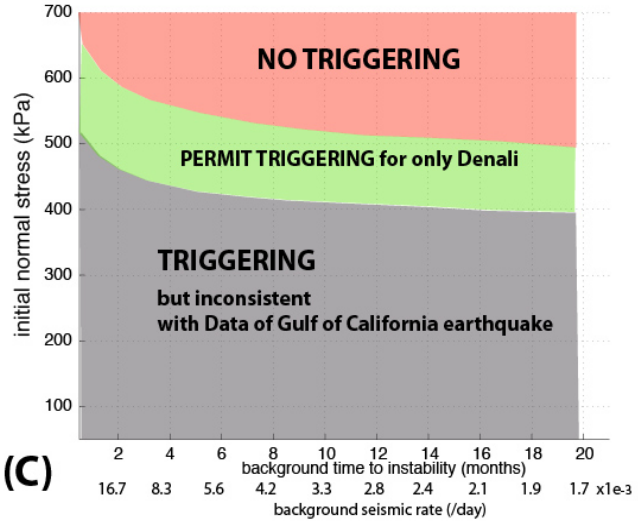
NO TRIGGERING
PERMIT TRIGGERING for only Denali
TRIGGERING
but inconsistent
with Data of Gulf of California earthquake
initial normal stress (kPa)
700
600
500
400
300
200
100
2 4 6 8 10 12 14 16 18 20
background time to instability (months)
16.7 8.3 5.6 4.2 3.3 2.8 2.4 2.1 1.9 1.7 x1e-3
background seismic rate (/day)
(C)

Figure 4.10 The triggering of instability based on shear stress loadings by the 2002 Denali earthquake and 2009 Gulf of California earthquake.
The triggering results are plotted with respect to the parameter space of background seismic rate and background normal stress. In panel (A) and (B), the red asterisks indicate no triggering of instability occurs during the entire shear stress loading. The green asterisk indicates the triggering of instability does occur regardless of the actual timing during the entire shear stress loading. In (A), the shear stress loading by the 2002 Denali earthquake is applied. The peak shear stress is 71 kPa. In (B), the shear stress loading by the 2009 Gulf of California earthquake is applied. The peak shear stress is 127 kPa. In C), we overlaid (A) and (B) to determine a parameter space of background normal stress and background seismic rate, which would be consistent with the triggering of NVT in both records. The green zone indicates the parameter space that permits only triggering of NVT by the Denali earthquake. This zone of parameters matches the actual instance of triggering of NVT.

Similarly, we simulate the accumulated number of events, and examine if these number matches the number of NVTs that are triggered in the true record (e.g. Figure 4.10). We change the background normal stress and the background seismic rate one at a time, apply the shear stress loading, and run each simulation. When we use the true record of shear stress loadings from teleseismic earthquakes, the peak amplitudes of the shear stress loading are known values. As a consequence, the normalized stress used previously can now be changed according to the background normal stresses. We record the number of accumulated number of events both for the shear stress loading record of Denali earthquake and Gulf of California earthquake. In Figure 4.11, we find that solving the accumulated number of events induced by the two shear stress loadings constrain neither background normal stress, nor the background seismic rate. We explore the background seismic rate in a broad range and examine the corresponding induced number of NVT. Through multiple tests, we find that the N=12 accumulated number of event (black curve) span the range of background seismic rate and normalized stress, which can be best illustrated in the upper panel of Figure 4.11. We see that the black curve in the upper panel is above the colored contours. The colored contours represent the induced number of NVT by Gulf of California, which should be fairly close to zero since no NVT was triggered. We see that the colored contours stay flat across most of the range of background seismic rate we explored. At the higher end of the background seismic rate, we did not find any constraint on the background seismic rate, at least at the rate of 1/day. Nonetheless, the background seismic (or NVT, in this context) rate in Anza region is hardly higher than 1/day. It is provided that we observed only 12 triggered NVTs during

44 large teleseismic earthquake records, for at most 88 hours in the Anza region. This induced seismic rate is equivalent to ~=0.0057/day. A background seismic rate much higher than this value is unrealistic.

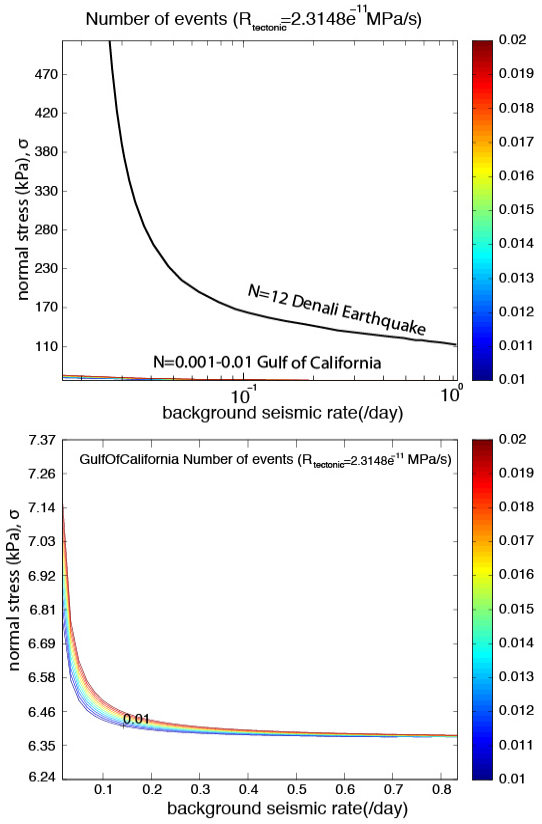

Figure 4.12 The induced number of events produced by the shear stress loading of the 2002 Denali earthquake and 2009 Gulf of California earthquake.
The parameter space are background normal stress (vertical axis) and seismic rate (horizontal axis). The top panel overlays two results of the induced number of events. The black curve shows the 12 triggered NVT induced by the shear stress loading from Denali earthquake. The colored contours show the small values of triggered NVT induced by the shear stress loading from Gulf of California earthquake. Note that the horizontal axis is in log scale. In the top panel, the horizontal axis is plotted in log-scale in order to show a wide span of the background seismic rate. Hence, the curvature of the black line around 0.03 can be better illustrated on log-scale. The low value contours (0.01-0.02/800 seconds) are shown to demonstrate the insignificant potential for triggering of NVT, which can be thought of as no triggering of NVT. In the lower panel, a zoom-in section of the top panel with lower value of background normal stress is provided. Note that the horizontal axis is linear in this case. This plot is to illustrate the detail of the small accumulated number of events, which represents the hardly triggered NVT in the case that the shear stress loading is from 2009 Gulf of California earthquake.

4.4 Discussions

4.4.1 Triggering Simulation

The analytical solutions of rate-and-state friction have important implications based on the simulation of the triggering of NVT. We demonstrate in our study how the the amplitude and period of the external shear stress loading and the background conditions affect the triggering process. We find that the triggering of NVT depends mainly on the relative strength of external loading to the background normal stress. It depends only mildly on the period of the external stress loading. Delayed triggering of NVT is especially prominent at low periods (10-40 s). This triggering pattern makes qualitative rather than quantitative predictions for the triggering phenomena in reality, where the true records of shear stress loading from seismic waves have varying periods and amplitudes overtime. Trugman et al. (2012) also uses a similar idea of analyzing triggering characteristics of the NVT with their model (described in section 4.1.4). Our results show a pattern similar to theirs. They also presented ranges in the parameter space for no triggering, delayed triggering, and instantaneous triggering of the NVT. The boundaries of these ranges (0.8-1) claimed by Trugman et al. (2012) are slightly different from what the normalized stress (0.098-0.13) suggested in our study. It is because that they use yield stress (in terms of force in their study) to normalize the shear stress (in terms of force) change, and thereby leads into the difference on the number. We have no information on the value of the yield stress used in their system, therefore we can not make a quantitative comparison. However, both their results and ours show qualitative similarity in triggering characteristics. The overall pattern in the triggering characteristics

presented by us and Trugman et al. (2012) are quite consistent. However, there is more complexity in the timing of triggering in our model due to different periods of the external shear stress loading, which is not explored by Trugman et al. (2012). This complexity on the triggering of NVT becomes more prominent when we change the shape of the external shear stress loading (discussed in section 4.4.2 and 4.4.3).

The amplitude of the external stress loading represents the strength of the external force promoting triggering of an instability on the fault. However, the amplitude of the background normal stress represents clamping on the fault which prevents the asperity from failing. The relative ratio between them, the normalized stress used in our simulation, determines the effective strength from the external stress loading, which is the dominant parameter in most of our simulations. The normalized stress also acts as a parameter that collectively describes the effect of external force and the intrinsic fault characteristics. This parameter explains that the effect of external loading cannot be independently considered apart from the intrinsic characteristics on the fault in the triggering problem. The reported shear stress change, or PGV thresholds, required for the triggering of NVT, differ among different regions or on different faults (Nadeau and Guilhem, 2009; Chao et al., 2011; Chao and Peng, 2012; Peng et al., 2013; Wang et al., 2013; Fuchs et al., 2014). It becomes evident that the differences in the shear stress threshold at different locations may well be natural. The differences in the shear stress threshold imply different background normal stresses on the fault. In addition, based on our results, triggering of NVT occurs for the normalized stress of 0.098 and above. We can impose an upper bound to the background normal stress, provided the shear stress

threshold in each location along with this limit. It suggests that locations with high shear stress threshold can be explained by high background (effective) normal stress. With the higher effective normal stress, the effect of pore-fluid on the fault could be mild, or that the pore-pressure could be far from lithostatic.

The background seismic rate used in our model represents another intrinsic characteristic of the fault. It can be considered how susceptible the fault may be to tectonic loading, independent of any transient stress perturbation. Although we have no constraint on this variable in most of our simulation, this parameter can be considered inversely proportional to the fault strength, characterized by the fault zone material. For example, pulverized gouge makes the fault weak (Lockner et al., 2010; Carpenter et al., 2010), or hydrothermal cohesion with pore-fluid cementing the microfractures makes the fault strong (Tenthorey et al., 2006). Fortunately, no matter what is the cause that alters the fault strength, the resulting background seismic rate (or NVT rate in this context) is measurable. By excluding periods affected by external stress perturbations (e.g. from earthquakes, tides or artificial noise), detecting NVT numbers during a time span would provide us some idea of the range for background seismic rate. With information on the background seismic rate, we can narrow down the range of parameters for normalized stress. Combined with the data of the triggering of NVT, we can at least constrain the background normal stress on the particular asperity. This method does not provide exact numbers, but it provides reasonable estimates on the ranges of the background normal stress.

Our study also demonstrates a method to confine the range of background normal stress and the background seismic rate, given several records of shear stress loading from the external sources, some of which trigger NVT, and others do not at the same location. With available data like in section 4.3.4, we can find the intersection in the parameter space that satisfies the triggering and no-triggering incidences. In the current study, we have two teleseismic records that contribute to confine our parameters, and we find constraint on only the background normal stress. If more triggering incidences are available, it may be possible to further confine the background normal stress or seismic rate to a smaller range. This method is widely applicable to other regions, as long as several incidences of triggered NVT are present.

4.4.2 Triggering Characteristics in Reality

When the shear stress loading consists of simplified monochromatic sine waves, our results suggest a boundary of normalized stress (0.098) above which the triggering of NVT is essentially guaranteed to occur. The minimum shear stress required for triggering in the Anza region along SJF is reported to be 17-35 kPa (Chapter 2). From these observations, in terms of a monochromatic sine wave with shear stress amplitude of 17 kPa, the upper bound for background normal stress in Anza is suggested to be 173 kPa. Conversely, in reality, the range of background normal stress constrained by the record of shear stress loading, from 2002 Denali and 2009 Gulf of California earthquake, is between ~400-700 kPa. The background normal stress suggested from real data is significantly larger than the 173 kPa suggested by our modeling. We find that in reality the shear stress loadings seem more powerful to trigger NVT compared to the case when

the external loading is monochromatic. It is less likely that this mismatch of background normal stress is due to the difference in background seismic(tremor) rate. We do not have constraints on background seismic rate, based on multiple simulations. Most important of all, we do not find the triggering threshold sensitive to background seismic rate (Figure 4.10). Generally, above a small range of normal stress, the NVT is determined to be triggered. The strength of the triggering wave may change dramatically if the shape is modulated to be a wave packet, instead of simple monochromatic function. We see this effect in Figure 4.7, comparing the triggered number of events between an external loading of monochromatic sine function and an envelope-modulated sinusoidal function. We do not analyze this complexity because it is beyond the scope of this study. However, this effect appears to change significantly the triggering characteristics from that of a simple case. The potential of triggering of NVT by a true shear stress loading is hardly predictable because of the complexity of the shape of the external loading. It would be a crucial future work to be analyzed systematically. However, we can always forwardly simulate the boundary between triggering and non-triggering of NVT (e.g. Figure 4.10 (C)), on the parameter space of background normal stress and seismic rate. Our study demonstrates a method to provide a conclusive result regardless of how the shape of waveform changes the triggering characteristics.

4.4.3 Constraints on Background Physical Conditions

Through our simulation test applying the true shear stress loadings, we find a constraint on background normal stress (~400-700 kPa) for the Anza region along SJF. This is a clear demonstration of how the background conditions can be constrained

through the use of our method and several true records of shear stress loadings. The range of background normal stress is low relative to that on the source of earthquakes. However, few studies have estimated the actual value of background normal stress on the source of NVT. Most of the observational studies infer pore-fluid on the source of NVT to explain low effective normal stress, but rarely estimate the value of the low effective normal stress. Johnson et al (2013) used a single-degree-of-freedom spring-slider model and Markov chain Monte Carlo inversion techniques to solve for friction parameters that reproduce the observed transient creep and tremor. This is the only study in the literature which had constrained on the background normal stress and associated simulation on tremor. They simulate the tremor activity before and after 2003 M6.5 San Semion earthquake successfully with an upper bound of background normal stress of ~1 MPa. Our estimated range for background normal stress is an order lower than 1MPa. However, the nominal friction coefficient used in Johnson et al. (2013) is 0.2, much smaller than the 0.6, typical value, we used in our simulations.

4.5 Conclusions

In this study, we analyze the effects introduced by the external shear stress loadings and the effects of the background conditions in the triggering process, using analytical solutions of rate-and-state friction. We incorporate most current estimates of the physical conditions, including background normal stress, amplitude of shear stress change, constitutive friction coefficient and other constitutive rate-and-state parameters, to our model fault. We first apply a monochromatic external shear stress loading. In the case of simple loading, we find that the relative strength of the shear stress loading to the

background normal stress, called normalized stress, mainly controls the triggering characteristics of NVT. The period of the external stress loading has a mild effect to the timing of the triggering process, which is more prominent in the short periods (10-40 s). The triggering of NVT ceases below normalized stress of 0.098. Between normalized stress of 0.098-0.13, triggering of NVT may be delayed to later cycles. Above normalized stress of 0.13, NVT is spontaneously triggered. We also test an envelope modulation to the monochromatic function and find it hinders triggered NVT. We then apply the true shear stress loadings induced by 44 large (M_w >=7.0) teleseismic earthquakes. Specifically, the records of 2002 Denali and 2009 Gulf of California earthquakes help us constrain background normal stress in the range of ~400-700 kPa. This range of background normal stress suggests consistent idea with the general understanding of a low effective normal stress on the source of NVT. We demonstrate how this method can provide some estimates to the physical stress conditions on the fault where NVT is triggered.

Chapter 5 Conclusions

5.1 Summary

The triggering of NVT first gained its attraction from the worldwide surge of the search for NVT, including ambient or triggered NVT, a newly discovered seismic signal different from earthquakes. We learn from observations that NVT is special compared to typical earthquakes owing to the physical conditions, including background stresses and frictional regimes, on the source of NVT, which are different from that of the earthquakes. Whether the triggering of NVT on specific portions of a fault would reflect such distinctions of the physical conditions remains controversial. Scientists devote tremendous efforts to understand the triggering mechanism, as well as the source mechanism of NVT. This is an ongoing process, and much more details are left to be explored. I dedicated to better understand the triggering process of NVT. The question can be break down into two main parts, albeit with some aspects of them are still inter-related. The first part is the external stress perturbation, commonly known as the triggering wave. The second part is the background physical conditions on the fault including the stress state and the frictional regime. I investigate these two parts with two observational studies and one numerical analysis. The observational studies report the triggering of NVT at Anza along the SJF, and near Cholame along the SAF. The numerical analysis explains the basic features of the triggering process of NVT, using the slip rate and seismic rate solutions from the rate-and-state constitutive law.

In the first case, the remote triggering of NVT by earthquakes, I examine the shear stress loading induced by 44 teleseismic earthquake records (M_w >=7.0). I

investigate the peak shear stress induced at the surface stations and constrain the minimum value required for triggering of NVT in Anza region along SJF. We found that the threshold of peak shear stress is 17-35 kPa. I observed only 1 incidence of triggered tremor by 2002 Denali earthquake, out of 44 teleseismic earthquake. In addition, the 2009 Gulf of California earthquake induced particularly high surface strain but did not trigger any NVT. With this set of observation, the NVT in the Anza region along SJF is considered infrequent, relative to other well-developed strike-slip faults like the SAF.

I utilized the BBP method developed by Ghosh et al. (2012) to examine the triggering of NVT near Cholame along the SJF. The BBP method provides enhanced detection power for weak amplitude signals, especially suitable for the detection of tremor. We implement this method using a designed array ~10 km west of SAF. We found that in 11 earthquakes with peak shear stress range 0.07-4.5 kPa, 7 of them had rate of NVT increase 2 times or above after the first arrival of the major events. The measurement is made in 1 hours before, during and 1 hours after each major earthquake signals. The corresponding peak shear stresses of these earthquakes suggest a minimum threshold of ~0.25 kPa for the triggering of NVT in this region. This minimum threshold is relatively low compared with what reported previously for the Parkfield-Cholame section of SAF. The reduction of the threshold may support the weak fault scenario on the SAF, which has been well suggested by both the SAFOD core sample analysis and the intensively observed creep.

We use an analytical patch model based on rate-and-state friction, which is proved consistent with the dynamic model on a 2D fault using Boundary Integral

Element Method (BIEM; Dunham et al., 2011) coded by Eric Dunham (Dunham et al., 2011). We simulate remote triggering of a slip-instability with the analytical solution of the rate-and-state friction. We first parameterize the stress perturbation of a triggering surface wave as sine wave with fixed period and amplitude. To resemble tremor source, the background stress, source dimensions, and friction coefficients in our model are set based on typical observational estimates and modeling studies. Therefore, we funnel the focus of the analysis to the effect of external loading stresses. We setup the event source on relatively young fault (10 yrs age), common background tectonic loading (.73kPa/yr), but low background normal stress (50-700 kPa) to resemble a tremor source. We find that the model is mildly sensitive to the period of the external loading (10- 70 s), such that varying the period does little effect to change the time to instability. In contrast, the relative amplitude of the shear stress loading to background normal stress strongly controls the time to failure of the patch. The model suggests that, under ratio of 0.098, the patch will not fail given the external loading. There is a small range of ratio (0.098-0.13) in which the triggering is delayed to a later time after the onset of external loading. At loading ratio beyond this point, the patch would always fail.

Then, we use the true teleseismic stressing histories of 44 large ($M_w \geq 7.4$) earthquakes as the external stress loading. Using these records, we explore the background stresses and seismic rate that would reproduce the triggered tremor observations in the case of Anza region along SJF. Constrained by the observations (Chapter1 ; Wang et al. 2013), our model results suggest that the background normal stress may be as low as 500-700 kPa at the tremor sources of Anza. Meanwhile, two

triggering observations in our test, 2002 Denali earthquake and 2009 Gulf of California mainly constrain this number. However, in our model, the background condition of seismicity rate cannot be constrained with the information currently available. Our model helps to demonstrate the corresponding relationship between external loading stresses and tremor triggering, under specific background conditions. In addition, our model provides some constraints of background normal stress, if the triggering stress loading is known.

5.2 Broader Impacts

This dissertation has clarified the factors involved in the triggering of NVT. Mostly, the focus is dedicated to estimate the background stresses and to characterize the effect of the external stress loading. We emphasize the importance of estimating the minimum shear stress required to trigger NVT, with better precision empowered by robust detection methods, such as BBP, or cross-correlation validated by thorough visual inspection. The shear stress threshold at a particular location implies the general strength of the fault, which can be inferred to the fault material and its friction characteristics.

The numerical model we constructed to simulate triggering of NVT jointly incorporates the most current knowledge of the NVT source. Some physical conditions of the source are not investigated in this study due to the complexity and number of parameters involved in the analysis (e.g. the value of rate-and-state frictional parameters, a, b, initial friction coefficient, the state variable, rate-weakening or rate-strengthening on the asperity, and the surrounding frictional regime adjacent to the asperity. These detailed frictional parameters should be tested step-by-step once an overall feature of the

triggering characteristics of NVT is shaped. The friction regime is solely handled by rate-and-state friction with the constitutive parameters arbitrary set. The constitutive parameters are consistent with current estimates used in most numerical models for slow-slip, LFE and creep. However, we do not investigate the effect of the constitutive friction parameters in the triggering of NVT. We focus on analyzing the background stresses on the source of NVT, as well as the effects from the external loading. We successfully find a way to solve for a range of the parameters, which explains whether triggering of NVT occurs, and when triggering of NVT is delayed. This method is applicable to estimate single parameter (e.g. background normal stress) at a source of NVT, when information on other parameters (e.g. period of stress loading, background rate of NVT) is known. It is possible to apply this method in other regions (or to other data), to explore the background physical conditions on the source of NVT. This will be important contribution to our understanding of the source of NVT in different regions.

5.3 Future Works

The BBP method could be used to investigate more data when the data are available. The minimum shear stress threshold can be constrained more accurately if more triggering events are reported. The same goes to the estimation of background rate of NVT. Although background rate of NVT may vary temporally, it is still crucial to obtain background rate of NVT as the reference for individual report of triggering.

In the numerical model, the complexity of the shape of the external loading may lead to significant change to the triggering of NVT. New series of tests carefully designed to analyze such effect should be carried out. Likewise, the constitutive friction regime

also affects the triggering process of NVT. The tests should be introduced by changing the constitutive friction parameters individually (e.g. varying a-b, D_c or the spatial distribution of a-b). Based on the tests we had already performed, the effect of background stresses and external stress loading would be separated more clearly, which enables future tests to solely focus on frictional parameters.

Bibliography

Ader, T. J., J.-P. Ampuero, and J.-P. Avouac (2012), The role of velocity-neutral creep on the modulation of tectonic tremor activity by periodic loading, *Geophys. Res. Lett*., 39, L16310, doi:10.1029/2012GL052326.

Agnew, D. C., and F. K. Wyatt (2014). Dynamic Strains at Regional and Teleseismic Distances. *Bulletin of the Seismological Society of America*, 104(4), 1846-1859.

Aguiar, A. C., J. R. Brown, and G. C. Beroza (2009). Non-volcanic tremor near the Calaveras fault triggered by Mw∼8 teleseisms, *Eos Trans. AGU* 90, no. 54 (Fall Meet. Suppl.), Abstract T23E-06.

Aguiar, A. C., T. I. Melbourne, and C. W. Scrivner (2009), Moment release rate of Cascadia tremor constrained by GPS, *J. Geophys. Res*., 114, B00A05, doi:10.1029/2008JB005909.

Ariyoshi, K., T. Hori, J. P. Ampuero, Y. Kaneda, T. Matsuzawa, R. Hino and A. Hasegawa (2009). Influence of interaction between small asperities on various types of slow earthquake in a 3-D simulation for a subduction plate boundary, *Gondwana Research*, 16, 534-544.

Bailey, I. W., Y. Ben-Zion, T. W. Becker, and M. Holschneider (2010). Quantifying Focal Mechanism Heterogeneity for Fault Zones in Central and Southern California, *Geophys. J. Int*., doi: 10.1111/j.1365-246X.2010.04745.x.

Bartlow, N. M., S. Miyazaki, A. M. Bradley, and P. Segall (2011), Space-time correlation of slip and tremor during the 2009 Cascadia slow slip event, *Geophys. Res. Lett*., 38, L18309, doi:10.1029/2011GL048714.

Ben-Zion, Y., and D. J. Andrews (1998). Properties and implications of dynamic rupture along a material interface, *Bull. Seismol. Soc. Am*. 88, no. 4, 1085–1094.

Berteussen, K. A. (1979), The origin of slowness and azimuth anomalies at large arrays, *Bull. Seismol. Soc. Am.*, 66, 719–741.

Blanpied, M. L., D. A. Lockner, and J. D. Byerlee (1991). Fault stability inferred from granite sliding experiments at hydrothermal conditions, *Geophysical Research Letters*, 18, 609-612.

Boatwright, J., J. B. Fletcher and T. E. Fumal (1991). A general inversion scheme for source, site, and propagation characteristics using multiply recorded sets of moderate-sized earthquakes, *Bull. Seismol. Soc. Am*. 81, no. 5, 1754–1782.

Brendan J. M., Y. Klinger and E. A. Hetland (2013). Inference of Multiple Earthquake-Cycle Relaxation Timescales from Irregular Geodetic Sampling of Interseismic Deformation, *Bull. Seismol. Soc. Am*. 103, no. 5, 2824-2835, doi:10.1785/0120130006

Brodsky, E. E., and N. J. Van der Elst (2014). The Uses of Dynamic Earthquake Triggering, *Annual Review of Earth and Planetary Sciences* 42, 317-339, doi: 10.1146/annurev-earth-060313-054648.

Brown, J. R., G. C. Beroza, and D. R. Shelly (2008), An autocorrelation method to detect low frequency earthquakes within tremor, *Geophys. Res. Lett*., 35, L16305, doi:10.1029/2008GL034560.

Brown, J. R. (2010). A catalog of low frequency earthquake activity from triggered tremor on the San Jacinto fault, in *SCEC Annual Meeting*, Palm Springs, California, 11–15 September 2010, Abstract 198.

Brown, K. M., M. D. Tryon, H. R. DeShon, L. M. Dorman, and S. Y. Schwartz (2005). Correlated transient fluid pulsing and seismic tremor in the Costa Rica subduction zone, *Earth Planet Sci. Lett*. 238, nos. 1–2, 189–203.

Brune, J. N. (1970). Tectonic Stress and the Spectra of Seismic Shear Waves from Earthquakes. *Journal of Geophysical Research*, 75(26), 4997-5009.

Courant, R., Friedrichs, K. and Lewy, H. (1928), On the partial difference equations of mathematical physics, *AEC Research and Development Report*, NYO-7689, New York: AEC Computing and Applied Mathematics Centre

Carpenter, B. M., C. Marone, and D. M. Saffer (2011). Weakness of the San Andreas fault revealed by samples from the active fault zone, *Nature Geosci*. 4, no. 4, 251–254.

Chao, K., Z. Peng, C. Wu, C.-C. Tang, and C.-H. Lin (2010). Remote triggering of non-volcanic tremor around Taiwan, *Geophys. J. Int*. 188, no. 1, 301–324.

Chao, K., Z. Peng, A. Fabian, and L. Ojha (2012). Comparisons of triggered tremor in California, *Bull. Seismol. Soc. Am*. 102, no. 2, 900–908.

Chao, K., Z. Peng, H. Gonzalez-Huizar, C. Aiken, B. Enescu, H. Kao, A. A. Velasco, K. Obara and T. Matsuzawa (2013). A Global Search for Triggered Tremor Following the 2011 M_w 9.0 Tohoku Earthquake, *Bull. Seismol. Soc. Am*. 103, no. 2B, 1551–1571.

Crotwell, H. P., T. J. Owens, and J. Ritsema (1999). The TauP ToolKit: Flexible Seismic Travel-Time and Raypath Utilities, *Seismological Research Letters*. 70, no. 2, 154-160.

Dieterich, J. H. (1979). Modeling of rock friction: 2. Simulation of preseismic slip, *Journal of Geophysical Research: Solid Earth*, 84, 2169-2175.

Dieterich, J. H. (1981). Constitutive properties of faults with simulated gouge, Mechanical Behavior of Crustal Rocks, *Geophys. Monogr. Ser*.,24N. L. Carter, et al., 103–120, *AGU*, Washington, D.C., 1981.

Dieterich, J. H. (1987). Nucleation and triggering of earthquake slip: effect of periodic stresses. *Tectonophysics*, 144(1), 127-139.

Dieterich, J. H. (1992). Earthquake nucleation on faults with rate-and state-dependent strength, *Tectonophysics*., 211, 115-134.

Dieterich, J. (1994). A constitutive law for rate of earthquake production and its application to earthquake clustering. *Journal of Geophysical Research: Solid Earth* 99(B2), 2601-2618.

Dieterich, J. H. and B. D. Kilgore. (1996). Imaging surface contacts: power law contact distributions and contact stresses in quartz, calcite, glass and acrylic plastic. *Tectonophysics*, 256(1), 219-239.

Dieterich, J. H. (2007). 4.04—Applications of rate-and state-dependent friction to models of fault slip and earthquake occurrence, *Treatise on Geophysics*, 107-129.

Dunham, E. M., D. Belanger, L. Cong and J. E. Kozdon (2011). Earthquake Ruptures with Strongly Rate-Weakening Friction and Off-Fault Plasticity, Part 1: Planar Faults, *Bull. Seismol. Soc. Am*. 101, no. 5, 2296–2307.

Fletcher, J. B., and A. McGarr (2011), Moments, magnitudes, and radiated energies of non-volcanic tremor near Cholame, CA, from ground motion spectra at UPSAR, *Geophys. Res. Lett*., 38, L16314, doi:10.1029/2011GL048636.

Fry, B., K. Chao, S. Bannister, Z. Peng, and L. Wallace (2011), Deep tremor in New Zealand triggered by the 2010 Mw8.8 Chile earthquake, *Geophys. Res. Lett*., 38, L15306, doi:10.1029/2011GL048319.

Fuchs, F., M. Lupi, and S. A. Miller (2014), Remotely triggered nonvolcanic tremor in Sumbawa, Indonesia. *Geophysical Research Letters*, 41(12), 4185-4193.

George, A. D., J. Markwell, and R. Fogarty (2000), Real-time sonar beamforming on high-performance distributed computers. *Parallel Computing*, 26(10), 1231-1252.

Gershenzon N.I., Bykov V. G. and Bambakidis G., (2009), Strain waves, earthquakes, slow earthquakes, and afterslip in the framework of the Frenkel-Kontorova model, *Physical Review E* 79, 056601

Gershenzon N.I., G. Bambakidis, E. Hauser, A. Ghosh, K.C. Creager (2011) Episodic tremors and slip in Cascadia in the framework of the Frenkel-Kontorova model. *Geophys. Res. Lett*., 38, L01309, doi:10.1029/2010GL045225

Ghosh, A., J. E. Vidale, J. R. Sweet, K. C. Creager, and A. G. Wech (2009), Tremor patches in Cascadia revealed by seismic array analysis, *Geophys. Res. Lett*., 36, L17316, doi:10.1029/2009GL039080.

Ghosh, A., J. E. Vidale, J. R. Sweet, K. C. Creager, A. G. Wech, H. Houston, and E. E. Brodsky (2010), Rapid, continuous streaking of tremor in Cascadia, Geochem. *Geophys. Geosyst*., 11, Q12010, doi:10.1029/2010GC003305.

Ghosh, A., J. E. Vidale, and K. C. Creager (2012), Tremor asperities in the transition zone control evolution of slow earthquakes, *J. Geophys. Res*., 117, B10301, doi:10.1029/2012JB009249.

Gomberg, J., and D. Agnew (1996). The accuracy of seismic estimates of dynamic strains: An evaluation using strainmeter and seismometer data from Piñon Flat observatory, California, *Bull. Seismol. Soc. Am*. 86, no. 1A, 212–220.

Gomberg, J., P. Bodin, and P. A. Reasenberg (2003). Observing earthquakes triggered in the near field by dynamic deformations, *Bull. Seismol. Soc. Am*. 93, 118–138.

Gomberg, J., and P. Johnson (2005). Seismology: Dynamic triggering of earthquakes, *Nature* 437, no. 7060, 830–830.

Gomberg, J., J. L. Rubinstein, Z. Peng, K. C. Creager, J. E. Vidale, and P. Bodin (2008). Widespread triggering of nonvolcanic tremor in California, *Science* 319, 173.

Gomberg, J. (2010), Lessons from (triggered) tremor, J. Geophys. Res., 115, B10302, doi:10.1029/2009JB007011.

Gonzalez-Huizar, H., A. A. Velasco, Z. Peng, and R. Castro (2012). Remote triggered seismicity caused by the 2011, M 9.0 Tohoku-Oki, Japan earthquake, *Geophys. Res. Lett*. 39, doi: 10.1029/2012GL051015.

Gu, J. C., J. R. Rice, A. L. Ruina, and S. T. Tse (1984). Slip motion and stability of a single degree of freedom elastic system with rate and state dependent friction, *Journal of the Mechanics and Physics of Solids*., 32, 167-196.

Gu, J. C. (1984). Frictional resistance to accelerating slip, *Pure and Applied Geophysics PAGEOPH*,. 122, 662-679.

Guilhem, A., Z. Peng, and R. M. Nadeau (2010). High-frequency identification of non-volcanic tremor triggered by regional earthquakes, *Geophys. Res. Lett*., 37, L16309, doi:10.1029/2010GL044660.

Hartse, H. E., M. C. Fehler, R. C. Aster, J. S. Scott, and F. L. Vernon (1994). Small-scale stress heterogeneity in the Anza seismic gap, southern California, *J. Geophys. Res*. 99, no. B4, 6801–6818.

Heaton, T. H., and D. V. Helmberger (1977). A study of the strong ground motion of the Borrego Mountain, California earthquake, *Bull. Seismol. Soc. Am*. 67, no. 2, 315–330.

Hill, D. P. (2008). Dynamic stresses, Coulomb failure, and remote triggering, *Bull. Seismol. Soc. Am*. 98, no. 1, 66–92.

Hill, D. P. (2010). Surface-Wave Potential for Triggering Tectonic (Nonvolcanic) Tremor, *Bull. Seismol. Soc. Am*. 100, no. 5A, 1859–1878.

Hill, D. P. (2012a). Dynamic stresses, Coulomb failure, and remote triggering — Corrected, *Bull. Seismol. Soc. Am*. 102, no. 6, 2313–2336.

Hill, D. P. (2012b). Surface-wave potential for triggering tectonic (nonvolcanic) tremor corrected, *Bull. Seismol. Soc. Am*. 102, no. 6, 2337–2355.

Hill, D. P., Z. Peng, D. R. Shelly, and C. Aiken (2013). S-wave triggering of tremor beneath the Parkfield, CA, section of the San Andreas fault by the 2011 Tohoku Japan earthquake: Observations and theory, *Bull. Seismol. Soc. Am*. 103, no. 2B, 1541–1550.

Hill, D. P., P. A. Reasenberg, A. Michael, W. J. Arabaz, G. Beroza, D. Brumbaugh, J. N. Brune, R. Castro, S. Davis, D. dePolo, W. L. Ellsworth, J. Gomberg, S. Harmsen, L. House, S. M. Jackson, M. J. S. Johnston, L. Jones, R. Keller, S. Malone, L. Munguia, S. Nava, J. C. Pechmann, A. Sanford, R.W. Simpson, R. B. Smith, M. Stark, M. Stickney, A. Vidal, S. Walter, V. Wong, and J. Zollweg (1993). Seismicity remotely triggered by the magnitude 7.3 Landers, California earthquake, *Science* 260, 1617–1622.

Hong, Tae-Kyung, and William Menke (2006) Tomographic investigation of the wear along the San Jacinto fault, southern California. *Physics of the earth and Planetary Interiors* 155.3: 236-248.

Husebye, E. S, and B. O. Ruud (1989) Array seismology—Past, present and future developments, in *Observatory Seismology*, edited by J. J. Litehiser, pp. 123–153, Univ. of Calif Press, Berkeley, 1989.

Houston, H., B.G. Delbridge, A. G. Wech and K. C. Creager (2011). Rapid tremor reversals in Cascadia generated by a weakened plate interface, *Nature Geoscience* 4, 404–409.

Ide, S., D. R. Shelly, and G. C. Beroza (2007). Mechanism of deep low frequency earthquakes : Further evidence that deep non-volcanic tremor is generated by shear slip on the plate interface, *Geophys. Res. Lett*. 34, L03308, doi: 10.1029/2006GL028890.

Ide, S. (2008), A Brownian walk model for slow earthquakes, *Geophys. Res. Lett*., 35, L17301, doi:10.1029/2008GL034821.

Ito, Y., K. Obara, K. Shiomi, S. Sekine, and H. Hirose (2007). Slow earthquakes coincident with episodic tremors and slow slip events, *Science* 315, 503–506.

Ito, Y., K. Obara, T. Matsuzawa, and T. Maeda (2009), Very low frequency earthquakes related to small asperities on the plate boundary interface at the locked to aseismic transition, *J. Geophys. Res*., 114, B00A13, doi:10.1029/2008JB006036.

Johnson, P. A., and X. Jia (2005). Nonlinear dynamics, granular media and dynamic earthquake triggering, *Nature* 437, 871-874.

Johanson, I. Anne (2006) Slip characteristics of San Andreas Fault transition zone segments*, Ph.D. Thesis, University of California, Berkeley*.

Kanamori, H. (1980). The state of stress in the Earth's lithosphere, in *Physics of the Earth's Interior*, A. M. Dziewonski and E. Boschi (Editors), Soc. Italiana di Fisica, North-Holland Pub. Co., Amsterdam, 531–554.

Kendrick, K. J., D. M. Morton, S. G. Wells, and R. W. Simpson (2002). Spatial and temporal deformation along the northern San Jacinto fault, southern California: Implications for slip rates, *Bull. Seismol. Soc. Am*. 92, no. 7, 2782–2802.

Kilb, D., J. Gomberg and P. Bodin (2000). Triggering of earthquake aftershocks by dynamic stresses, *Nature* 408, 570-574.

Liu, Y., and J. R. Rice (2005), Aseismic slip transients emerge spontaneously in three-dimensional rate and state modeling of subduction earthquake sequences, *J. Geophys. Res*., 110, B08307, doi:10.1029/2004JB003424.

Lehne, P.H. and M. Pettersen, (1999) An Overview of Smart Antenna Technology

for Mobile Communications Systems, *IEEE Communications Surveys*, Vol. 2, no. 4, pp. 2–13, Fourth Quarter 1999.

Lockner, D. A., C. Morrow, D. Moore and S. Hickman (2011). Low strength of deep San Andreas fault gouge from SAFOD core, *Nature* 472, 82-85.

Louie, J.N., C.R. Allen, D.C. Johnson, P.C. Haase, and S.N. Cohn (1985). Fault slip in southern California, *Bull. Seis. Soc. Am*. 75, 811–833.

Marone, C. (1998). The effect of loading rate on static friction and the rate of fault healing during the earthquake cycle. *Nature*, 391(6662), 69-72.

Matsuzawa, T., H. Hirose, B. Shibazaki, and K. Obara (2010), Modeling short- and long-term slow slip events in the seismic cycles of large subduction earthquakes, *J. Geophys. Res*., 115, B12301,

Mikumo, T., and K. Aki (1964). Determination of local phase velocity by intercomparison of seismograms from strain and pendulum instruments, *J. Geophys. Res*. 69, no. 4, 721–731.

Miyazawa, M., and J. Mori (2005). Detection of triggered deep lowfrequency events from the 2003 Tokachi-oki earthquake, *Geophys. Res. Lett*. 32, no. 10, L10307, doi: 10.1029/2005GL022539.

Miyazawa, M., and J. Mori (2006). Evidence suggesting fluid flow beneath Japan due to periodic seismic triggering from the 2004 Sumatra–Andaman earthquake, *Geophys. Res. Lett*. 33, no. 5, L05303.

Miyazawa, M., E. E. Brodsky, and J. Mori (2008). Learning from dynamic triggering of low-frequency tremor in subduction zones, *Earth Planets Space* 60, e17–e20.

Miyazawa, M., and E. E. Brodsky (2008). Deep low-frequency tremor that correlates with passing surface waves, *J. Geophys. Res*. 113, no. B1, B01307, doi: 10.1029/2006JB004890.

Nadeau, R. M., and D. Dolenc (2005). Nonvolcanic tremors deep beneath the San Andreas fault, *Science* 307, no. 5708, 389.

Nadeau, R. M., and A. Guilhem (2009). Nonvolcanic Tremor Evolution and the San Simeon and Parkfield, California, Earthquakes, *Science* 325 , 191-193.

Nakata, R., N. Suda and H. Tsuruoka (2008). Non-volcanic tremor resulting from the combined effect of Earth tides and slow slip events, *Nature Geoscience* 1, 676-678.

Neal, S. L., and G. L. Pavlis, Imaging *P*- to *S* conversions with broad-band seismic arrays using multichannel time-domain deconvolution, *Geophys. J. Int.*, 146, 57–67, 2001.

Noda, H., and N. Lapusta (2013). Stable creeping fault segments can become destructive as a result of dynamic weakening, *Nature* 493, 518-521.

Obara, K. (2002). Nonvolcanic deep tremor associated with subduction in southwest Japan, *Science* 296, 1679–1681.

Obara, K., H. Hirose, F. Yamamizu, and K. Kasahara (2004). Episodic slow slip events accompanied by non-volcanic tremors in southwest Japan subduction zone, *Geophys. Res. Lett*. 31, no. 23, L23602, doi: 10.1029/2004GL020848.

Oyman, O., R. Nabar, H. Bolcskei, and A. Paulraj, (2003) Characterizing the Statistical Properties of Mutual Information in MIMO Channels, *IEEE Trans. Signal Processing*, Vol. 51, no. 11, pp. 2784-2795, Nov. 2003

Pavlis, G. L., F. Vernon, D. Harvey, and D. Quinlan (2004). The generalized earthquake-location (GENLOC) package: An earthquake-location library, *Comput. Geosci*. 30, nos. 9–10, 1079–1091.

Peacock, S. M., N. I. Chiristensen, M. G. Bostock and P. Audet (2011). High pore pressures and porosity at 35 km depth in the Cascadia subduction zone, *Geology*. 39, 471-474.

Peng, Z., and K. Chao (2008). Non-volcanic tremor beneath the Central Range in Taiwan triggered by the 2001 Mw 7.8 Kunlun earthquake, *Geophys. J. Int*. 175, no. 2, 825–829.

Peng, Z., J. E. Vidale, K. C. Creager, J. L. Rubinstein, J. Gomberg, and P. Bodin (2008). Strong tremor near Parkfield, CA, excited by the 2002 Denali fault earthquake, *Geophys. Res. Lett*. 35, L23305, doi: 10.1029/2008GL036080.

Peng, Z., J. E. Vidale, A. G. Wech, R. M. Nadeau, and K. C. Creager (2009). Remote triggering of tremor along the San Andreas fault in central California, *J. Geophys. Res*. 114, B00A06, doi: 10.1029/2008JB006049.

Peng, Z., D. P. Hill, D. R. Shelly, and C. Aiken (2010), Remotely triggered microearthquakes and tremor in central California following the 2010 M_w 8.8 Chile earthquake, *Geophys. Res. Lett*., 37, L24312, doi:10.1029/2010GL045462.

Peng, Z., and J. Gomberg (2010). An integrated perspective of the continuum between earthquakes and slow-slip phenomena, *Nature Geoscience* 3, 599 - 607.

Peng, Z., H. Gonzalez-Huizar, K. Chao, C. Aiken, B. Moreno, and G. Armstrong (2013).

Tectonic Tremor beneath Cuba Triggered by the Mw 8.8 Maule and Mw 9.0 Tohoku-Oki Earthquakes. *Bulletin of the Seismological Society of America*, 103(1), 595-600.

Petersen, M. D., and S. G. Wesnousky (1994). Fault slip rates and earthquake histories for active faults in southern California, *Bull. Seismol. Soc. Am*. 84, no. 5, 1608–1649.

Plesch, A., J. H. Shaw, C. Benson, W. A. Bryant, S. Carena, M. Cooke, J. Dolan, G. Fuis, E. Gath, L. Grant, E. Hauksson, T. Jordan, M. Kamerling, M. Legg, S. Lindvall, H. Magistrale, C. Nicholson, N. Niemi, M. Oskin, S. Perry, G. Planansky, T. Rockwell, P. Shearer, C. Sorlien, M. P. Suss, J. Suppe, J. Treiman, and R. Yeats (2007). Community fault model (CFM) for southern California, *Bull. Seismol. Soc. Am*. 97, no. 6, 1793–1802.

Plesch, A., C. Tape, R. Graves, P. Small, G. Ely, and J. H. Shaw (2011). Updates for the CVM-H including new representations of the offshore Santa Maria and San Bernardino basin and a new Moho surface, *SCEC Annual Meeting*, Proceedings and abstracts, Vol. 21, Palm Springs, Florida.

Prejean, S. G., D. P. Hill, E. E. Brodsky, S. E. Hough, M. J. S. Johnston, S. D. Malone, D. H. Oppenheimer, A. M. Pitt, and K. B. Richards-Dinger (2004). Remotely triggered seismicity on the United States West Coast following the Mw 7.9 Denali fault earthquake, *Bull. Seismol. Soc. Am*. 94, no. 6B, S348–S359.

Rice, J. R. (1992). Fault stress states, pore pressure distributions, and the weakness of the San Andreas fault. *International Geophysics*, 51, 475-503.

Richards-Dinger, K. and Dieterich, J. H. (2012). RSQSim earthquake simulator. *Seismological Research Letters*, 83(6), 983-990.

Rockwell, T., C. Loughman, and P. Merifield (1990). Late quaternery rate of slip along the San Jacinto fault zone near Anza, southern California, *J. Geophys. Res*. 95, 8593–8606.

Rogers, G., and H. Dragert (2003). Episodic tremor and slip on the Cascadia subduction zone: The chatter of silent slip, *Science* 300, no. 5627, 1942–1943.

Rost, S., and C. Thomas (2002). Array seismology: Methods and applications, *Rev. Geophys*., 40 (3), 1008, doi:10.1029/2000RG0001002002.

Rubinstein, J. L., J. E. Vidale, J. Gomberg, P. Bodin, K. C. Creager, and S. D. Malone (2007). Non-volcanic tremor driven by large transient shear stresses, *Nature* 448, 579–582.

Rubinstein, J. L., M. L. Rocca, J. E. Vidale, K. C. Creager, and A. G. Wech (2008). Tidal modulation of nonvolcanic tremor, *Science* 319, 186.

Rubinstein, J. L., J. Gomberg, J. E. Vidale, A. G. Wech, H. Kao, K. C. Creager, and G. Rogers (2009). Seismic wave triggering of nonvolcanic tremor, episodic tremor and slip, and earthquakes on Vancouver Island, *J. Geophys. Res.* 114, no. B2, B00A01(22), doi: 10.1029/2008JB005875.

Rubinstein, J. L., D. R. Shelly, and W. L. Ellsworth (2010). Non-volcanic tremor: A window into the roots of fault zones, in *New Frontiers in Integrated Solid Earth Sciences*, S. Cloetingh and J. Negendank (Editors), Springer, Netherlands, 287–314.

Rubin, A. M.*, and* J.-P. Ampuero *(*2007*),* Aftershock asymmetry on a bimaterial interface*, J. Geophys. Res.,* 112*,* B05307, doi:10.1029/2006JB004337.

Ryberg, T., C. Haberland, G. S. Fuis, W. L. Ellsworth, and D. R. Shelly (2010). Locating non-volcanic tremor along the San Andreas Fault using a multiple array source imaging technique. *Geophysical Journal International*, 183(3), 1485-1500.

Sanders, C. O. (1990). Earthquake depths and the relation to strain accumulation and stress near strike-slip faults in southern California, *J. Geophys. Res*. 95, 4751–4762.

Sanders, C. O., and H. Kanamori (1984). A seismotectoonic analysis of the Anza seismic gap, San Jacinto fault zone, southern California, *J. Geophys. Res*. 89, 5873–5890.

Sanders, C. O., and H. Magistrale (1997). Segmentation of the northern San Jacinto fault zone, southern California, *J. Geophys. Res*. 102, no. B12, 27453–27467.

Schwartz, S. Y., and J. M. Rokosky (2007). Slow slip events and seismic tremor at circum-Pacific subduction zones, *Rev. Geophys*. 45, RG3004, doi: 10.1029/2006RG000208.

Sharp, R. V. (1967). San Jacinto fault zone in the Peninsular ranges of southern California, *Geol. Soc. Am. Bull*. 78, 705–730.

Shelly, D. R., G. C. Beroza, S. Ide, and S. Nakamula (2006). Low-frequency earthquakes in Shikku, Japan, and their relationship to episodic tremor and slip, *Nature* 442, 188–191.

Shelly, D. R., G. C. Beroza, and S. Ide (2007).Non-volcanic tremor and low-frequency earthquake swarms, *Nature* 446, 305–307.

Shelly, D. R., W. L. Ellsworth, T. Ryberg, C. Haberland, G. S. Fuis, J. Murphy, R. M. Nadeau, and R. Burgmann (2009). Precise location of San Andreas fault tremors near Cholame, California using seismometer clusters: Slip on the deep extension of the fault? *Geophys. Res. Lett*. 36, L01303.

Shelly, D. R., and J. L. Hardebeck (2010). Precise tremor source locations and amplitude variations along the lower-crustal central San Andreas fault, Geophys. *Res. Lett*. 37, no. 14, L14301.

Shelly, D. R., Z. Peng, D. P. Hill, and C. Aiken (2011). Triggered creep as a possible mechanism for delayed dynamic triggering of tremor and earthquakes, *Nature Geosci*. 4, no. 6, 384–388.

Sieh, K. (1986). Slip rate across the San Andreas fault and prehistoric earthquakes at Indio, *Eos Trans. AGU* 67, 1200.

Steidl, J., M. Gladwin, R. Gwyther, and F. Vernon (2000). Fault processes on the Anza section of the San Jacinto fault, *The Anza Broadband Seismic 24-bit Real-Time Telemetry Network Year 2000 Proposal*, UCSD, San Diego, California, 1–5.

Suess, M. P., and J. H. Shaw (2003). P wave seismic velocity structure derived from sonic logs and industry reflection data in the Los Angeles basin, California, *J. Geophys. Res*. 108, no. B3, 2170.

Sykes, L. R., and S. P. Nishenko (1984). Probabilities of occurrence of large plate rupturing earthquakes for the San Andreas, San Jacinto, and Imperial faults, California,1983–2003, *J. Geophys. Res*. 89, no. B7, 5905–5927.

Thatcher, W., J. A. Hileman, and T. C. Hanks (1975). Seismic slip distribution along the San Jacinto fault zone, southern California, and its implications, *Bull. Seismol. Soc. Am*. 86, no. 8, 1140–1146.

Thomas, M. A., R. M. Nadeau, and R. Burgmann (2009). Tremor-tide correlations and near-lithostatic pore pressure on the deep San Andreas fault, *Nature* 462, 1048–1051.

Thurber, C., H. Zhang, F. Waldhauser, J. Hardebeck, A. Michael, and D. Eberhart-Phillips (2006). Three-dimensional compressional wavespeed model, earthquake relocations, and focal mechanisms for the Parkfield, California, region. *Bulletin of the Seismological Society of America*, *96*(4B), S38-S49.

Trugman, D. T., E. G. Daub, R. A. Guyer, and P. A. Johnson (2013), Modeling dynamic triggering of tectonic tremor using a brittle-ductile friction model, *Geophys. Res. Lett*., 40, 5075–5079, doi:10.1002/grl.50981.

Tsuruoka, H., M. Ohtake and H. Sato (1995). Statistical test of the tidal triggering of earthquakes: contribution of the ocean tide loading effect, *Geophys. J. Int*., 122, 183-194.

Van Veen, B.D. and K.M. Buckley (1988). Beamforming: A versatile approach to spatial filtering. *IEEE ASSP Magazine* **5** (2): 4. doi:10.1109/53.665

Vanboskirk, E.J., M.H. Gottlieb, K.M. Hodgkinson, D. Mencin,W. Johnson, C. Pyatt, D.B. Henderson, O. Fox, W.W. Gallaher, M.E. Jackson, and the PBO BSM Group (2011). 2011 creep event observations in borehole strainmeter instrumentation along the San Andreas and San Jacinto faults (abstract T13A-2348), *AGU*, presented at 2011 Fall Meeting, San Francisco, California, 5–9 December, T13A-2348.

Wang, T. H., E. S. Cochran, D. Agnew, and D. D. Oglesby (2013). Infrequent triggering of tremor along the San Jacinto fault near Anza, California. *Bulletin of the Seismological Society of America*, 103(4), 2482-2497.

Wech, A. G., C. M. Boese, T. A. Stern, and J. Townend (2012). Tectonic tremor and deep slow slip on the Alpine Fault, *Geophys. Res. Lett.* 39*,* L10303, doi:10.1029/2012GL051751.

Wdowinski, S. (2009). Deep Creep as a cause for the excess seismicity along the San. Jacinto fault, *Nat. Geosci*. 2, 882–885.

Zhang, J., P. Gerstoft, P. M. Shearer, H. Yao, J. E. Vidale, H. Houston, and A. Ghosh (2011), Cascadia tremor spectra: Low corner frequencies and earthquake-like high-frequency falloff, *Geochem. Geophys. Geosyst*., 12, Q10007, doi:10.1029/2011GC003759.

Zigone, D., D. Rivet, M. Radiguet, M. Campillo, C. Voisin, N. Cotte, A. Walpersdorf, N. M. Shapiro, G. Cougoulat, P. Roux, V. Kostoglodov, A. Husker and J. S. Payero. (2012), Triggering of tremors and slow slip event in Guerrero, Mexico, by the 2010 Mw 8.8 Maule, Chile, earthquake, *J. Geophys. Res*., 117, B09304, doi:10.1029/2012JB009160.